# FIMP Dark Matter Genesis Produced via Non-Thermal Freeze-In Mechanism

*Master's thesis, May 25, 2019*

*Author:*

Henri Jutila

*Supervisor:*

Sami Nurmi

JYVÄSKYLÄN YLIOPISTO
UNIVERSITY OF JYVÄSKYLÄ

# Tiivistelmä

Jutila, Henri
FIMP pimeän aineen syntyminen ei-termisen freeze-in mekanismin kautta
Pro Gradu -tutkielma
Fysiikan laitos, Jyväskylän yliopisto, 2019, 92 sivua.

Kosmologiset havainnot kuten: galaksien rotaatiokäyrien käyttäytyminen, kosmisen taustasäteilyn yksityiskohdat ja gravitaatiolinssiefektiin perustuvat galaksijoukkojen massajakaumat tukevat pimeän aineen olemassaoloa. Havainnot antavat ymmärtää, että pimeää ainetta on viisinkertainen määrä baryoniseen aineeseen verrattuna, joka vuorovaikuttaa vain gravitaation kautta. Suurin osa pimeästä aineesta oletetaan olevan ei-baryonista ja koostuvan standardimallin ulkopuolisista hiukkasista. Kosmologisista havainnoista huolimatta pimeän aine pysyy näkymättömissä maailmankaikkeuden kulissien takana, sillä sitä ei ole pystytty kokeellisesti havaitsemaan. Pimeän aineen voidaan olettaa olevan termisessä tasapainossa varhaisessa maailmankaikkeudessa ja syntyneen samalla tavalla kuten kevyet reliikit termisen freeze-out mekanismin kautta. Näin syntynyttä pimeä aine -hiukkasta kutsutaan WIMPiksi (Weakly Interactive Massive Particle). Pimeä aine voi myös olla syntynyt vaihtoehtoisesti ei-termisesti freeze-in mekanismin kautta. Tällä tavalla syntynyttä pimeä aine -hiukkasta kutsutaan FIMPiksi (Feebly Interactive Massive Particle). Tässä tapauksessa pimeä aine ei missään vaiheessa saavuta termistä tasapainoa, koska kytkennät muihin hiukkasiin ovat hyvin heikkoja. Tässä tutkielmassa tarkastellaan molempia syntytapoja pitäen pääpainon freeze-in mekanismissa. $1 \to 2$ hajonnan ja $2 \to 2$ sironnan analyyttiset ja numeeriset ratkaisut määritetään pimeän aineen hiukkastiheydelle, joka on syntynyt freeze-in mekanismin kautta. Ratkaisut pimeän aineen energiatiheydelle vaadittavilla kytkennöillä esitetään vastaaville prosesseille.

Avainsanat: Pimeä aine, freeze-out, WIMP, freeze-in, FIMP

# Abstract

Jutila, Henri
FIMP Dark Matter Genesis Produced via Non-Thermal Freeze-In Mechanism
Master's thesis
Department of Physics, University of Jyväskylä, 2019, 92 pages.

Cosmological observations such as behavior of galaxy rotation curves, details of the cosmic microwave background and mass distribution of galaxy clusters based on gravitational lensing support the existence of dark matter. Observations indicate, that dark matter interacts only through gravity and outweighs baryonic matter five to one. Majority of dark matter is expected to be non-baryonic and composed of particles beyond Standard Model. Despite the various cosmological observations, dark matter remains hidden behind the scenes of the Universe, since there is no confirmed positive signal from experiments aiming to detect dark matter. In the early universe dark matter can be assumed to be in thermal equilibrium and produced similarly to light relics through thermal freeze-out mechanism involving Weakly Interacting Massive Particle (WIMP). Dark matter can also be produced alternatively non-thermally via freeze-in mechanism, involving Feebly Interacting Massive Particle (FIMP). In this case dark matter never attains thermal equilibrium, since the couplings to other particles are extremely weak. In this thesis both mechanisms are studied with main focus on freeze-in. Analytical and numerical solutions to the comoving number density of dark matter produced via freeze-in is determined for $1 \to 2$ decay and for $2 \to 2$ scattering. Solution to the dark matter energy density with required couplings are presented for the corresponding processes.

Keywords: Dark matter, freeze-out, WIMP, freeze-in, FIMP

# Notation

Natural units $c \equiv 1$, $\hbar \equiv 1$ and $k_B \equiv 1$ are used throughout the thesis. Metric signature is chosen as (-, +, +, +). Reduced Planck mass is $M_{\rm P} = \sqrt{1/(8\pi G)}$, where $G$ is the gravitational constant. Indices $(\mu, \nu \dots)$ correspond to all the space-time coordinates and summation over repeated indices is understood. Other notations are explained in the text.

**Parameters**

| | | |
|---|---|---|
| $G_F$ | Fermi Constant | $1.17 \times 10^{-5}$ GeV$^{-2}$ |
| $h$ | Reduced Hubble constant | $H_0/(100$ km/s/Mpc) |
| $M_{\rm P}$ | Reduced Planck Mass | $2.435 \times 10^{18}$ GeV |
| $T_0$ | Photon temperature today | $2.348 \times 10^{-4}$ eV |
| $\rho_c h^{-2}$ | Critical energy density | $8.1 \times 10^{-11}$ eV$^4$ |

**Abbrevations**

| | |
|---|---|
| CDM | Cold Dark Matter |
| CMB | Cosmi Microwave Background |
| DM | Dark Matter |
| FIMP | Feebly Interactive Massive Particle |
| HDM | Hot Dark Matter |
| SM | Standard Model |
| WIMP | Weakly Interactive Massive Particle |

# Contents

# 1 Introduction

Dark matter (DM) is something that we know exists in the Universe but has never been directly observed. This strange substance does not emit or absorb electromagnetic radiation. The origin and nature of DM is unknown, and it is one of the biggest mysteries in the field of cosmology and physics in general. DM is expected to consist of non-baryonic particles beyond Standard Model (SM) yet to be discovered, which only interacts through gravity. The effect of DM can be seen for example, in the motions of galaxies, which would not otherwise remain stable [1] and in many other independent observations [2], [3]. One possibility, what cannot be ignored, is that there is no missing mass and simply, our theory of gravity is wrong. But alternative theories, such as Modified Newtonian Dynamics (MOND), cannot provide satisfactory explanation to some of the cosmological observations without the need of dark matter [4]. Therefore, it is reasonable to believe, that the observed phenomena originate from unknown new particle beyond Standard Model. Recent results of Planck satellite indicate that our universe is composed of 68.5 % of dark energy, 26.4 % of dark matter and only 5.1 % of baryonic matter [5].

In 1933 Fritz Zwicky observed the velocities of galaxies in Coma Cluster [6]. He deduced that there had to be significantly more mass in the cluster compared to the visible mass for the system to be stable. Although Zwicky discussed about dark matter, he believed that it originated from cool and cold stars, macroscopic and microscopic solid bodies and gases [7].

In the 1960s and 1970s Vera Rubin provided strong evidence for the existence of dark matter by studying the galaxy rotation curves. She concluded, that there must be significant amount of non-luminous matter well beyond the optical galaxy, otherwise galaxies would fly apart [1]. The observation could be explained by dark matter halo surrounding the galaxy. Soon, the theory of dark matter was widely recognized, and characteristics of this excess mass became a major problem in physics.

The Cosmic Microwave Background observations suggest that SM particles have been in thermal equilibrium in the early universe [5]. The hypothetical dark matter particles can be assumed to be part of the same thermal bath. In this scenario DM is thermal relic, referred as Weakly Interacting Massive Particle (WIMP), and produced similarly to SM particles through thermal freeze-out mechanism [8]. However, DM might never have been in thermal equilibrium and the observed DM abundance might have been generated alternatively through non-thermal freeze-in

mechanism [9] involving Feebly Interacting Massive Particle (FIMP).

This thesis provides a general overview to dark matter and to two production mechanisms: freeze-out and freeze-in. In section 2, strong observational evidence supporting the existence of non-baryonic DM is presented, following the introduction of thermal freeze-out mechanism in section 3,. An alternative production mechanism, thermal freeze-in is presented, and compared to the more conventional freeze-out mechanism in section 4. Analytical and numerical solutions to the comoving number density of DM generated through freeze-out and freeze-in mechanism are also presented together with the couplings required to generate the observed dark matter density $\Omega_h^2 = 0.12$. As an example, freeze-in mechanism is applied to a specific sterile neutrino dark matter model after accomplishing the basics of the freeze-in mechanism. The status and prospects of experiments aiming to detect DM is discussed in section 5.

## 1.1 FRW cosmology

The cosmological principle states that the Universe is spatially homogeneous and isotropic on large scales. The Universe is the same everywhere and there is no preferred direction. The metric describing the homogeneous and isotropic universe is the Friedmann-Robertson-Walker (FRW) metric, which can be written in the form of line element $ds^2 = g_{\mu\nu}dx^\mu dx^\nu$, which reads [10], [11]

$$ds^2 = -dt^2 + a^2(t)\Big(\frac{dr^2}{1-Kr^2} + r^2 d\theta^2 + r^2 \sin^2\theta d\phi^2\Big). \tag{1.1}$$

The factor $a(t)$ is the dimensionless scale factor, which describes how the Universe expands or contracts. $K$ describes the curvature of the Universe. $K < 0$ corresponds to open Universe and $K > 0$ corresponds to a closed Universe. The Universe is spatially flat if $K = 0$. The parameters $t, r, \theta$ and $\phi$ are referred as comoving coordinates. Comoving observer will perceive the Universe to be isotropic. The proper distance between two galaxies changes due to the expansion of the Universe, while their distance in comoving frame remains the same all times.

The standard model of cosmology is based on General Relativity (GR), which states that gravity is a geometric property of space-time and can be derived from the Einstein-Hilbert Lagrangian

$$S = \frac{M_{\rm P}^2}{2}\int d^4x\sqrt{-g}R + \int d^4x\sqrt{-g}\mathcal{L}_m, \tag{1.2}$$

where $R$ is the Ricci scalar and $\mathcal{L}_m$ lagrangian for matter fields. $M_{\rm P}$ is the reduced Planck mass and $g$ is the determinant of the metric defined as $g \equiv \det(g_{\mu\nu})$. Einstein's field equations can be obtained by variating the metric

$$R_{\mu\nu} - \frac{1}{2}Rg_{\mu\nu} = 8\pi G T_{\mu\nu}, \tag{1.3}$$

where $R_{\mu\nu}$ is the Ricci tensor related to curvature of space-time and the stress energy momentum tensor $T_{\mu\nu}$ describes the source of gravitational fields in space-time.

The evolution of homogeneous and isotropic universe is often described as universe filled with a ideal fluid. For continuous frictionless matter, the stress energy momentum tensor has the form

$$T^{\mu\nu} = \rho u^{\mu} u^{\nu} + p(g^{\mu\nu} + u^{\mu} u^{\nu}), \tag{1.4}$$

where $\rho$ is the energy density and $p$ is the pressure of the ideal fluid. Four-velocity of the ideal fluid is denoted by $u^{\mu}$ in comoving coordinates. Stress energy momentum conservation $\nabla_{\mu} T^{\mu\nu} = 0$ gives the continuity equation in comoving coordinates

$$\dot{\rho} + 3H(\rho + p) = 0. \tag{1.5}$$

Volume expansion of the fluid is described by the Hubble parameter $H$. The equation of state describes the physical properties of the ideal fluid and is defined as

$$p(t) = w(t)\rho(t). \tag{1.6}$$

If the parameter $w$ is constant the continuity equation (1.5) can be solved for energy density

$$\rho = \rho_0 \left( \frac{a_0}{a} \right)^{3(1+w)}. \tag{1.7}$$

The equation of state parameter $w = 1/3$ corresponds to radiation or relativistic matter and $w = 0$ corresponds to dust or non-relativistic matter. At late times vacuum energy or the cosmological constant $\Lambda$ corresponding to $w = -1$, can be included in equation (1.3) acting as repulsive force [11].

Using the FRW metric and the idea that homogeneous and isotropic universe can be described as ideal fluid at rest, the stress energy momentum tensor (1.4) has the form $T^{\mu}{}_{\nu} = \mathrm{diag}(-\rho, p, p, p)$. The Einstein's field equations are collection of ten coupled partial differential equations. In FRW universe Einstein's equations are reduced to two ordinary differential equations. First one is called the Friedmann equation

$$H^2 = \frac{\rho}{3M_{\mathrm{P}}^2} - \frac{K}{a^2}, \tag{1.8}$$

which is derived from the 0 – 0 component of equation (1.3). $H$ in the above equation is the Hubble parameter defined as

$$H(t) \equiv \frac{\dot{a}(t)}{a(t)}, \tag{1.9}$$

where $\dot{a}$ is the time derivative of the cosmic scale factor. The second differential equation derived from (1.3) is

$$2\frac{\ddot{a}}{a} + H^2 = -\frac{p}{M_{\rm P}^2} - \frac{K}{a^2}, \tag{1.10}$$

which is obtained from the $i$ – $i$ components. The second Friedmann equation or often called the acceleration equation can be obtained by rearranging equations (1.8) and (1.10)

$$\frac{\ddot{a}}{a} = -\frac{\rho + 3p}{6M_{\rm P}^2}. \tag{1.11}$$

FRW universe is thus described by three variables, the cosmic scale factor $a(t)$, the energy density $\rho(t)$ and the equation of state parameter $w(t)$, and two independent equations, the continuity equation (1.5) and the Friedmann equation (1.8).

From the Friedmann equation we can obtain the critical density defined as

$$\rho_c \equiv 3H_0^2 M_{\rm P}^2, \tag{1.12}$$

where $H_0 = 67.4$ km/s/Mpc [5] is the present value of Hubble constant. This is the density of spatially flat FRW universe ($K = 0$) expanding at a rate of $H(t)$. The density parameter is given by

$$\Omega(t) = \frac{\rho(t)}{\rho_c(t)}, \tag{1.13}$$

where the $\rho(t)$ is the actual density of the Universe. The density parameter is the sum of different components including dark matter, baryonic matter and dark energy ($\Omega = \Omega_{\rm c} + \Omega_{\rm b} + \Omega_\Lambda$), which are the three major components of the standard model of Big Bang cosmology or the $\Lambda$CDM model.

## 1.2 Thermodynamics

Particles in the early universe can be assumed to be in thermal equilibrium. By applying thermodynamics and statistical physics gives clues about the evolution of the early universe. The energy of a particle in thermal equilibrium is

$$E = \sqrt{|\vec{\mathbf{p}}|^2 + m^2}, \tag{1.14}$$

where $|\vec{\mathbf{p}}|$ is three-momentum and $m$ is the mass of the particle. The distribution function in thermodynamic equilibrium describes the states that particle can occupy defined by [10]

$$f(\vec{p}) = \frac{1}{e^{(E-\mu)/T} \pm 1}, \tag{1.15}$$

which is used to find the probability that a state is occupied. The $(+1)$ refers to fermions and the $(-1)$ to bosons. The chemical potential of the particle is denoted by $\mu$.

In phase space the particle number density, energy density and pressure can be written as integrals over momentum space [10]

$$n_i = \frac{g_i}{(2\pi)^3}\int f_i(\vec{p})d^3p \tag{1.16}$$

$$\rho_i = \frac{g_i}{(2\pi)^3}\int E_i(\vec{p})f_i(\vec{p})d^3p \tag{1.17}$$

$$p_i = \frac{g_i}{(2\pi)^3}\int \frac{|\vec{\mathbf{p}}|^2}{3E_i(\vec{p})}f_i(\vec{p})d^3p, \tag{1.18}$$

where the prefactor $g_i/(2\pi)^3$ is the density of states and $g_i$ is the number of internal degrees of freedom. Different particle species is denoted by $i$. In the relativistic limit $T \gg m$, we can approximate $E \approx |\vec{\mathbf{p}}|$. Therefore, the above quantities yield

$$\begin{aligned} n_{\mathrm{b}} &= \frac{1}{\pi^2}\zeta(3)gT^3 & n_{\mathrm{f}} &= \frac{3}{4\pi^2}\zeta(3)gT^3 \\ \rho_{\mathrm{b}} &= \frac{\pi^2}{30}gT^4 & \rho_{\mathrm{f}} &= \frac{7}{8}\frac{\pi^2}{30}gT^4 \\ p_{\mathrm{b}} &= \frac{1}{3}\frac{\pi^2}{30}gT^4 & p_{\mathrm{f}} &= \frac{1}{3}\frac{7}{8}\frac{\pi^2}{30}gT^4 \end{aligned} \tag{1.19}$$

For bosons and fermions respectively. For the non-relativistic limit $T \ll m$ we can approximate $E \approx m + |\vec{\mathbf{p}}|^2/(2m)$ and obtain the results

$$n = g\left(\frac{mT}{2\pi}\right)^{3/2} e^{-\frac{m-\mu}{T}} \tag{1.20}$$

$$\rho = n\left(m + \frac{3T}{2}\right) \tag{1.21}$$

$$p = nT. \tag{1.22}$$

In the non-relativistic limit particle number density, energy density and pressure get suppressed exponentially as the temperature falls below the mass of the particle.

Friedmann equation states that the expansion of the Universe is governed by the total energy density. This includes all relativistic particle species and excludes non-relativistic species. This holds true in the early universe, but not at late times. The total energy density can be written as [10]

$$\rho(T) = \frac{\pi^2}{30}g_{*\rho}(T)T^4, \tag{1.23}$$

where $g_{*\rho}$ is the effective number of energy degrees of freedom defined as

$$g_{*\rho}(T) = \sum_{\text{bos}} g_i \left(\frac{T_i}{T}\right)^4 + \frac{7}{8} \sum_{\text{fer}} g_i \left(\frac{T_i}{T}\right)^4, \tag{1.24}$$

where some of the species may have different temperature $T_i$ than the species in thermal equilibrium. The Hubble parameter can be obtained in terms of $g_{*\rho}$ from the Friedmann equation (1.8) to yield

$$H = \left(\frac{g_{*\rho}\pi^2}{90 M_{\text{P}}^2}\right)^{1/2} T^2. \tag{1.25}$$

Consider the fundamental equation of thermodynamics

$$dE = TdS - pdV + \sum_i \mu_i N_i. \tag{1.26}$$

This gives the entropy density

$$s = \frac{\rho + p - \sum_i \mu_i n_i}{T}. \tag{1.27}$$

While $|\mu_i| \ll T$ and using the expressions for density $\rho$ and pressure $p$ in equation (1.19), and summing all the possible relativistic species we get [10]

$$s(T) = \frac{2\pi^2}{45} g_{*s}(T) T^3, \tag{1.28}$$

where $g_{*s}$ is the effective number of entropy degrees of freedom defined as

$$g_{*s}(T) = \sum_{\text{bos}} g_i \left(\frac{T_i}{T}\right)^3 + \frac{7}{8} \sum_{\text{fer}} g_i \left(\frac{T_i}{T}\right)^3. \tag{1.29}$$

# 2 Evidences of dark matter

The effects of dark matter can be seen in various ways. In this section strong observational evidence for the existence of non-baryonic dark matter is presented. Rotation curves and gravitational lensing are discussed, followed by an overview of how the structure of the Universe would be significantly different without dark matter.

## 2.1 Galaxy rotation curves

One of the earliest evidences of dark matter came from Fritz Zwicky, who studied motions of galaxies near the edge of Coma Clusters in the 1930s [6] [7]. He used the virial theorem to estimate the mass of Coma Cluster and compared it to the mass obtained based on the brightness and number of galaxies in the cluster.

Virial theorem is used to estimate the properties of complicated many particle systems that are otherwise impossible to solve. The theorem states that a bound system in equilibrium obeys

$$\langle K \rangle = -\frac{1}{2}\langle U \rangle, \tag{2.1}$$

where $\langle K \rangle$ and $\langle U \rangle$ are mean kinetic and potential energy respectively. By estimating the number of individual galaxies in the cluster and their masses we get the mean velocity for the galaxies in the cluster

$$\langle v \rangle = \sqrt{\frac{3GM}{5R}}, \tag{2.2}$$

where $R$ is the radius and $M$ is the mass of the cluster.

Zwicky estimated that the density had to be at least 400 times greater than what was observed visually alone [6]. Zwicky's work was based on the Hubble constant and at that time the value of Hubble constant was measured to be $H_0 = 558$ km/s/Mpc. By adopting the modern value $H_0 = 67.4$ km/s/Mpc still gives a high mass-to-light ratio pointing towards missing mass.

Further evidence of dark matter was provided by Vera Rubin, who studied the rotation of the Andromeda galaxy (M31) [12]. She continued researching rotation curves of other galaxies in the 1970s. Her results confirmed, that stars orbit the galaxy roughly at the same velocity regardless of the distance from galaxy center. This implied, that galaxies with different luminosities must have significant mass beyond the luminous region [1].

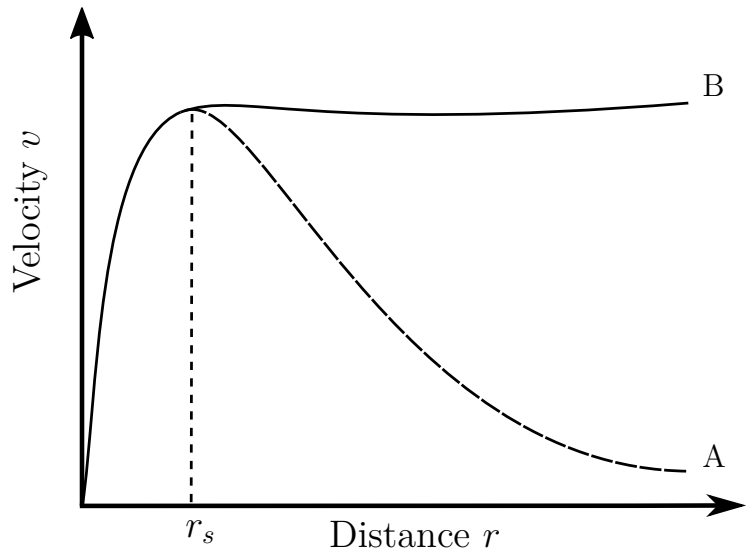


Figure 1: Illustration of rotation curve of a typical spiral galaxy, where (A) is the predicted Keplerian rotation, if most of the mass is at the center of a galaxy, and (B) is the observed rotation curve. $r_s$ represents the limit of visible galaxy, where majority of the baryonic matter is.

Newtonian gravity states that the velocity $v$ of a body on a circular orbit around mass $M(r)$ in an axially symmetric mass distribution is

$$v^2 = \frac{GM(r)}{r}, \tag{2.3}$$

where $M(r)$ is the mass inside radius $r$ and $G$ is the gravitational constant. Equation (2.3) is called the rotation curve. For example, rotation curve of the Earth, orbiting around the Sun obeys $v(r) \propto r^{-1/2}$, where $M = M_\odot$ is the mass of the Sun. The situation for stars orbiting the center of a galaxy is different, because the mass of a galaxy increases respect to distance, however we should see behavior $r^{-1/2}$ in the outer regions of galaxies where stars are not visible.

Assume that the energy density of a spiral galaxy decreases as a power-law

$$\rho = r^{-n} \tag{2.4}$$

where $n$ is an arbitrary constant. The mass inside radius $r$ is then

$$M(r) = \int \rho dV \propto r^{3-n} \qquad \text{for} \qquad n < 3, \tag{2.5}$$

therefore, the rotation curve of a galaxy is

$$v(r) \propto r^{1-n/2}. \tag{2.6}$$

Vera Rubin observed from visible stars, that the rotation curves increased rapidly with small $r$ up to $\sim$ 5 kpc [1] from the center of the galaxy and typically flatten out thereafter so that $v(r) \approx$ constant. Roberts and Whitehurst observed the same flattened rotation curve for M31 from 21-cm hydrogen line outside the visible region, where the mass of hydrogen accounts for $\sim$ 1 % of the total mass [13]. Constant rotation velocity and equation (2.6) would indicate a density profile proportional to

$$\rho \propto r^{-2} \tag{2.7}$$

at large distances.

The density profile $\rho \propto r^{-2}$ is actually the density profile of pressureless non-relativistic ideal gas. Consider an ideal gas sphere with mass $M(r)$ and a volume element with mass $m = \rho A dr$ inside the sphere. A is constant and $\rho$ is the density of the volume element. The system is balanced if the gravitational force of the element is equal to the gradient of the pressure inside the sphere. This is called the hydrostatic equilibrium equation

$$\frac{dp}{dr} = -\frac{GM(r)\rho(r)}{r^2}, \tag{2.8}$$

where $p$ is pressure and $r$ is distance to the volume element from the center of the sphere. Using (1.22) the equation (2.8) can be written as

$$4\pi \int_0^R r^2 \rho(r) dr = -\frac{T}{mG}\frac{r^2}{\rho}\frac{d\rho}{dr}, \tag{2.9}$$

where the LHS is the mass of the sphere $M(r)$. Taking the derivative with respect to $r$ on both sides we get

$$4\pi^2 \rho(r) = -\frac{T}{mG}\frac{d}{dr}\Big[r^2 \frac{d}{dr}\Big(\ln \rho\Big)\Big]. \tag{2.10}$$

Using ansatz: $\rho = Cr^{\lambda}$ we get

$$r^{2+\lambda} = -\frac{T\lambda}{4\pi C m G}. \tag{2.11}$$

The above equation is satisfied when $\lambda = -2$ and $C = T/(2\pi mG)$. Therefore, the solution to equation (2.8) is

$$\rho = \frac{T}{2\pi mG} r^{-2}, \tag{2.12}$$

which is the wanted form $\rho \propto r^{-2}$.

Figure 1 shows the predicted Keplerian rotation curve (A), assuming that majority of mass is located at the center of the galaxy, and the observed rotation

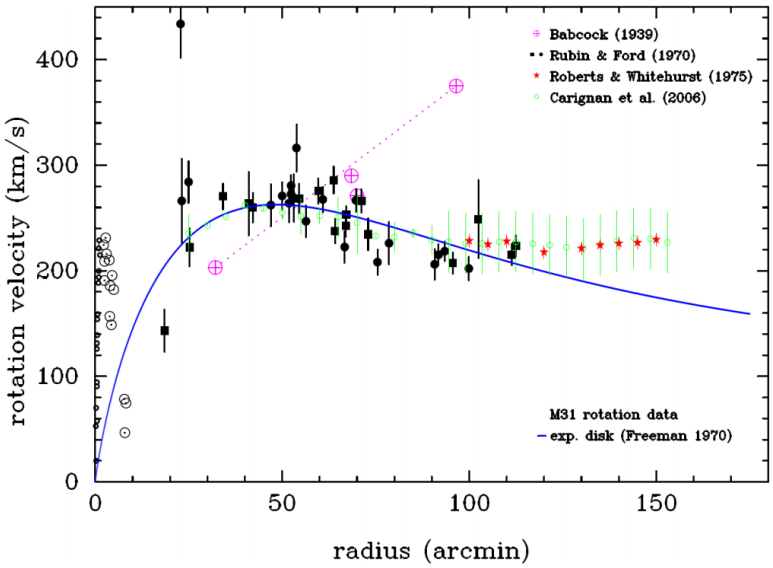


Figure 2: Experimental results for M31 rotation curve from multiple experiments showing flat rotation curve in the outer parts of the galaxy. The purple points are emission line data from Babcock (1939) [14], the black squares and rectangles are from Rubin & Ford (1970) [12], the red points are from Roberts & Whitehurst (1975) [13] and the green points are from Carignan et al. (2006) [15]. The solid line is rotation curve of an exponential disc based on Freeman (1970) [16]. Figure is from [17].

curve (B). Near the center of the galaxy the rotation curve acts like of rigid body, $v(r) \propto r$, but then flattens out, $v(r) \propto$ const. This implies, that there has to be another mass component, which cannot be observed with conventional methods, since the total mass from the luminous matter is not enough to account for the observed rotation velocity at large distances. In the inner region of the galaxy the unknown mass should be sub-dominant and in the outer region it should be dominant. This mass component is described as a dark matter halo surrounding the galaxy that expands well beyond the visible parts of the galaxy. Figure 2 shows multiple experimental results for rotation curve of M31, including Rubin and Ford [12] based on visible stars and Roberts and Whitehurst based on the 21-cm signal [13].

Fit to N-body simulations indicate, that instead of density profile $\rho \propto r^{-2}$, which only describes outer parts of a galaxy, the distribution of dark matter in galaxies is better described with Navarro-Frenk-White profile [18]

$$\rho = \frac{\rho_0}{\frac{r}{r_s}(1+\frac{r}{r_s})^2}. \tag{2.13}$$

It describes both inner and outer regions of a galaxy. $r_s$ and $\rho_0$ are parameters which vary from halo to halo. This does not apply near the center of the galaxy, where the density is dominated by baryonic matter. It is still unclear what are the effects of regions with high baryon density to dark matter density profile, but observations indicate, that the gravitational potential from DM is negligible compared to baryons at the center of a galaxy [19].

## 2.2 Gravitational lensing

In 1915 Albert Einstein published his new theory of gravity, general relativity, that links together matter and curvature of space-time. In short, matter tells space-time how to curve and space-time tells matter how to move. GR states that light is also affected by the curvature of space-time, which has been experimentally verified just as GR predicted [20].

Gravity can be defined as the effect, which curvature of space-time has on objects with mass. In other words, falling objects do not feel gravitational attraction, instead they follow geodesics, i.e., straight path in curved space-time, if no other forces such as air resistance act on the objects. Light propagating through distorted fabric of space-time also moves along geodesic, which is perceived as "bending of light". In reality, the space-time itself is bent.

When looking at distant galaxies in the sky, a massive object between observer and the light source distort and shift the image of the galaxy just like when using a magnifying glass. This effect is called gravitational lensing and the distribution of matter between observer and the distant light source is called gravitational lens [21]. The gravitational lensing affects all kinds of electromagnetic radiation equally and can be accurately calculated, when the mass distribution of the lens is known, which on the other hand gives information on the distribution of dark matter in the lens.

Strong lensing effect causes distortions, which are easily visible. It can cause formation of multiple images as illustrated in Figure 3, or even a ring around the lens called Einstein ring. First gravitational lens system was discovered in 1979 [22]. Twin Quasar Q0957+561A was later determined to consist of two images of the same object [23].

In GR Schwarzschild metric is one solution to Einstein's field equations assuming spherical symmetry [11]

$$ds^2 = -(1 - \frac{r_s}{r})dt^2 + (1 - 2\frac{r_s}{r})^{-1}dr^2 + r^2 d\theta^2 + r^2 \sin^2\theta d\varphi^2, \tag{2.14}$$

where $r_s = 2GM$ is the Schwarzschild radius of a body with mass $M$. Schwarzschild metric is a good approximation for example describing the movement of

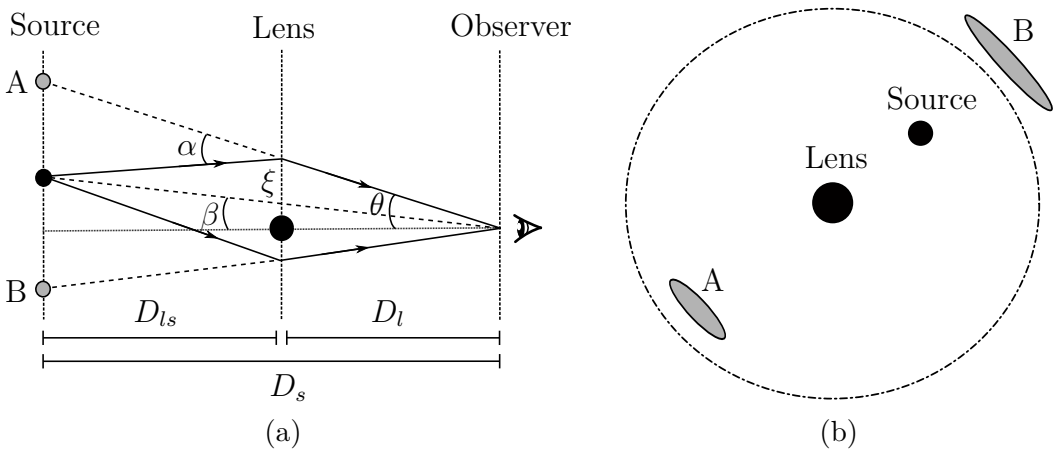


Figure 3: Illustration of the geometry of the gravitational lenses, where A and B are the virtual images of the source. On the left side $\alpha$ represents the deflection angle and $\xi$ is the impact parameter.

massive bodies in solar system. The deflection angle for a point mass using Schwarzschild metric is [21]

$$\alpha = \frac{4GM}{\xi}, \tag{2.15}$$

where $\xi$ is the impact parameter representing the distance to the nearest light beam from the center of mass. Based on Figure 3a and using small angle approximation we can write the lens equation

$$\theta D_s = \alpha D_{ls} + \beta D_s, \tag{2.16}$$

where $D_s, D_l$ and $D_{ls}$ are the distances from observer to source, from observer to lens and from lens to source respectively. $\theta$ and $\beta$ are the corresponding angles. Substituting equation (2.15) into the lens equation and writing the impact parameters as $\xi = \theta D_l$ we get

$$\theta - \beta = \frac{4GM}{\theta D_l}\frac{D_{ls}}{D_s}. \tag{2.17}$$

If the source is right behind the lens, i.e., $\beta = 0$ the Einstein radius in radians for point mass is

$$\theta = \sqrt{\frac{4GMD_{ls}}{D_l D_s}}, \tag{2.18}$$

which is the characteristic angle for gravitational lensing in general. The typical distance between images are of the order of the Einstein radius $\theta$. Note that in Figure 3 we do not observe the source, instead we only see the virtual images. In reality, more complicated models are applied to gravitational lens systems [24], [25].

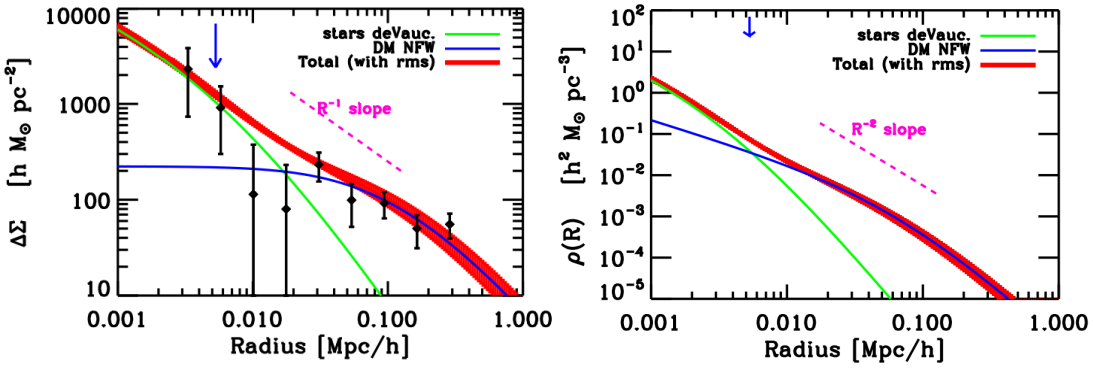


(a) (b)

Figure 4: Shear profile (a) and density profile (b) for the best DM + de Vaucouleurs profile of 22 strong lens galaxies with weak gravitational lensing data points. The expected stellar and dark matter components are shown as green and blue lines respectively. The mean effective radius is marked by blue arrow. The thickness of the red curve corresponds to $1\sigma$ uncertainty in the total shear profile. Figure is from [26].

Distortions caused by weak gravitational lensing are much harder to detect. Weak gravitational lensing surveys aim to find coherent distortions between large number of galaxies in statistical way [27], [28]. Weak gravitational lensing analyses are applied to large number of scales ranging from galaxies to galaxy clusters or even larger scales [29].

The gravitational lensing acts as coordinate transformation, that reshapes the images of background objects. It can be divided into two components, convergence and shear. First component increases size and the other stretches the object. Consider a hypothetical circular light source deformed by weak gravitational lensing. The ellipticity of such image is defined by the reduced shear [29]

$$\varrho = \frac{\gamma}{1-\kappa}, \tag{2.19}$$

where $\gamma$ is the shear and $\kappa$ is the convergence. In case of weak gravitational lensing $\kappa \ll 1$ and therefore $\varrho \approx \gamma$. In reality the observed galaxies are not circular, instead they are intrinsically elliptical. The total ellipticity of a galaxy is the sum of the reduced shear and the intrinsic ellipticity

$$\epsilon \approx \varrho + \varepsilon_s, \tag{2.20}$$

which holds true in the lowest-order approximation [29]. The intrinsic ellipticity

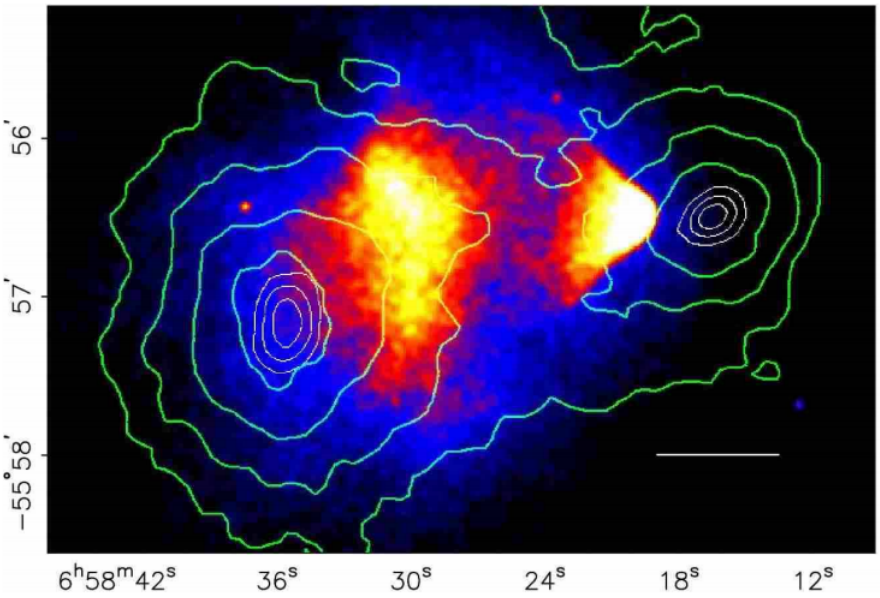


Figure 5: X-ray image of Bullet Cluster (1E0657-558) of two colliding galaxy cluster by Chandra X-ray Observatory with exposure time around 140 hours [30]. The blue-red-yellow-white areas are the hot baryonic matter and the green contours represents the mass concentration in the two clusters based on weak gravitational lensing. The white bar represents 200 kpc. Figure taken from [2]

should be almost entirely random [31] therefore, in weak gravitational lensing analysis when averaging over large number of samples it is essential to verify, that the intrinsic ellipticities approach zero $\langle \epsilon_s \rangle \approx 0$. Therefore, any systematic orientation between multiple galaxies point towards weak gravitational lensing.

Galaxy-galaxy lensing [32] is used to determine the mass-to-light ratios of galaxies, their sizes and constraints on their surface density profiles [29]. Shear profile and close to isothermal ($\rho \propto r^{-2}$) density profile was obtained from analysis of weak gravitational lensing of 22 strong lens galaxies [26] shown in Figure 4. The transition between the component profiles occurs close to the mean effective radius at which half of the total light of the system is emitted.

Weak gravitational lensing by galaxy clusters help to determine the distribution of dark and luminous matter in the clusters and to constrain the amount of structure in them [29]. Weak gravitational lensing by the Bullet Cluster (1E0657-558) was observed [2], which consists of two colliding clusters of galaxies. Figure 5 is the X-ray photo by Chandra X-ray Observatory [30] of the collision, where smaller "bullet" cluster has passed through the larger cluster. It is clear, that most of the mass is not where the normal baryonic matter is. Therefore, this is a clear

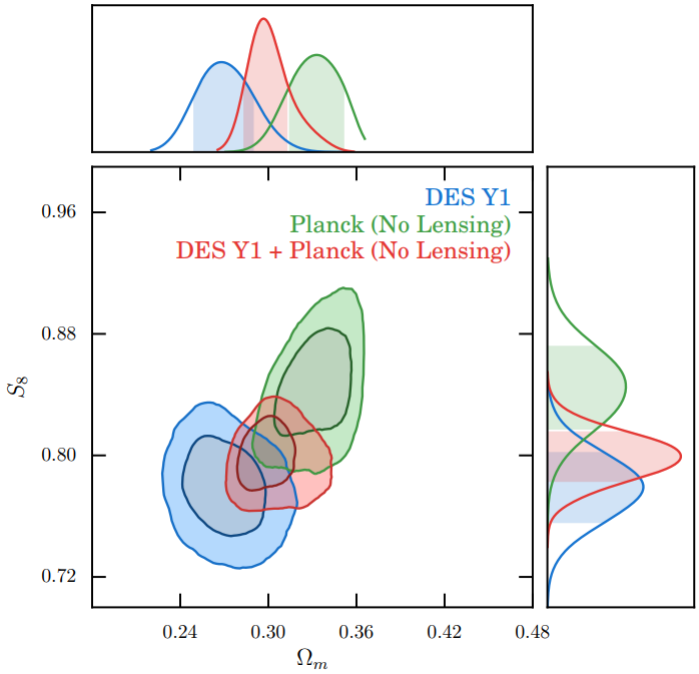


Figure 6: DES Y1 (blue) and Planck (green) constraints on the parameter space of $\Omega_m$ and $S_8$. The combination of the two is shown as red area. Figure is from [33].

evidence of dark matter. The hot baryonic matter in each cluster was slowed down during the collision, but dark matter was not affected by the impact and passed through the bigger cluster.

Weak gravitational lensing by large scale structures is used to probe the matter density parameter $\Omega_m$ and amplitude $\sigma_8$ of matter power spectrum [34], [35]. The Dark Energy Survey (DES) [36] aims to reveal the nature of dark matter and dark energy causing the expansion of our Universe to accelerate [37]. DES is expected to catalogue hundreds of millions of galaxies with information about the shape of the galaxy, which is connected to the weak gravitational lensing. The DES year 1 combined analysis of galaxy clustering and weak gravitational lensing results, shown in Figure 6 show, that the constraints between DES and Planck on $\Omega_m$ and $S_8 = \sigma_8(\Omega_m/0.3)^{0.5}$ are consistent when quantified via Bayes factor [33].

## 2.3 Cosmic microwave background

By pointing a sufficiently sensitive radio telescope at a dark spot in the sky in arbitrary direction shows faint background noise, that is not associated with any astronomical object. This microwave band noise would seem to originate from

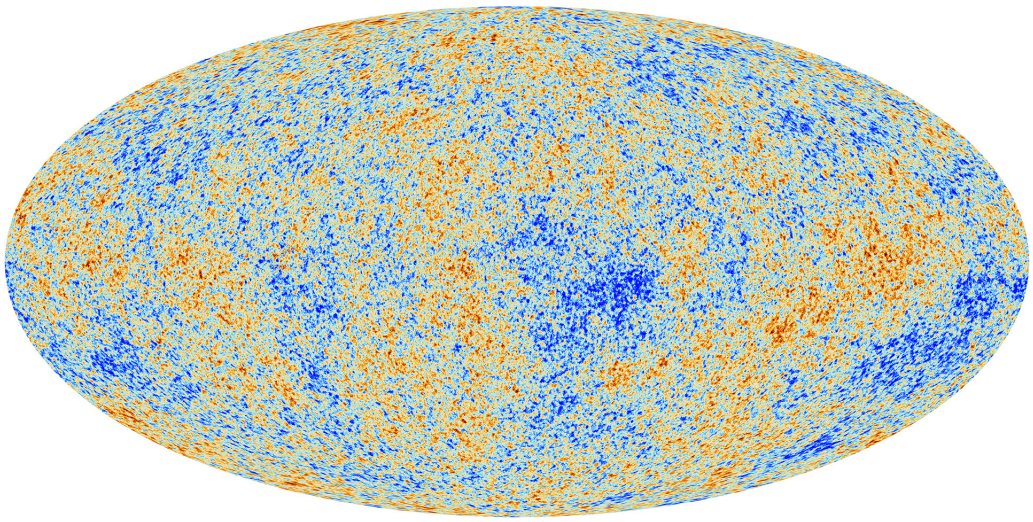

Figure 7: Mollweide projection of the CMB by Planck. Different colors represent temperature fluctuation in the early universe. Red spots correspond to higher temperatures than average and blue spots to lower temperatures than average. Image is from [39].

everywhere, regardless where the telescope is pointed at. The electromagnetic radiation left over is called the Cosmic Microwave Background (CMB), discovered in 1965 [38]. CMB originates from the early stage of the Universe and is profound evidence of the Big Bang theory.

In the early universe the temperature remained too high for electrons to bound with nuclei and Compton scatterings

$$e^- + \gamma \leftrightarrow e^- + \gamma, \tag{2.21}$$

dominated the thermal equilibrium. Photons could not travel very far before they collided with electrons and the Universe remained opaque. As the Universe expanded and cooled, neutral atoms were formed. This era is referred as recombination, which took place around $z_{\text{rec}} \simeq 1300$ [10]. The absence of electrons and insufficient energy of the photons enabled them to travel long distances, which is referred as the photon decoupling, that occurred at redshift [10]

$$z_{\text{dec}} \simeq 1100 \simeq \frac{a_0}{a_{\text{dec}}} \simeq \frac{T_{\text{dec}}}{T_0}. \tag{2.22}$$

After decoupling, photons started to propagate freely through space and the Universe became transparent. As the Universe expands it causes the wave length of the photons to increase over time. The decoupled photons can be observed today as CMB with mean temperature $T_0 = 2.725$ K [40].

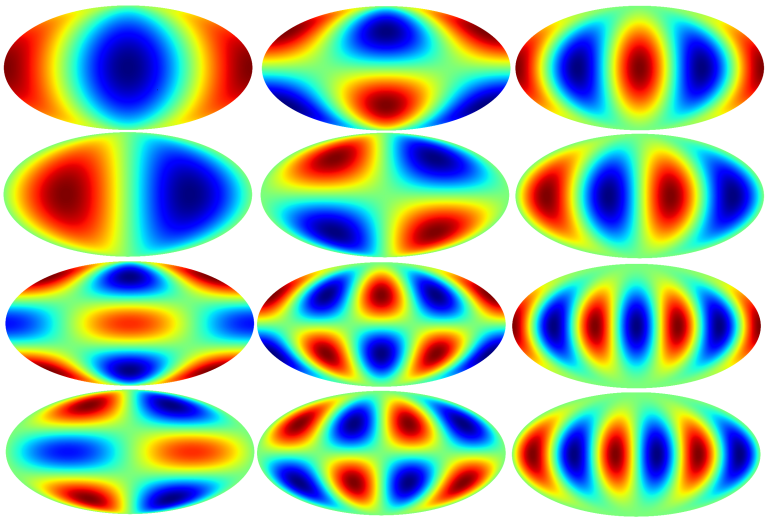

Figure 8: Real and imaginary part of spherical harmonics $Y_{11}$, $Y_{21}$, $Y_{22}$, $Y_{31}$, $Y_{32}$ and $Y_{33}$.

Detailed images of the CMB have been able to construct by observing the microwave band electromagnetic radiation, first by COBE satellite [41] and later improved by WMPA [42]. The latest image of the CMB all-sky map is by Planck [5] shown in Figure 7, contains very small deviations $\delta T/T \sim 10^{-5}$ [10] in the temperature.

A sky map of the CMB anisotropy can be presented as an angular power spectrum, which is the amplitude of the fluctuations as a function of scale. Since the CMB is a projection of the fluctuations on a celestial sphere at the time of last scattering, it is useful to expand the anisotropies in spherical harmonics $Y_{lm}(\theta, \phi)$ [43]

$$\frac{\delta T}{T}(\theta, \phi) = \sum_{l=0}^{\infty} \sum_{m=-l}^{m=l} a_{lm} Y_{lm}(\theta, \phi). \tag{2.23}$$

The spherical harmonics are set of orthogonal functions on a sphere. In this expansion low values of $l$ corresponds to large scale and high values of $l$ corresponds to small scale. The spherical harmonics are illustrated in Figure 8 with multipoles $l = 1, 2, 3$. One useful property of spherical harmonics is, that we can sum all $m$ corresponding to the same $l$. This is called the closure relation

$$\sum_{m} |Y_{lm}(\theta, \phi)|^2 = \frac{2l+1}{4\pi}. \tag{2.24}$$

The multipole coefficients $a_{lm}$ in equation (2.23) can be calculated from

$$a_{lm} = \int Y^*(\theta, \phi) \frac{\delta T}{T}(\theta, \phi) d\Omega. \tag{2.25}$$

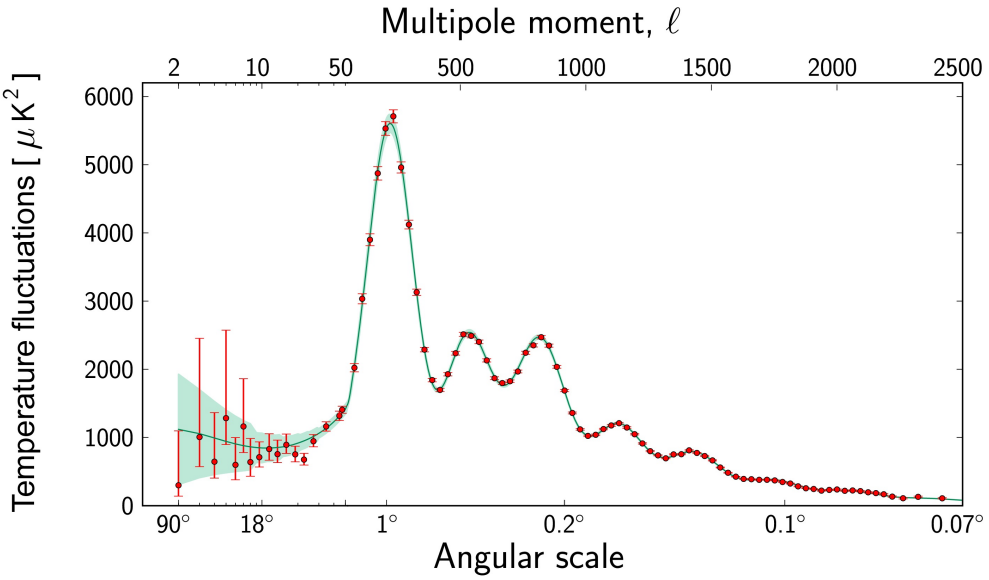


Figure 9: The power spectrum of the CMB anisotropy, where green curve represents the best fit of the ΛCDM model and the red dots correspond to measurements with error bars. Figure taken from [44]

$a_{lm}$ are independent random variables with $\langle a_{lm}\rangle = 0$. Statistically isotropic temperature fluctuations mean, that the variance of the $a_{lm}$ is independent of $m$, which are related to the orientation of the anisotropy pattern [43], thus

$$\langle a_{lm} a^*_{l'm'}\rangle = \delta_{ll'}\delta_{mm'}C_l, \tag{2.26}$$

where $\delta_{ij}$ is the Kronecker delta and averages are over statistical ensembles. The set of $C_l$'s form the angular power spectrum

$$C_l \equiv \langle |a_{lm}|^2\rangle = \frac{1}{2l+1}\sum_m \langle |a_{lm}|^2\rangle. \tag{2.27}$$

and for Gaussian fluctuations, $C_l$ describes the CMB temperature anisotropy perfectly. This is the angular power spectrum predicted from theory. The temperature variance related to the angular power spectrum gives

$$\left\langle \left(\frac{\delta T(\theta,\phi)}{T}\right)^2 \right\rangle = \left\langle \sum_{lm} a_{lm} Y_{lm}(\theta,\phi) \sum_{l'm'} a^*_{l'm'} Y^*_{l'm'}(\theta,\phi) \right\rangle = \sum_l \frac{2l+1}{4\pi} C_l, \tag{2.28}$$

where we used the closure relation (2.24). The above equation describes the expectation value of the power spectrum thus, there is no discrepancy between different set of $\theta$ and $\phi$, since the average is taken over ensemble of universes. The actual

observed value $\tilde{C}_l$, a single realization, varies with direction [43]. The $C_l$'s can be determined accurately for the inflationary models as function of the cosmological parameters [45], [46]. Therefore, comparing the measured CMB anisotropies to $C_l$, predicted by theory, will set constraints on the cosmological model and to the density of dark matter. The uncertainty of the measurement is called the cosmic variance [43]

$$\langle(\tilde{C}_l - C_l)^2\rangle = \frac{2}{2l+1}C_l, \tag{2.29}$$

where the difference between $\tilde{C}_l$ and $C_l$ becomes smaller for higher $l$ as the sample of $a_{lm}$ for calculating the $\tilde{C}_l$ becomes larger. Sample variance further increased the uncertainty by a factor of $4\pi/A$ [47], because only part of the sky can be covered within a given time. Here $A$ is the solid angle covered by the experiment.

By plotting $(2l+1)C_l/4\pi$ as of function of the multipole $l$, gives series of acoustic peaks, where the area under the curve gives the temperature variance. The power spectrum data from 2013 by Planck satellite is shown in Figure 9. The peaks arise from the oscillation of the photon-baryon fluid, when gravitational attraction and the photon pressure are both trying to overcome one another.

By setting the parameters of our cosmological model to correspond the power spectrum of temperature fluctuations in the CMB, the density of dark matter can be estimated. Because the power spectrum of the CMB anisotropy is well fitted, it provides powerful evidence in support of dark matter.

The angular power spectrum of the temperature fluctuations in the early universe defines the cosmological model. Based on CMB observations the density of the Universe is close to critical and consist mostly of dark energy and dark matter. In Figure 10 the angular power spectrum is presented by variating one of the main components of the Universe, while keeping the others at fixed values. We can see how the parameters affect the angular power spectrum, but regarding dark matter, the most important one is the variation around the matter density. If all the matter would consist of baryons, the overall height of the spectrum would be higher corresponding to much larger temperature anisotropies in the CMB at angular scales $l = 100$ to $l = 1000$.

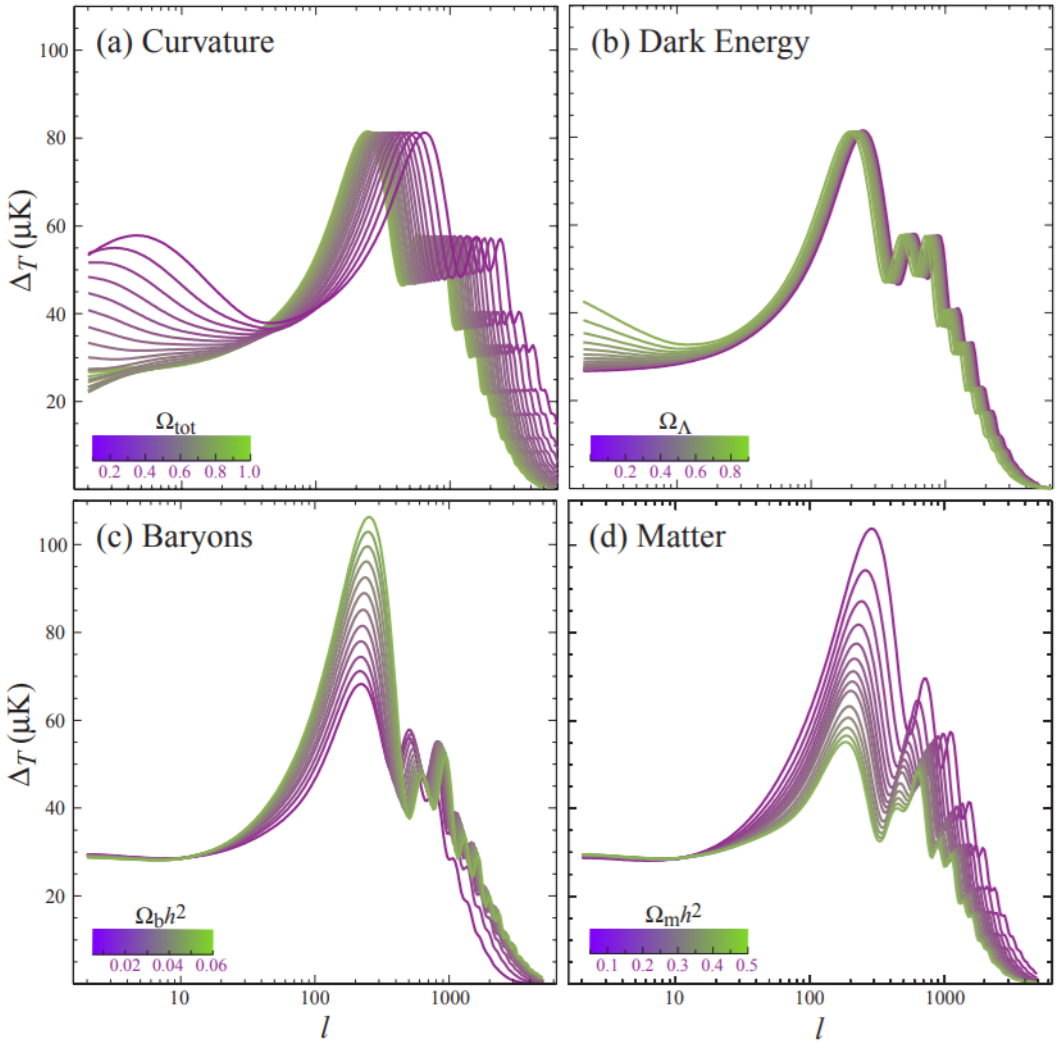


Figure 10: The angular power spectrum of temperature fluctuations with different set of parameters varied around: a) the curvature or the total energy density $\Omega_{\rm tot} = 1.0$, b) the dark energy $\Omega_\Lambda = 0.65$, c) the baryon energy density $\Omega_b h^2 = 0.02$ and the d) matter energy density $\Omega_m h^2 = 0.147$. Figure is from [3].

## 2.4 Structure formation

Galaxies, galaxy clusters and larger structures all formed from small density fluctuations in the early universe and this is referred as structure formation [10]. In an essence structure formation is an initial data problem and the CMB and the angular power spectrum gives us hints about this data, since the temperature anisotropy of CMB is connected to the density fluctuation by [10]

$$\frac{\delta T}{T} \propto \lambda \frac{\delta \rho}{\rho}, \tag{2.30}$$

where $\lambda$ = constant with values ranging from 10 to 100 depending on the scale. CMB shows that the early universe was extremely smooth with density fluctuation of $\sim 10^{-5}$. This means that the fluctuations were even smaller before photon decoupling. Today the Universe is very lumpy. Galaxy clusters are $10^2$ or even $10^3$ times as dense as the Universe and galaxies are about $10^5$ times the average density of the Universe [10]. Although there is clear difference between matter and photon distribution in the Universe, both originated from the same small density fluctuations after inflation. Structures formed through gravitational, or Jeans instability [10] from primordial density fluctuations during a inflationary epoch into larger inhomogeneities we observe today [48].

Dark matter plays important role in formation of structure, since it interacts with baryonic matter only via gravitation. Because DM is free from the radiation pressure, it can collapse and grow into complex gravitational systems well before photon decoupling, where baryonic matter can later fall. Without dark matter, formation of galaxies would occur considerably later in the cosmic timeline.

The evolution of DM perturbations and baryonic perturbations can be solved from coupled, linearized Einstein, Boltzmann and fluid equations [49]. By choosing a synchronous coordinate system or in other words a synchronous gauge [50], the spatially flat FRW metric can be written as

$$g_{\mu\nu} = \bar{g}_{\mu\nu} + \delta g_{\mu\nu}, \tag{2.31}$$

which consists of background metric $\bar{g}_{\mu\nu}$ and small perturbation $\delta g_{\mu\nu}$. For synchronous gauge $\delta g_{00} = \delta g_{i0} = 0$, however these condition do not eliminate all gauge freedom [10].

Solving the equations governing the perturbations is well beyond the scope of this thesis however, using the existing Code for Anisotropies in the Microwave Background (CAMB) library [51] the perturbation equations can be solved numerically shown in Figure 11. The photon-baryon fluid perturbations starts to oscillate after horizon entry around $a/a_0 \sim 10^{-5}$, while dark matter perturbations are free from the photon pressure. After photon decoupling around $a/a_0 \sim 10^{-3}$ baryon perturbations start to grow and quickly match DM perturbations.

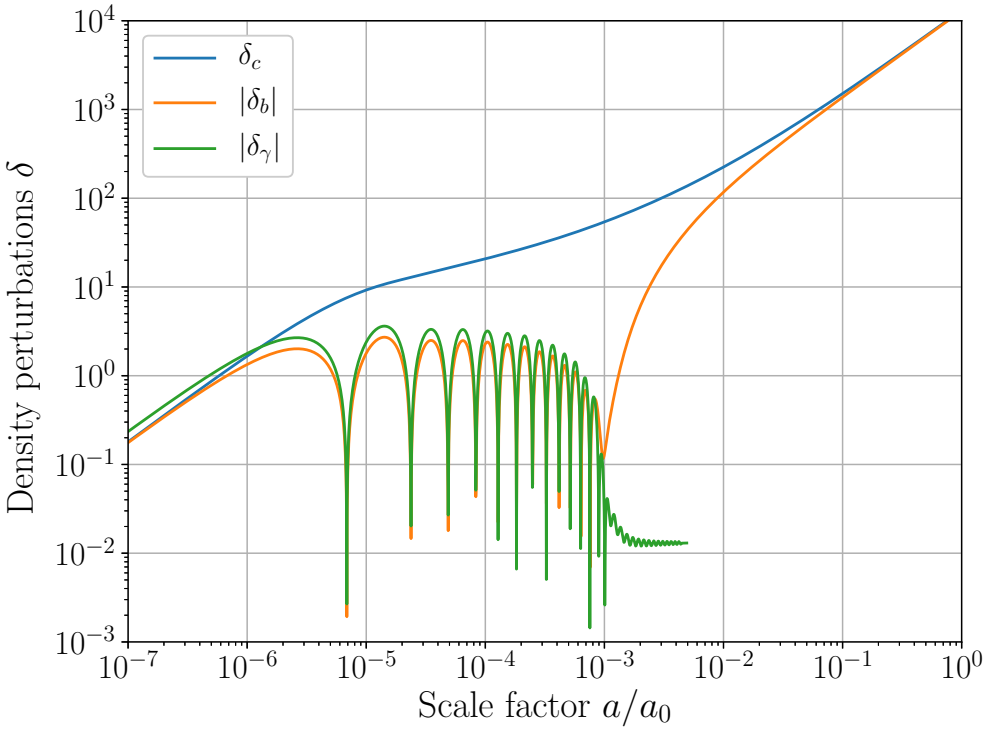


Figure 11: Evolution of the density perturbations of DM $\delta_c$, baryonic matter $\delta_b$ and radiation $\delta_\gamma$ in synchronous gauge with $H_0 = 67.4$, $\Omega_c h^2 = 0.12$, $\Omega_b h^2 = 0.022$, $A_s = 2 \times 10^{-9}$, $n_s = 0.95$ and $k = 0.3/\text{Mpc}$. We can see how the baryon perturbations start to oscillate after horizon entry around $a/a_0 \sim 10^{-5}$ and quickly grows to match the DM perturbations after photon decoupling around $a/a_0 \sim 10^{-3}$. Figure created by utilizing the CAMB library [51].

The baryon density fluctuations could not grow larger before photon decoupling. Only after the Universe became matter-dominated all matter components grow as

$$\frac{\delta\rho}{\rho} \propto \begin{cases} a(t) & \delta\rho/\rho \lesssim 1 \quad \text{(linear regime)} \\ a(t)^n \ \ (n \gtrsim 3) & \delta\rho/\rho \gtrsim 1 \quad \text{(nonlinear regime).} \end{cases} \tag{2.32}$$

CMB is consistent with perturbations of $10^{-2}$ to $10^{-3}$ and the cosmic scale factor $a(t)$ has grown bit more than a factor of $10^3$ after photon decoupling [10]. The existence of dark matter allows baryon perturbations to be small at photon decoupling and grow more than factor of $10^3$ matching the observed structure today.

# 3 WIMP and thermal freeze-out

In this section thermal relics and their generation through freeze-out mechanism are briefly discussed following the introduction of Boltzmann equation and calculations of dark matter genesis through freeze-out.

## 3.1 Baryonic dark matter

Luminous matter includes all the stars and gas clouds in the Universe, which emit observable electromagnetic radiation. However, all the luminous matter in the Universe accounts only less than 1 % of the total energy density in the Universe [10] thus, according to CMB power spectrum data

$$\Omega_l < \Omega_b < \Omega_m, \tag{3.1}$$

where $\Omega_l$ corresponds to luminous matter, $\Omega_b$ to baryonic matter, and $\Omega_m$ to the total matter in the Universe. This indicates that there are two types of dark matter, baryonic and nonbaryonic dark matter. If matter would consist solely of baryonic matter, the fluctuations in the CMB would look different as discussed in section 2.4.

Objects too faint to be seen such as neutron stars, brown dwarfs, planet like objects and even black holes are called Massive Astrophysical Compact Halo Objects (MACHO). They drift lonely through interstellar space and emit electromagnetic radiation weakly or none at all, thus MACHOs are hard to detect

Surveys such as MACHO [52] and EROS [53] were designed to test via gravitational lensing, if the dark matter halo in galaxies could consists of MACHOs. Although, the Big Bang nucleosynthesis [10] and the anisotropies in the CMB [5] have already shown that baryonic matter does not constitute all the matter in the Universe. Results from MACHO and EROS surveys further confirms that this indeed is the case. Nonbaryonic dark matter is needed, since there should have been more gravitational lensing events than what was observed according to MACHO and EROS. In this thesis, only nonbaryonic dark matter is considered and studied.

## 3.2 Nonbaryonic dark matter

Nonbaryonic dark matter can be divided into three different types depending on when they decoupled from the thermal bath [10]. Hot dark matter (HDM) de-

coupled while still relativistic, cold dark matter (CDM) decoupled while non-relativistic. Warm dark matter (WDM) has characteristics between HDM and CDM.

The main feature of HDM is that they have negligible mass compared to their thermal velocity and after freeze-out they retain large number density so that their density would correspond to dark matter density today. The most reasonable candidate for HDM in the Standard Model are neutrinos. They have small rest mass and they interact weakly via weak interaction and gravity, therefore neutrinos are extremely hard to detect.

Although neutrinos would make good HDM candidate, their rest mass is not enough for the cosmic neutrino background to have significant contribution to the total density today. Upper limit for the neutrino masses from CMB observations is [5]

$$\sum m_\nu < 0.12 \text{ eV}. \tag{3.2}$$

The cosmic neutrino background temperature $T_\nu$ is connected to the photon temperature by $T_\nu^3 = (4/11)T_\gamma^3$ [10]. Using this relation, the corresponding maximum contribution of neutrinos to the density parameter is

$$\Omega_\nu h^2 \approx \frac{\sum m_\nu}{94.46 \text{ eV}} < 0.00127, \tag{3.3}$$

which is significantly less than the density of baryonic matter $\Omega_\text{b} h^2 = 0.022$.

Large scale structure observations and structure formation theory indicate that DM is cold. The problem with HDM theory is the high velocities of the particles. Dark matter perturbations grew much larger before baryon perturbations as discussed in section 2.4. The clustering properties of DM are determined by the free streaming length $\lambda_\text{fs}$, which is the distance that a particle travels before the primordial perturbations start to grow larger around matter-radiation equality [54]

$$\lambda_\text{fs} = \int_0^{t_\text{EQ}} \frac{v(t)}{a(t)} dt. \tag{3.4}$$

In the above equation perturbations are smoothed out at length scales below the free-streaming length $\lambda_\text{fs}$ and larger scales undergo gravitational instability [55]. The integral in (3.4) can be separated into regions where particle is relativistic and non-relativistic, which leads to [54]

$$\lambda_\text{fs} \approx r_H(t_\text{NR}) \Big[ 1 + \frac{1}{2} \log \Big( \frac{t_\text{EQ}}{t_\text{NR}} \Big) \Big], \tag{3.5}$$

where $t_\text{EQ}$ is the time of matter-radiation equality, $t_\text{NR}$ is the epoch when particle becomes non-relativistic and $r_H$ is the comoving size of the horizon at $t_\text{NR}$. For

a hypothetical heavy neutrinos with mass around $m_\nu \sim 30$ eV, $\lambda_{\rm fs}$ will lead to free-streaming mass of [56], [57]

$$M_{\rm fs} = 3.2 \times 10^{15} M_\odot \left(\frac{m_\nu}{30 \text{ eV}}\right)^{-2}. \tag{3.6}$$

This is a mass scale of superclusters, which implies that all structures smaller than $10^{15} M_\odot$ would be smoothed out as the neutrinos stream out of any overdense regions. In neutrino-dominated universe superclusters would form before smaller structures, such as galaxies and galaxy clusters. This so called "top-down" scenario is inconsistent with the abundance of quasars [58] and with the actual mass limit for neutrinos. Thus, HDM theory cannot alone account for the distribution of matter that we observe today.

Based on experimental observations and the Millennium Simulation [59] the matter in the Universe consists mostly of CDM [5], which abundance is determined by the initial conditions of the early universe. CDM has been extremely successful in explaining the formation of large-scale structure with predictions in agreement with observations [60], [61]. In case of CDM the structure is formed "bottom-up" from small initial DM perturbations, which grew large while baryons were still coupled to photons. After photon decoupling baryonic matter could fall in the already existing gravitational potential wells and form larger structures earlier in the cosmic timeline.

The most common candidates for nonbaryonic dark matter are called WIMPs or Weakly Interacting Massive Particles [8]. WIMPs are CDM, which refers to dark matter particles with negligible velocities compared to their masses and decouple from the thermal bath while non-relativistic. Successful prediction of the abundances of light relics motivates to consider WIMPs as thermal relic, which have generated similarly to SM particles.

WIMPs are expected to be particles beyond the Standard Model yet to be discovered. There are multiple candidates for WIMPs. For example, the neutralino, the Lightest Supersymmetric Partner (LSP) in the Minimal Supersymmetric Standard Model (MSSM) [62]. In MSSM every Standard Model particle has a twin with the same quantum numbers except the spin, which differs by 1/2. The LSP with R-parity conservation, defined by [63]

$$P_{\rm R} = (-1)^{3(B-L)+2s}, \tag{3.7}$$

is stable. It cannot decay into SM particles, which all have opposite R-parity [63]. In the above equation $B$ is baryon number, $L$ is lepton number and $s$ is spin. In addition, it is possible that LSP is neutral and color singlet and would therefore only interact via weak interaction and gravity.

## 3.3 Boltzmann equation

In order to delve into the WIMP mechanism, we need to understand and solve the Boltzmann equation in terms of $n$, the number density of a particle species. The evolution of the phase space density $f(p^\mu, x^\mu)$ is governed by the Boltzmann equation and it can be written as [64]

$$\hat{L}\Big[f\Big] = \hat{C}\Big[f\Big]. \tag{3.8}$$

Here $\hat{L}$ is the Liouville operator, which measures the rate of change with respect to time along the fluid flow. $\hat{C}$ is the collision operator, which represents the change in particle number per unit time per phase space volume due to interactions with other particles and self-couplings.

The covariant, relativistic form of the Liouville operator is [10]

$$\hat{L} = p^\alpha \frac{\partial}{\partial x^\alpha} - \Gamma^\alpha{}_{\beta\gamma} p^\beta p^\gamma \frac{\partial}{\partial p^\alpha}, \tag{3.9}$$

where $\Gamma^\alpha_{\beta\gamma}$ are the Christoffel symbols or connection coefficients defined by the metric as

$$\Gamma^\alpha{}_{\beta\gamma} = \frac{1}{2} g^{\alpha\lambda}(\partial_\beta g_{\gamma\lambda} + \partial_\gamma g_{\lambda\beta} - \partial_\lambda g_{\beta\gamma}). \tag{3.10}$$

In FRW universe $f(p^\mu, x^\mu) = f(E, t)$ [10], [65]. Thus, the Liouville operator can be rewritten as

$$\hat{L}[f(E,t)] = E\frac{\partial f}{\partial t} - H|\vec{\mathbf{p}}|^2 \frac{\partial f}{\partial E}, \tag{3.11}$$

where we used the energy-momentum relation (1.14). Integrating equation (3.8) over the particle momenta and summing over internal degrees of freedom $g$ we get

$$\frac{g}{(2\pi)^3}\int d^3p \frac{\partial f}{\partial t} - H\frac{g}{(2\pi)^3}\int d^3p |\vec{\mathbf{p}}|^2 \frac{\partial f}{E\partial E} = \frac{g}{(2\pi)^3}\int \frac{d^3p}{E}\hat{C}[f]. \tag{3.12}$$

Rewriting 3-momentum element as $d^3p = |\vec{\mathbf{p}}|^2 dp d\Omega$ and integrating the middle term by parts with respect to momentum from 0 to $\infty$, we get

$$\frac{g}{(2\pi)^3}\int d^3p \ \frac{\partial f}{\partial t} + 3H\frac{g}{(2\pi)^3}\int d^3p f = \frac{g}{(2\pi)^3}\int \frac{d^3p}{E}\ \hat{C}[f]. \tag{3.13}$$

Comparing the above result with equation (1.16) we see that

$$\dot{n} + 3Hn = \frac{g}{(2\pi)^3}\int \frac{d^3p}{E}\ \hat{C}[f], \tag{3.14}$$

where the RHS depends on the interaction details of the particles. Equation (3.14) is the Boltzmann equation that describes the evolution of particle number density.

The density changes due to interaction described by the RHS and dilution caused by the expansion of the Universe described by the term $3Hn$.

For example, the Boltzmann equation for $2 \to 2$ process is [65]

$$\begin{aligned} \dot{n} + 3Hn = -\int & d\Pi_1 d\Pi_2 d\Pi_3 d\Pi_4 \\ & \times (2\pi)^4 \delta^{(4)}(p_1^\mu + p_2^\mu - p_3^\mu - p_4^\mu) \\ & \times \Big[ |\mathcal{M}_{12\to 34}|^2 f_1 f_2 (1 \pm f_3)(1 \pm f_4) \\ & - |\mathcal{M}_{34\to 12}|^2 f_3 f_4 (1 \pm f_1)(1 \pm f_2) \Big], \end{aligned} \tag{3.15}$$

where $d\Pi_i$ is the Lorentz invariant phase space element defined as

$$d\Pi_i \equiv \frac{g_i d^3 p_i}{(2\pi)^3 2E_i}. \tag{3.16}$$

$\mathcal{M}$ is the Lorentz invariant matrix element of the $2 \to 2$ process obtained using the Feynman rules. $p_i^\mu$ is the 4-momentum of particle $i$ and factors $(1 \pm f_i)$ describe the quantum mechanical effects of degenerate matter, where $(+)$ is for bosons and $(-)$ for fermions [10].

## 3.4 WIMP mechanism

Thermal relics are particles, which decouple from the thermal bath in the early universe when interactions rate $\Gamma$ becomes too weak and cannot keep up with the expansion rate of the Universe. Particle species are determined to be coupled when $\Gamma \gtrsim H$ and decoupled when $\Gamma \lesssim H$.

If the WIMP relic $\chi$ particle is stable, so that decays to SM particles $\chi \longrightarrow \psi\bar{\psi}$ are not allowed, $\chi$ can be DM. This can be achieved by imposing a suitable symmetry on $\chi$, such as R-parity. Provided that $\chi$ is stable, the only annihilation and inverse annihilation processes which can change the number density are

$$\chi\bar{\chi} \longleftrightarrow \psi\bar{\psi}, \tag{3.17}$$

where $\psi$ and $\bar{\psi}$ are Standard Model particles in thermal bath with $\mu_\psi = 0$. For simplicity only $2 \to 2$ process is considered, but from here it is easy to generalize to more complex interactions.

The Boltzmann equation for these processes can be simplified greatly by assuming CP invariance [66] and using Maxwell-Boltzmann statistic for all particle species [10]. CP invariance implies that

$$|\mathcal{M}_{\chi\bar{\chi}\to\psi\bar{\psi}}|^2 = |\mathcal{M}_{\psi\bar{\psi}\to\chi\bar{\chi}}|^2 = |\mathcal{M}|^2. \tag{3.18}$$

This approximation is well motivated since the only observed CP violations are in the decays of $K_2^0$ [67] and $B_s^0$ mesons [68]. Bose-Einstein and Fermi-Dirac statistics are reduced to Maxwell-Boltzmann statistic, since the temperature for each particle species satisfies $T_i \ll E_i - \mu_i$. The quantum mechanical effects can be neglected, since WIMPs can be treated as non-degenerate diluted gas. Thus, we can write Boltzmann equation for process $\chi\bar{\chi} \longleftrightarrow \psi\bar{\psi}$ as

$$\dot{n}_\chi + 3Hn_\chi \approx \int d\Pi_\chi d\Pi_{\bar{\chi}} d\Pi_\psi d\Pi_{\bar{\psi}} |\mathcal{M}|^2 (2\pi)^4 \delta^{(4)}(p_i^\mu - p_f^\mu) \Big[ f_\psi f_{\bar{\psi}} - f_\chi f_{\bar{\chi}} \Big]. \quad (3.19)$$

The energy in 4-momentum conservation imply

$$E_\chi + E_{\bar{\chi}} = E_\psi + E_{\bar{\psi}} \quad (3.20)$$

therefore

$$f_\psi f_{\bar{\psi}} = e^{-E_\psi/T} e^{-E_{\bar{\psi}}/T} = e^{-E_\chi/T} e^{-E_{\bar{\chi}}/T} = f_\chi^{\text{eq}} f_{\bar{\chi}}^{\text{eq}}. \quad (3.21)$$

Here $f_\chi^{\text{eq}}$ and $f_{\bar{\chi}}^{\text{eq}}$ are the equilibrium distributions of particles $\chi$ and $\bar{\chi}$. Therefore, it follows

$$\Big[ f_\chi f_{\bar{\chi}} - f_\psi f_{\bar{\psi}} \Big] = \Big[ f_\chi f_{\bar{\chi}} - f_\chi^{\text{eq}} f_{\bar{\chi}}^{\text{eq}} \Big]. \quad (3.22)$$

The thermally averaged cross section is defined as [10]

$$\langle \sigma v \rangle \equiv (n_\chi^{\text{eq}})^{-1} (n_{\bar{\chi}}^{\text{eq}})^{-1} \int \frac{g_\chi d^3 p_\chi}{(2\pi)^3} \frac{g_{\bar{\chi}} d^3 p_{\bar{\chi}}}{(2\pi)^3} f_\chi^{\text{eq}} f_{\bar{\chi}}^{\text{eq}} \sigma v, \quad (3.23)$$

where $n_\chi^{\text{eq}} = n_{\bar{\chi}}^{\text{eq}}$. By assuming that the $\chi$ particles will remain in kinetic equilibrium, we have

$$f_\chi(\vec{p}) = e^{\mu/T} f_\chi^{\text{eq}}(\vec{p}), \quad (3.24)$$

where the factor $e^{\mu/T}$does not depend on momentum. Using equations (3.23) and (3.24), we obtain the Lee-Weinberg equation [10]

$$\dot{n}_\chi + 3Hn_\chi = -\Big\langle \sigma v \Big\rangle \Big( n_\chi^2 - (n_\chi^{\text{eq}})^2 \Big). \quad (3.25)$$

$n_\chi^2$ describes the decrease of particles $\chi$ due to annihilations and $n_\chi^{\text{eq}}$ accounts for the pair production from thermal bath. In the thermal equilibrium they balance each other yielding $d(a^3 n_\chi)/dt = 0$ which implies $n_\chi \propto a^{-3}$ in the relativistic limit $m \ll T$. In the non-relativistic limit $m \gg T$, the pair production processes $\psi\bar{\psi} \longrightarrow \chi\bar{\chi}$ are exponentially suppressed by $n_\chi^{\text{eq}} \propto e^{-m/T}$.

Equation (3.25) can be expressed in terms of the comoving number density

$$Y \equiv \frac{n_\chi}{s}, \quad (3.26)$$

where $s$ is the entropy density. Entropy is conserved per comoving volume

$$sa^3 = \text{constant}. \tag{3.27}$$

It follows that

$$s\dot{Y} = \dot{n}_\chi + 3Hn_\chi. \tag{3.28}$$

By defining a new variable

$$x \equiv ms^{-1/3} \propto \frac{m}{T} \tag{3.29}$$

and assuming $g_{*s} = \text{constant}$, so that $T \propto a^{-1}$, we find

$$\frac{dx}{dt} = Hx. \tag{3.30}$$

Using equations (3.28) and (3.30) the Lee-Weinberg equation (3.25) can be rewritten as

$$\frac{x}{Y_{\text{eq}}}\frac{dY}{dx} = -\frac{\Gamma}{H}\Big(\frac{Y^2}{Y_{\text{eq}}^2} - 1\Big), \tag{3.31}$$

where the decay rate is defined by

$$\Gamma \equiv \langle\sigma v\rangle n_{\text{eq}}. \tag{3.32}$$

Here $Y$ is the actual number of $\chi$ and $\bar{\chi}$ particles per comoving volume and $Y_{\text{eq}}$ is the equilibrium number of $\chi$ and $\bar{\chi}$ particles per comoving volume.

Equation (3.31) clearly shows how the change of particles $\chi$ per comoving volume is controlled by factor of $\Gamma/H$ times the deviations from equilibrium. If $\Gamma \gg H$ the comoving number density $Y$ follows $Y_{\text{eq}}$. As the expansion rate of the Universe becomes larger than the interaction rate $\Gamma \ll H$, the number of particles decouple from the thermal bath and "freezes" to a constant $dY/dx = 0$. This is called the freeze-out process, which refers to the comoving number density $Y$ unable to follow $Y_{\text{eq}}$.

## 3.5 Analytical solution

Equation (3.31) can be solved using numerical methods, but we can also derive an analytical estimate for the relic abundance $Y_0$, which is the number of DM particles per comoving volume today. For non-relativistic limit (i.e. $m \gg T$) the equilibrium number density per comoving volume has the form

$$Y_{\text{eq}} = 0.145\frac{g}{g_{*s}}\Big(\frac{m}{T}\Big)^{3/2}e^{-m/T}. \tag{3.33}$$

Using the definition of $x$ (3.29) and equation for entropy density (1.28) we find

$$\frac{dY_{\rm eq}}{dx} = b\frac{dY_{\rm eq}}{d(\frac{m}{T})} = b\Big(\frac{3}{2}\frac{T}{m} - 1\Big)Y_{\rm eq} \simeq -bY_{\rm eq}, \tag{3.34}$$

where $b \approx 0.7598 g_{*s}$. Well before the freeze-out $x \ll x_f$, we have

$$\delta \equiv Y - Y_{\rm eq} \ll 1 \tag{3.35}$$

and equation (3.31) before freeze-out is

$$\frac{dY}{dx} = -\frac{\Gamma(Y - Y_{\rm eq})(Y + Y_{\rm eq})}{HxY_{\rm eq}} \simeq -\frac{2\delta\Gamma}{Hx}. \tag{3.36}$$

After freeze-out $x \gg x_f$ when $\delta \gg 1$ we find

$$\frac{dY}{dx} \simeq -\frac{\Gamma Y^2}{HxY_{\rm eq}}. \tag{3.37}$$

Equations (3.36) and (3.37) are asymptotically equivalent at $x = x_f$

$$\Gamma\frac{2\delta}{Hx_f} = \frac{\Gamma Y^2(x_f)}{Hx_f Y_{\rm eq}(x_f)} \tag{3.38}$$

$$2\delta \simeq Y_{\rm eq}(x_f). \tag{3.39}$$

Using equations (3.36) and (3.34) we can write

$$bY_{\rm eq} = \frac{2\delta\Gamma}{Hx} \tag{3.40}$$

$$\frac{2\delta}{Y_{\rm eq}} = \frac{H}{\Gamma}\frac{m}{T}. \tag{3.41}$$

Substituting equation (3.39) into equation (3.41) we get the result for freeze-out time

$$\Gamma_f = \langle\sigma v\rangle n_f^{\rm eq} \simeq H_f\Big(\frac{m}{T_f}\Big), \tag{3.42}$$

where we can see how the equilibrium number density $n_f^{\rm eq}$ is related to the freeze-out temperature $T_f$ and the decoupling time is not when $\Gamma = H$ but close.

Let us then estimate the freeze-out temperature $T_f$. Substituting the equilibrium number density at freeze-out $n_f^{\rm eq}$ into (1.20) and the Hubble parameter $H$ (1.25) into (3.42) we get

$$g\Big(\frac{mT}{2\pi}\Big)^{3/2} e^{-m/T} = \Big(\frac{g_{*\rho}\pi^2}{90M_{\rm P}^2}\Big)^{1/2}\frac{T_f^2}{\langle\sigma v\rangle_f}\frac{m}{T_f}. \tag{3.43}$$

From which we get

$$\frac{m}{T_f} = -\frac{1}{2}\ln\left(\frac{m}{T_f}\right) + \left[38 + \ln(g) - \frac{1}{2}\ln\left(\frac{g_{*\rho}}{100}\right) + \ln\left(\frac{m}{\text{GeV}}\right) + \ln\left(\frac{\langle\sigma v\rangle_f}{\text{GeV}^{-2}}\right)\right]. \quad (3.44)$$

This can be written as

$$y = -\frac{1}{2}\ln(y) + y_0(m, \langle\sigma v\rangle_f, g, g_{*\rho}), \quad (3.45)$$

where $y \equiv m/T_f$ and $y_0$ is the rest of the terms that only depend on $m, \langle\sigma v\rangle_f, g$ and $g_{*\rho}$. This can be solved iteratively by substituting $y = y_0(1+\delta y)$ into equation (3.45) and doing the Taylor expansion on $\ln(1+\delta y)$ to first order

$$y_0 + y_0\delta y = -\frac{1}{2}\ln(y_0(1+\delta y)) + y_0 \quad (3.46)$$

$$y_0\delta y = -\frac{1}{2}\ln(y_0) - \frac{1}{2}\ln(1+\delta y) \quad (3.47)$$

$$y_0\delta y \simeq -\frac{1}{2}\ln(y_0) - \frac{\delta y}{2} + \mathcal{O}(\delta y^2) \quad (3.48)$$

$$\delta y \simeq -\frac{1}{2}\frac{\ln(y_0)}{y_0}. \quad (3.49)$$

$y$ can now be written as

$$y = y_0 - \frac{1}{2}\ln(y_0), \quad (3.50)$$

which we got by doing the iteration cycle once. Taking for example a particle with a mass $m = 3$ GeV and with an annihilation cross section $\langle\sigma v\rangle = G_F^2 m^2$, where $G_F = 1.17 \times 10^{-5}$ GeV$^{-2}$ is the Fermi constant, we get

$$\frac{m}{T_f} \sim 18. \quad (3.51)$$

Let us then calculate the relic abundance $Y_0(x \to \infty)$. Since the annihilation cross section depends on velocity $\sigma v \propto v^p$ and the thermal velocity of the particles is related to temperature by $\langle v\rangle \propto T^{1/2}$. Therefore, the cross section can be parametrized as [10]

$$\langle\sigma v\rangle = \sigma_0\left(\frac{T}{m}\right)^p, \quad (3.52)$$

where $p$ correspond to a specific wave annihilation or angular quantum number ($l = 0, 1, 2\ldots$) [66].

We want to find the relation $\Gamma/Y_{\text{eq}}$ in terms of the freeze-out temperature $T_f$, therefore we may write

$$\left(\frac{\Gamma}{Y_{\text{eq}}}\right) = \left(\frac{\Gamma}{Y_{\text{eq}}}\right)_f \frac{\langle\sigma v\rangle s}{\langle\sigma v\rangle_f s_f}. \quad (3.53)$$

Using equation (3.52) and the fact that $s \propto T^3$, we can write

$$\left(\frac{\Gamma}{Y_{\mathrm{eq}}}\right) = \left(\frac{\Gamma}{Y_{\mathrm{eq}}}\right)_f \left(\frac{T}{T_f}\right)^{p+3} = \left(\frac{\Gamma}{Y_{\mathrm{eq}}}\right)_f \left(\frac{x}{x_f}\right)^{-(p+3)}. \tag{3.54}$$

The Hubble parameter can also be expressed in terms of the freeze-out temperature $T_f$

$$H = H_f \left(\frac{T}{T_f}\right)^2 = H_f \left(\frac{x}{x_f}\right)^{-2}. \tag{3.55}$$

Equation (3.37) can now be written as

$$\int_{Y_f}^{Y_0} \frac{dY}{Y^2} = -\frac{m}{T_f} \frac{x_f^{(p+1)}}{Y_{\mathrm{eq}}(x_f)} \int_{x_f}^{\infty} dx x^{-(p+2)}. \tag{3.56}$$

Integrating the above equation with respect to $Y$ and $x$ we get

$$Y_0 = \frac{T_f}{m}(p+1) Y_{\mathrm{eq}}(x_f). \tag{3.57}$$

Using equation (3.26) with the value for $n_f^{\mathrm{eq}}$ (3.42) and substituting values for entropy density $s$ (1.28) and Hubble parameter $H$ (1.25) at freeze-out, we then finally arrive at the result

$$Y_0 \approx 0.75 \frac{(p+1)}{\langle \sigma v \rangle_f} \left(\frac{\sqrt{g_{*\rho}}}{g_{*s}}\right)_f \frac{1}{M_{\mathrm{P}} T_f}. \tag{3.58}$$

The solution (3.58) shows how the relic abundance depends on the cross section. $Y_0$ becomes smaller as the cross section $\langle \sigma v \rangle_f$ becomes larger. This is because stronger interactions keep particle species longer close to the equilibrium distribution $Y_{\mathrm{eq}}$. Figure 12 shows the analytical solution for the relic abundance $Y_0$ and the numerical solutions for the Lee-Weinberg equation (3.31) with different values for the annihilation cross section.

The dark matter abundance is determined by its contribution to the total energy density today

$$\Omega_{\mathrm{DM}} = \frac{\rho_{\mathrm{DM}}}{\rho_c}. \tag{3.59}$$

The density of dark matter can be written in terms of the WIMP mass $m$, entropy density $s$ and the comoving number density $Y$

$$\rho_{\mathrm{DM}} = mn = msY. \tag{3.60}$$

Substituting the value of critical energy density $\rho_c h^{-2} = 8.1 \times 10^{-11}$ eV$^4$ and the energy density of dark matter (3.60) into (3.59) with $Y_0$ (3.58) and $s_0 = s(T_0)$

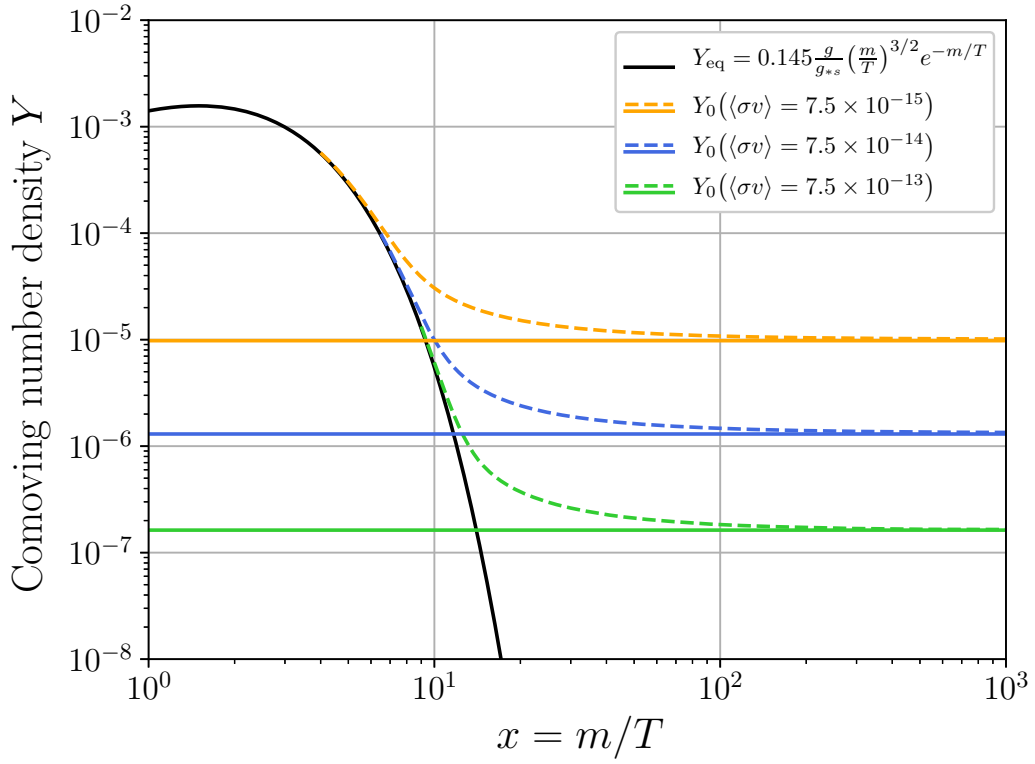


Figure 12: The evolution of the comoving number density $Y$. Increasing the annihilation cross section $\langle\sigma v\rangle$ decreases the final relic density $Y$, since stronger interactions will keep particle species longer in the equilibrium state. Dashed line corresponds to numerical solution and solid line represents the analytical solution to the Lee-Weinberg equation.

(1.28), where $T_0$ is the photon temperature today we get the analytical estimate for the WIMP dark matter energy density

$$\Omega_{\rm DM}h^2 \approx 8.5\times10^{-11}\left(\frac{m}{T_f}\right)\left(p+1\right)\left(\frac{\sqrt{g_{*\rho}}}{g_{*s}}\right)_f\left(\frac{\rm GeV^{-2}}{\langle\sigma v\rangle_f}\right). \tag{3.61}$$

As an example, dark matter with annihilation cross section near electroweak scale $\langle\sigma v\rangle \sim G_F^2 m^2$, where the Fermi constant is $G_F = 1.17\times10^{-5}$ GeV$^{-2}$ and $m \sim 3$ GeV with $g_{*\rho} \simeq g_{*s} = 75.75$ at freeze-out gives the correct dark matter energy density $\Omega_{\rm c}h^2 = 0.12$. This is referred as the "WIMP miracle".

# 4 FIMP and non-thermal freeze-in

In this section an alternative mechanism for dark matter genesis is introduced, called non-thermal freeze-in, and compared to previously introduced thermal freeze-out. After the general overview of the mechanism, a few simple production channels are presented, and density of dark matter calculated for each case from the Boltzmann equation. Lastly, as an example, freeze-in mechanism is applied to a specific sterile neutrino dark matter model.

## 4.1 FIMP mechanism

Most theories of dark matter are based on thermal freeze-out [8], [10], where dark matter particles or WIMPs have large initial number density in thermal bath. As the temperature in the early universe drops below the mass of DM particle due to the expansion of the Universe, annihilation to lighter species become smaller and eventually cease completely. Thus, the comoving number density of dark matter particles "freezes" to a constant.

Large annihilation cross section generates less dark matter since more particles are able to annihilate and follow the equilibrium distribution longer as illustrated in Figure 12. Freeze-out mechanism typically occurs at a temperature around a factor of 20–30 below the mass of the dark matter particle.

There exist many alternative non-thermal production mechanisms for DM and one of them is called freeze-in [9]. In the early universe Standard Model particles are in thermal equilibrium. Suppose there is a particle FIMP $\chi$ (Feebly Interacting Massive Particle), which is decoupled from the thermal bath, since its interactions with SM particles are extremely weak. Although the interactions are weak they may lead to some $\chi$ production via decays of the bath particles. Assume that the initial abundance of $\chi$ is small for example due to inflation. The dominant production of $\chi$ occurs as the temperature drops below the mass of the decaying particle [9]. The comoving number density of $\chi$ "freezes-in" to a constant as the Universe expands and cools. The density of $\chi$ increases as the interaction strength increases. Freeze-in occurs at a temperature around a factor of 2–5 below the mass of the decaying particle.

Comparing the freeze-out and freeze-in mechanisms, they can be viewed as opposite of each other. Thermal number density of dark matter particles is large at the beginning of freeze-out process. Reducing the annihilation cross section will

result in a larger DM density. Freeze-in starts with negligible initial dark matter abundance and increasing the interaction strength, increases the final DM density. For all normalizable interactions the final abundance for freeze-in is [9]

$$Y_{FI} \propto \lambda^2 \Big( \frac{M_{\mathrm{P}}}{m} \Big), \tag{4.1}$$

where $\lambda$ is the interaction strength and $m$ is the mass of the decaying particle. In contrast to freeze-out the final abundance is

$$Y_{FO} \propto \frac{1}{\Lambda^2} \Big( \frac{M}{M_{\mathrm{P}}} \Big), \tag{4.2}$$

where $M$ is the mass of the DM particle and $\Lambda$ is the required interaction strength which is proportional to the cross section $\Lambda^2 \propto \sigma v M^2$ in the simple case [9].

Whether dark matter is produced through freeze-out or freeze-in mechanism, it is always depends on the coupling and mass of the DM particle, but in the case on FIMP dark matter, the final DM density also depends on the couplings and masses of the particles in the thermal bath. For example, in weak scale supersymmetry theories depending on the mass, FIMP could be the DM particle or alternatively the LSP is the DM particle produced via decays of "frozen-in" FIMPs [9].

Despite the different features, there are couple fundamental common features which are required from these two mechanisms. The final relic abundance can be calculated solely from an initial state of bath particles which are in thermal equilibrium, given the masses and couplings of the particles in thermal bath and in dark sector. In addition, the production of dark matter particles is dominated by temperatures near the mass of dark matter and is independent of quantities such as the reheat temperature after inflation [9].

Through neutrino oscillations experiments [69] we know that neutrinos have mass although very small compared to other SM particles. Since $m_\nu \neq 0$ physics beyond SM is needed and it motivates to consider heavy sterile neutrinos as DM, which can also explain the masses of SM neutrinos. Dodelson and Widrow were the first ones to propose sterile neutrinos as dark matter [70]. Sterile neutrino with mass lying in the keV range could be produced through neutrino oscillations between active neutrinos and sterile neutrinos via Dodelson-Widrow (DW) mechanism. Today we know from astrophysical observations, that this type of dark matter produced by DW mechanism cannot make up all the dark matter in the Universe [71]–[74]. This encourages to consider different kind of sterile neutrino production mechanism such as freeze-in, where sterile neutrinos are colder compared to DW and not produced from mixing with active neutrinos and alleviate the constraints from X-ray and Lyman-$\alpha$ observations [75].

## 4.2 FIMP production via $1 \to 2$ decay

Decays or inverse decays of bath particles dominate the freeze-in abundance of FIMP dark matter depending on the masses of the particles. Contributions from scatterings like $2 \to 2$ are sub-dominant [9].

The analysis in this and the following two sections closely follow [9][1]. In the simple case, the freeze-in production is dominated by $1 \to 2$ decays. For this production channel consider that the FIMP $\chi$ is the dark matter particle and coupled to two bath particles $\psi_1$ and $\psi_2$ through $\lambda\chi\psi_1\psi_2$. If $m_{\psi_1} > m_{\psi_2} + m_\chi$, the dominant process of freeze-in is [9]

$$\psi_1 \to \psi_2 + \chi. \tag{4.3}$$

The density of dark matter can be calculated by solving the Boltzmann equation (3.14). For $1 \to 2$ process the equation becomes

$$\begin{aligned} \dot{n}_\chi + 3Hn_\chi = \int d\Pi_{\psi_1} d\Pi_{\psi_2} d\Pi_\chi (2\pi)^4 \delta^{(4)}(p^\mu_\chi + p^\mu_{\psi_2} - p^\mu_{\psi_1}) \\ \times \Big[ |\mathcal{M}_{\psi_1 \to \psi_2 \chi}|^2 f_{\psi_1}(1 \pm f_{\psi_2})(1 \pm f_\chi) \\ - |\mathcal{M}_{\psi_2 \chi \to \psi_1}|^2 f_{\psi_2} f_\chi (1 \pm f_{\psi_1}) \Big]. \end{aligned} \tag{4.4}$$

The above Boltzmann equation can be simplified by assuming CP invariance and using Maxwell-Boltzmann statistics as was done in section 3.4. Furthermore, freeze-in mechanism requires, that the initial $\chi$ abundance is negligible, thus we can set $f_\chi = 0$. Therefore, the Boltzmann equation is reduced to

$$\dot{n}_\chi + 3Hn_\chi \approx \int d\Pi_{\psi_1} d\Pi_{\psi_2} d\Pi_\chi (2\pi)^4 \delta^{(4)}(p^\mu_\chi + p^\mu_{\psi_2} - p^\mu_{\psi_1}) |\mathcal{M}|^2 f_{\psi_1}. \tag{4.5}$$

Using the definition of decay rate $\Gamma_{\psi_1}$ (see section A.1) the Boltzmann equations can be written as

$$\dot{n}_\chi + 3Hn_\chi = 2 \int d\Pi_{\psi_1} \Gamma_{\psi_1} m_{\psi_1} f_{\psi_1} = \int \frac{g_{\psi_1} d^3 p_{\psi_1}}{(2\pi)^3 E_{\psi_1}} \Gamma_{\psi_1} m_{\psi_1} f_{\psi_1}. \tag{4.6}$$

By writing the momentum element as $d^3 p_{\psi_1} = |\vec{\mathbf{p}}|^2_{\psi_1} dp_{\psi_1} d\Omega$ and integrating over $d\Omega$, the integral over momentum space can be written as integral over energy

$$\dot{n}_\chi + 3Hn_\chi = \frac{g_{\psi_1} m_{\psi_1} \Gamma_{\psi_1}}{2\pi^2} \int_{m_{\psi_1}}^\infty (E^2_{\psi_1} - m^2_{\psi_1})^{1/2} e^{-E_{\psi_1}/T} dE_{\psi_1}. \tag{4.7}$$

Equation (4.7) can be solved in terms of special functions (see section C.1), therefore the Boltzmann equation can be written as

$$\dot{n}_\chi + 3Hn_\chi = \frac{g_{\psi_1} m^2_{\psi_1} \Gamma_{\psi_1}}{2\pi^2} T K_1(m_{\psi_1}/T), \tag{4.8}$$

[1] Calculations in [9] were more closely examined in [76].

where $K_1(m_{\psi_1}/T)$ is the first modified Bessel function of the second kind.

Substituting (3.28) into equation (4.8) and assuming that $g_{*\rho}$ is constant, so that $\dot{T} = -HT$, we get

$$Y_\chi = \int_{T_{min}}^{T_{max}} \frac{g_{\psi_1} m_{\psi_1}^2 \Gamma_{\psi_1}}{2\pi^2} \frac{K_1(m_{\psi_1}/T)}{sH} dT. \tag{4.9}$$

With the entropy density $s$ (1.28) and the Hubble parameter $H$ (1.25) we get

$$Y_\chi = \int_{T_{min}}^{T_{max}} \frac{g_{\psi_1} m_{\psi_1}^2 \Gamma_{\psi_1}}{2\pi^2} \frac{45}{2\pi^2 g_{*s} T^3} \left(\frac{90 M_{\mathrm{P}}^2}{g_{*\rho}\pi^2}\right)^{1/2} \frac{K_1(m_{\psi_1}/T)}{T^2} dT. \tag{4.10}$$

By defining a new variable

$$x \equiv m_{\psi_1}/T \tag{4.11}$$

we find

$$\frac{dT}{dx} = -\frac{T^2}{m_{\psi_1}} \tag{4.12}$$

therefore, equation (4.10) can be expressed in terms of $x$

$$Y_\chi = \left(\frac{90}{\pi^2}\right)^{1/2} \frac{45}{4\pi^4} \frac{g_{\psi_1} M_{\mathrm{P}} \Gamma_{\psi_1}}{m_{\psi_1}^2 g_{*s}\sqrt{g_{*\rho}}} \int_{x_{min}}^{x_{max}} K_1(x) x^3 dx. \tag{4.13}$$

Using limits $x_{min} = 0$ and $x_{max} = \infty$, equation (4.13) can be solved in terms of special functions (see section C.1) to yield

$$Y_\chi = \left(\frac{90}{\pi^2}\right)^{1/2} \frac{45}{4\pi^4} \frac{g_{\psi_1} M_{\mathrm{P}} \Gamma_{\psi_1}}{m_{\psi_1}^2 g_{*s}\sqrt{g_{*\rho}}} \frac{3\pi}{2}. \tag{4.14}$$

Finally the comoving number density for $1 \to 2$ process produced via freeze-in mechanism is

$$Y_\chi = \frac{405\sqrt{10} g_{\psi_1}}{8\pi^4 g_{*s}\sqrt{g_{*\rho}}} \left(\frac{M_{\mathrm{P}} \Gamma_{\psi_1}}{m_{\psi_1}^2}\right). \tag{4.15}$$

The DM density parameter is defined by (3.59). After substituting expressions for entropy density $s_0 = s_0(T_0)$ (1.28) and for the comoving number density $Y_0$ (4.15) we finally obtain the expression for the dark matter density

$$\Omega_{\mathrm{DM}} h^2 \approx \frac{1.09 \times 10^{27} g_{\psi_1}}{g_{*s}\sqrt{g_{*\rho}}} \frac{m_\chi \Gamma_{\psi_1}}{m_{\psi_1}^2}. \tag{4.16}$$

Substituting the value for the decay rate $\Gamma_{\psi_1} = \lambda^2 m_{\psi_1}/8\pi$ [9] and using $\Omega_{\mathrm{DM}} = 0.12$ [5] we can solve the interaction strength $\lambda$

$$\lambda \approx 5.25 \times 10^{-13} \left(\frac{m_{\psi_1}}{m_\chi}\right)^{1/2} \left(\frac{g_{*s}\sqrt{g_{*\rho}}}{10^2}\right)^{1/2}. \tag{4.17}$$

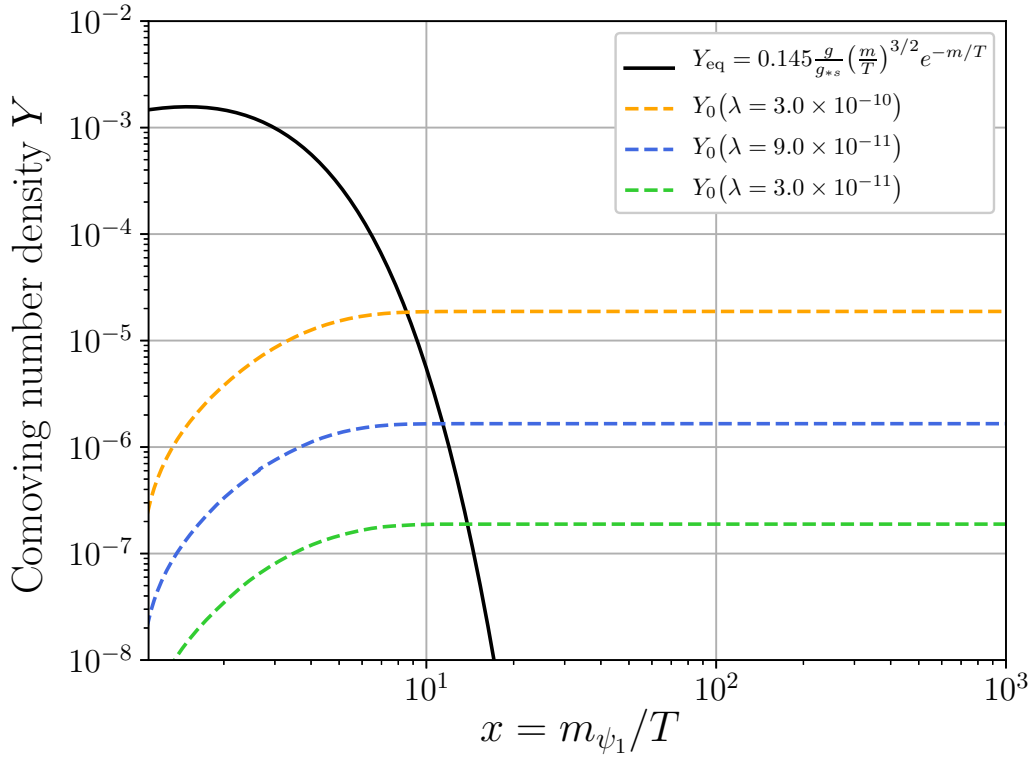


Figure 13: The evolution of the comoving number density $Y$ produced by freeze-in mechanism for $1 \to 2$ decay. Increasing the interaction strength $\lambda$, increases the final density $Y$.

As we can see from equation (4.16), we only need to know the masses of $\chi$ and $\psi_1$ and the required coupling $\lambda$, in order to determine the density of dark matter. From (4.17) we can see that the required interaction strength is extremely small. Numerical solution to the comoving number density (4.15) is shown in Figure 13. Increasing the interaction strength $\lambda$, increases the final dark matter abundance.

## 4.3 DM produced by decays of FIMPs

Another possibility is that the FIMP, which freezes-in is unstable and decays to dark matter if mass of the FIMP is greater than the mass of the DM particle. Consider a FIMP $\chi$ coupled to two bath particles again through $\lambda\chi\psi_1\psi_2$. For $m_\chi > m_{\psi_1} + m_{\psi_2}$, the production of dark matter is then dominated by inverse decays of $\chi$

$$\psi_1 + \psi_2 \to \chi, \tag{4.18}$$

where $\psi_1$ is the DM particle. The Boltzmann equation for $2 \to 1$ process is

$$\begin{aligned}\dot{n}_\chi + 3Hn_\chi = & \int d\Pi_\chi d\Pi_{\psi_1} d\Pi_{\psi_2} (2\pi)^4 \delta^{(4)}(p^\mu_\chi - p^\mu_{\psi_1} - p^\mu_{\psi_2}) \\ & \times \Big[ |\mathcal{M}_{\psi_1\psi_2\to\chi}|^2 f_{\psi_1} f_{\psi_2}(1 \pm f_\chi) \\ & - |\mathcal{M}_{\chi\to\psi_1\psi_2}|^2 f_\chi (1 \pm f_{\psi_1})(1 \pm f_{\psi_2}) \Big].\end{aligned} \tag{4.19}$$

The above equation can be again simplified as in previous section. Thus, the Boltzmann equation is reduced to

$$\dot{n}_\chi + 3Hn_\chi = \int d\Pi_\chi d\Pi_{\psi_1} d\Pi_{\psi_2} (2\pi)^4 \delta^{(4)}(p^\mu_\chi - p^\mu_{\psi_1} - p^\mu_{\psi_2}) |\mathcal{M}|^2 f_{\psi_1} f_{\psi_2}. \tag{4.20}$$

Energy is conserved, thus

$$f_{\psi_1} f_{\psi_2} = e^{-E_1/T} e^{-E_2/T} = e^{-(E_1+E_2)/T} = e^{-E_\chi/T} = f^{eq}_\chi. \tag{4.21}$$

The Boltzmann equation can be rewritten as

$$\dot{n}_\chi + 3Hn_\chi \approx \int d\Pi_\chi d\Pi_{\psi_1} d\Pi_{\psi_2} (2\pi)^4 \delta^{(4)}(p^\mu_\chi - p^\mu_{\psi_1} - p^\mu_{\psi_2}) |\mathcal{M}|^2 f^{eq}_\chi. \tag{4.22}$$

Comparing equations (4.22) and (4.5) we can immediately write down the solution for the comoving number density

$$Y_{\psi_1} = \frac{405\sqrt{10} g_\chi}{8\pi^4 g_{*s}\sqrt{g_{*\rho}}} \Big( \frac{\Gamma_\chi M_{\rm P}}{m^2_\chi} \Big), \tag{4.23}$$

where $\Gamma_\chi$ is the decay rate of $\chi \to \psi_1 + \psi_2$. Here $\psi_1$ is the dark matter particle, which decouples from the thermal equilibrium. It is then necessary to assume that the freeze-out abundance of $\psi_1$ is dominated by decays of $\chi$.

The density parameter of dark matter is obtained from (3.59) to yield

$$\Omega_{\rm DM} h^2 = \frac{1.09 \times 10^{27} g_\chi}{g_{*s}\sqrt{g_{*\rho}}} \frac{m_{\psi_1}\Gamma_\chi}{m^2_\chi}. \tag{4.24}$$

It is essential to assume that the decay of $\chi \to \psi_1 + \psi_2$ happens after the freeze-out of $\psi_1$ so that the density does not change. Substituting $\Gamma_\chi = \lambda^2 m_\chi / 8\pi$ [9] and $\Omega_{\rm DM} h^2 = 0.12$ [5] into (4.24), we obtain the required interaction strength

$$\lambda \approx 5.25 \times 10^{-13} \Big( \frac{m_\chi}{m_{\psi_1}} \Big)^{1/2} \Big( \frac{g_{*s}\sqrt{g_{*\rho}}}{10^2} \Big)^{1/2}. \tag{4.25}$$

## 4.4 FIMP production via $2 \to 2$ scattering

In this case the FIMP $\chi$ is a scalar and interacts with three scalar bath particles $\psi_1, \psi_2$ and $\psi_3$ through $\lambda\chi\psi_1\psi_2\psi_3$. The freeze-in production of DM is dominated by contributions from

$$\psi_i + \psi_j \to \psi_k + \chi \quad \text{for} \quad i, j, k = \{1, 2, 3\}. \tag{4.26}$$

The comoving number density of DM produced by freeze-in can be calculated using the Boltzmann equation

$$\dot{n}_\chi + 3Hn_\chi \approx 3 \int d\Pi_\chi d\Pi_{\psi_1} d\Pi_{\psi_2} d\Pi_{\psi_3} (2\pi)^4 \delta^{(4)}(p_i^\mu - p_f^\mu) |M_{\psi_1\psi_2 \to \psi_3\chi}|^2 f_{\psi_1} f_{\psi_2}, \tag{4.27}$$

where the factor 3 comes from the fact that there can be $\psi_1\psi_2 \to \psi_3\chi$, $\psi_1\psi_3 \to \psi_2\chi$ and $\psi_2\psi_3 \to \psi_1\chi$ contributions to the DM abundance with the same rate. $\chi\psi_i \to \psi_j\psi_k$ scatterings are very unlikely to happen and are suppressed.

Let us define a new variable

$$\xi = \int d\Pi_\chi d\Pi_{\psi_3} (2\pi)^4 \delta^{(4)}(p_{\psi_1}^\mu + p_{\psi_2}^\mu - p_{\psi_3}^\mu - p_\chi^\mu). \tag{4.28}$$

4-momentum conservation can be written as energy conservation and 3-momentum conservation denoted by $p$

$$\xi = \frac{1}{16\pi^2} \int \delta(E_{\psi_1} + E_{\psi_2} - E_{\psi_3} - E_\chi) \delta^{(3)}(p_{\psi_1} + p_{\psi_2} - p_{\psi_3} - p_\chi) \frac{d^3 p_{\psi_3} d^3 p_\chi}{E_{\psi_3} E_\chi}. \tag{4.29}$$

Integrating over $p_{\psi_3}$ we get

$$\xi = \frac{1}{16\pi^2} \int \delta\Big(E_{\psi_1} + E_{\psi_2} - \sqrt{m_{\psi_3}^2 + p_{\psi_3}^2} - \sqrt{m_\chi^2 + p_\chi^2}\Big) \frac{d^3 p_\chi}{E_{\psi_3} E_\chi}. \tag{4.30}$$

We can express the 3-momentum element as $d^3 p_\chi = p_\chi^2 dp_\chi d\Omega$. Integrating over $d\Omega$ and writing $p_{\psi_3} = -p_\chi = p$ we get

$$\xi = \frac{1}{4\pi} \int \delta\Big(\sqrt{s'} - \sqrt{m_{\psi_3}^2 + p^2} - \sqrt{m_\chi^2 + p^2}\Big) \frac{p^2 dp}{E_{\psi_3} E_\chi}, \tag{4.31}$$

where $s'$ is the Mandelstam variable for center of mass energy, which is defined as

$$s' \equiv (p_{\psi_1}^\mu + p_{\psi_2}^\mu)^2 = (E_{\psi_1} + E_{\psi_2})^2 \tag{4.32}$$

in CMS frame. Equation (4.31) is similar to equation (A.6), thus we can write $\xi$ as

$$\xi = \frac{1}{4\pi} \frac{P_{\chi\psi_3}}{\sqrt{s'}}, \tag{4.33}$$

where $P_{ij}$ is

$$P_{ij} \equiv \frac{\sqrt{\left[s' - (m_i + m_j)^2\right]\left[s' - (m_i - m_j)^2\right]}}{2\sqrt{s'}}. \tag{4.34}$$

Using the solution for $\xi$ the Boltzmann equation can be expressed as

$$\dot{n}_\chi + 3Hn_\chi = \frac{3|\mathcal{M}|^2}{4\pi} \int d\Pi_{\psi_1} d\Pi_{\psi_2} f_{\psi_1} f_{\psi_2} \frac{P_{\psi_3\chi}}{\sqrt{s'}}. \tag{4.35}$$

Substituting the values for $d\Pi_i$ and $f_i$, we get

$$\dot{n}_\chi + 3Hn_\chi = \frac{3|\mathcal{M}|^2}{4\pi} \int \frac{P_{\psi_3\chi}}{\sqrt{s'}} \frac{d^3p_{\psi_1}}{(2\pi)^3 2E_{\psi_1}} \frac{d^3p_{\psi_2}}{(2\pi)^3 2E_{\psi_2}} e^{-E_{\psi_1}/T} e^{-E_{\psi_2}/T}. \tag{4.36}$$

The volume element can be written as

$$d^3p_{\psi_1} d^3p_{\psi_2} = 8\pi^2 p_{\psi_1} p_{\psi_2} E_{\psi_1} E_{\psi_2} dE_{\psi_1} dE_{\psi_2} d\cos\theta. \tag{4.37}$$

By changing variables to [77]

$$\begin{cases} E_+ = E_{\psi_1} + E_{\psi_2}, \\ E_- = E_{\psi_1} - E_{\psi_2}, \\ s' = m_{\psi_1}^2 + m_{\psi_2}^2 + 2E_{\psi_1}E_{\psi_2} - 2p_{\psi_1}p_{\psi_2}\cos\theta \end{cases} \tag{4.38}$$

the Lorentz invariant phase space element can be written as (see section B.1)

$$\frac{d^3p_{\psi_1}}{(2\pi)^3 2E_{\psi_1}} \frac{d^3p_{\psi_2}}{(2\pi)^3 2E_{\psi_2}} = \frac{dE_+ dE_- ds'}{128\pi^4}. \tag{4.39}$$

The integration limits $\{E_{\psi_1} \geq m_{\psi_1}, E_{\psi_2} \geq m_{\psi_2}, |\cos\theta| \leq 1\}$ transforms into [77] (see section B.2)

$$s' \geq (m_{\psi_1} + m_{\psi_2})^2, \tag{4.40}$$

$$E_+ \geq \sqrt{s'}, \tag{4.41}$$

$$\left| E_- - E_+ \frac{m_{\psi_1}^2 - m_{\psi_2}^2}{s'} \right| \leq 2P_{\psi_1\psi_2} \sqrt{\frac{E_+^2 - s'}{s'}}. \tag{4.42}$$

Using the new variables the Boltzmann equation can be expressed as

$$\dot{n}_\chi + 3Hn_\chi = \frac{3|\mathcal{M}|^2}{512\pi^5} \int \frac{ds'}{\sqrt{s'}} P_{\psi_3\chi} \int dE_- \int e^{-E_+/T} dE_+. \tag{4.43}$$

We can now integrate over $dE_-$, since the product of equilibrium distribution functions depends only on $E_+$

$$\dot{n}_\chi + 3Hn_\chi = \frac{3|\mathcal{M}|^2}{512\pi^5}\int \frac{ds'}{s'} 4P_{\psi_3\chi}P_{\psi_1\psi_2}\int(\sqrt{E_+^2 - s'})e^{-E_+/T}dE_+. \tag{4.44}$$

The integral over $E_+$ gives first modified Bessel function of the second kind

$$\dot{n}_\chi + 3Hn_\chi = \frac{3T|\mathcal{M}|^2}{512\pi^5}\int \frac{ds'}{\sqrt{s'}} 4P_{\psi_3\chi}P_{\psi_1\psi_2}K_1(\sqrt{s'}/T). \tag{4.45}$$

The masses $\psi_1, \psi_2$ and $\psi_3$ are negligible compared to the mass of FIMP $\chi$, thus we can approximate $P_{\chi\psi_3}P_{\psi_1\psi_2} \approx (s' - m_\chi^2)/4$. Setting $|\mathcal{M}|^2 = \lambda^2$ [9] we get

$$\dot{n}_\chi + 3Hn_\chi \approx \frac{3T\lambda^2}{512\pi^5}\int_{m_\chi^2}^{\infty} ds'(s' - m_\chi^2)K_1(\sqrt{s'}/T)/\sqrt{s'}. \tag{4.46}$$

Doing the integral over $s'$ in terms of special functions (see section C.1) we obtain

$$\dot{n}_\chi + 3Hn_\chi = \frac{3T^3\lambda^2}{128\pi^5}m_\chi K_1(m_\chi/T). \tag{4.47}$$

Expressing this in terms of the comoving number density $Y_\chi$ we get

$$\frac{dY_\chi}{dT} = -\frac{3\lambda^2T^2m_\chi}{sH}\frac{K_1(m_\chi/T)}{128\pi^5}. \tag{4.48}$$

Substituting values for entropy density $s$ (1.28) and Hubble parameter $H$ (1.25) we obtain

$$\frac{dY_\chi}{dT} = -\frac{405\sqrt{10}M_{\rm P}\lambda^2}{256\pi^8}\frac{m_\chi K_1(m_\chi/T)}{T^3 g_{*s}\sqrt{g_{*\rho}}}. \tag{4.49}$$

The above equation can be written as integral over $x = m_\chi/T$ with limits $x = 0$ to $x = \infty$

$$Y_\chi = \frac{405\sqrt{10}\lambda^2 M_{\rm P}}{256\pi^7 g_{*s}\sqrt{g_{*\rho}}m_\chi}\int_0^\infty xK_1(x)dx. \tag{4.50}$$

Equation (4.50) can be solved in terms of special functions (see section C.1) to yield the comoving number density for $2 \to 2$ scattering process produced through freeze-in

$$Y_\chi = \frac{405\sqrt{10}\lambda^2 M_{\rm P}}{512\pi^7 g_{*s}\sqrt{g_{*\rho}}m_\chi}. \tag{4.51}$$

Using equation (3.59) and substituting all the relevant values, the dark matter density is

$$\Omega_{\rm DM}h^2 \approx \frac{5.51\times10^{23}}{g_{*s}\sqrt{g_{*\rho}}}\lambda^2. \tag{4.52}$$

Comparing equation (4.52) to (4.16) and (4.24), we can clearly see how the DM production from $2 \to 2$ scatterings is suppressed by order of $10^4$. The coupling strength $\lambda$ can be solved using $\Omega_{\rm DM}h^2 = 0.12$ to yield

$$\lambda \approx 4.67 \times 10^{-12}\left(\frac{g_{*s}\sqrt{g_{*\rho}}}{10^2}\right)^{1/2}. \tag{4.53}$$

The Dark matter density produced via freeze-in mechanism can be determined if the initial couplings and masses of the relevant particles are known. Coupling are extremely small and contributions from $2 \to 2$ scattering are sub-dominant and decay channels dominate the production of DM.

## 4.5 Freeze-in and $\mathrm{U(1)_{B\text{-}L}}$ model

One popular dark matter candidate is the sterile neutrino, which was discussed in section 4.1. As an example, we will go through how the freeze-in mechanism is applied to a specific sterile neutrino model called $\mathrm{U(1)_{B\text{-}L}}$ [78]. This extension for SM is one of many models, but it is simple and well-motivated extension, since it explains the nonzero neutrino mass through Type-I see-saw mechanism [78].

The Standard Model is based on the gauge group $\mathrm{SU(3)_c}\times\ \mathrm{SU(2)_L}\times\mathrm{U(1)_Y}$. In this model an additional $\mathrm{U(1)_{B-L}}$ symmetry is imposed to the group, where B corresponds to the baryon number and L to the lepton number of a particle. This new gauge group requires three additional right-handed neutrinos $(N_1, N_2, N_3)$, extra gauge boson $Z_{\rm BL}$ and a complex scalar singlet $\Psi$, with B – L charge of +2 [79], [80]. Spontaneous breaking of the additional symmetry by the vacuum expectation value (VEV) of $\Psi$ generates masses for the three right-handed neutrinos.

The Higgs doublet $\Phi$ and the singlet $\Psi$ are

$$\Phi = \begin{pmatrix} 0 \\ \frac{\phi+v}{\sqrt{2}} \end{pmatrix}, \qquad \Psi = \frac{\psi + v_{\rm BL}}{\sqrt{2}} \tag{4.54}$$

after obtaining VEVs $v$ and $v_{\rm BL}$ respectively. The langrangian of the scalar sector is given by [78]

$$\mathcal{L}_{\rm scalar} = (D_{\phi\mu}\Phi)^\dagger(D_\phi{}^\mu\Phi) + (D_{\psi\mu}\Psi)^\dagger(D_\psi{}^\mu\Psi) - V(\Phi,\Psi), \tag{4.55}$$

where the covariant derivatives of $\Phi$ and $\Psi$ are

$$D_{\phi\mu}\Phi = \left(\partial_\mu + i\frac{g}{2}\sigma^a W_{a\mu} + i\frac{g'}{2}B_\mu\right)\Phi \tag{4.56}$$

$$D_{\phi\mu}\Psi = \left(\partial_\mu + iQ_{\rm BL}(\Psi)g_{\rm BL}Z_{{\rm BL}\mu}\right)\Psi. \tag{4.57}$$

Here $Q_{\rm BL}(\Psi)$ is the B – L charge of $\Psi$. The Couplings $g$, $g'$ and $g_{\rm BL}$ corresponds to $\mathrm{SU(2)_L}$, $\mathrm{U(1)_Y}$ and $\mathrm{U(1)_{B–L}}$ respectively and their gauge fields are $W_{a\mu}$ $(a = 1, 2, 3)$, $B_\mu$ and $Z_{{\rm BL}\mu}$. The potential is

$$\begin{aligned} V(\Phi, \Psi) = \mu_1^2(\Phi^\dagger\Phi) + \lambda_1(\Phi^\dagger\Phi)^2 + \mu_2^2(\Psi^\dagger\Psi) \\ + \lambda_2(\Psi^\dagger\Psi)^2 + \lambda_3(\Phi^\dagger\Phi)(\Psi^\dagger\Psi). \end{aligned} \tag{4.58}$$

After the spontaneous symmetry breaking we get two scalar fields $h$ and $H$. The $h$ is the SM Higgs and $H$ is the extra heavy Higgs of the model. They can be expressed as a linear combination of $\phi$ and $\psi$

$$\begin{pmatrix} h \\ H \end{pmatrix} \begin{pmatrix} \cos\theta & -\sin\theta \\ \sin\theta & \cos\theta \end{pmatrix} \begin{pmatrix} \phi \\ \psi \end{pmatrix}. \tag{4.59}$$

Here $\theta$ is the mixing angle between $h$ and $H$. Extra kinetic term is added to the lagrangian

$$\mathcal{L}_{\rm gauge} = \mathcal{L}^{SM}_{\rm gauge} - \frac{1}{4} Z'_{\mu\nu} Z'^{\mu\nu}, \tag{4.60}$$

where the field strength tensor $Z'^{\mu\nu}$ for an abelian gauge field is defined by

$$Z'^{\mu\nu} = \partial^\mu {Z_{\rm BL}}^\nu - \partial^\nu {Z_{\rm BL}}^\mu. \tag{4.61}$$

Lagrangian for the extra right-handed neutrinos is

$$\mathcal{L}_{\rm RH} = i \sum_{i=1}^{3} \bar{N}_i \not{D}_N N_i - \lambda_{R_i} \bar{N}_i^c N_i \Psi + \sum_{\alpha=1}^{3} \sum_{i=1}^{3} y_{\alpha i} \bar{L}_\alpha \tilde{\Phi} N_i, \tag{4.62}$$

where $\tilde{\Phi} = -i\tau_2 \Phi^*$ and $\not{D}_n = \gamma_\mu D_N^\mu$, where the covariant derivative for the right-handed neutrino $N_i$ is

$$D_N^\mu N_i = (\partial_\mu - i g_{\rm BL} Z_{{\rm BL}\mu}) N_i. \tag{4.63}$$

In this example there are few independent parameters. Masses of the three right-handed neutrinos $M_{N_i}$, mass of the extra gauge boson $Z_{\rm BL}$, mass of the extra Higgs $M_H$, scalar mixing angle $\theta$, extra gauge coupling $g_{\rm BL}$ and active-sterile mixing angle $\alpha$. The scalar mixing angle does not play important role and is kept $\theta = 0.1$ throughout the example.

Here we consider that DM is the lightest sterile neutrino $N_1$ generated non-thermally through freeze-in mechanism mainly via decays of [78].

$$W^\pm \to N_1 e^\pm \qquad \text{and} \qquad Z_{BL} \to N_1 \bar{N}_1, \tag{4.64}$$

where $W$ is the intermediate vector boson from SM and $Z_{BL}$ is the extra gauge boson of the model. The initial abundance of $N_1$ is negligible, thus $N_1 e^\pm \to W^\pm$

and $N_1\bar{N}_1 \to Z_{BL}$ are unlikely to happen. Although $N_1$ is mainly produced by decays of $W^\pm$ and $Z_{BL}$ all possible production channels of $N_1$ from SM and beyond SM have to be taken into account. The active-sterile mixing angle [81] is therefore nonzero and a normal active SM neutrino can change flavor to a sterile neutrino.

Decay rates for the two main decay channels are [78]

$$\begin{aligned}\Gamma(W^\pm \to N_1 e^\pm) = &\frac{2(2m_W^4 - (m_e^2 - m_{N_1}^2)^2 - (m_e^2 + m_{N_1}^2)m_W^2)\sin^2\alpha}{3v^2} \\ &\times \frac{1}{16\pi m_W}\sqrt{1 - \left(\frac{m_e + m_{N_1}}{m_W}\right)^2}\sqrt{1 - \left(\frac{m_e - m_{N_1}}{m_W}\right)^2}\end{aligned} \tag{4.65}$$

$$\Gamma(Z_{LB} \to N_1\bar{N}_1) = \frac{m_{Z_{BL}}}{24\pi}\Big[(\sin^2\alpha - \cos^2\alpha)^2 g_{BL}^2\Big]\Big[1 - \frac{4m_{N_1}^2}{m_{Z_{BL}}^2}\Big]^{3/2}. \tag{4.66}$$

Since the non-thermal DM interacts extremely weakly, it requires the coupling $g_{BL}$ to be small as well. Making $g_{BL}$ very small $g_{BL}$ ($< 10^{-9}$) [78] makes the contribution from decays of $W^\pm$ also significant production channel of $N_1$. Notably, if $g_{BL} \ll \alpha$ the only dominant production channel is from decays of $W^\pm$, as it depends only on the active-sterile mixing angle $\alpha$.

Due to the extremely weak interaction strength $g_{\rm BL}$, the extra gauge boson $Z_{BL}$, is not in thermal equilibrium in the early universe. In order to calculate the comoving number density $Y_{N_1}$, we need to form and solve the Boltzmann equation, which tells how the comoving number density $Y_{Z_{\rm BL}}$ evolves. The additional Higgs boson (H) and the extra gauge boson $Z_{\rm BL}$ gain their masses after the breaking of $\mathrm{U}(1)_{B-L}$ symmetry, therefore $Z_{BL}$ is mainly produced by equilibrium decays of $H$. The decay rate for $H$ is [78]

$$\Gamma(H \to Z_{\rm BL}Z_{\rm BL}) = \frac{g_{\rm BL}M_H^3\cos^2\theta}{8\pi M_{Z_{\rm BL}}}\sqrt{1 - \frac{4M_{Z_{\rm BL}}^2}{M_H^2}}\left(1 - \frac{4M_{Z_{\rm BL}}^2}{M_H^2} + \frac{12M_{Z_{\rm BL}}^4}{M_H^4}\right). \tag{4.67}$$

The Boltzmann equation is given by

$$\frac{dY_{Z_{BL}}}{dz} = \frac{2M_{\rm P}}{0.33M_h^2}\frac{z\sqrt{g_*(z)}}{g_{*s}(z)}\Big(\big\langle\Gamma_{H\to Z_{BL}Z_{BL}}\big\rangle Y_H^{\rm eq} - \big\langle\Gamma_{Z_{BL}\to \rm all}\big\rangle Y_{Z_{BL}}\Big), \tag{4.68}$$

where $z = M_h/T$, where $M_h$ is the mass of the SM Higgs. $g_*(z)$ is given by

$$\sqrt{g_*(z)} = \frac{g_{*s}(z)}{\sqrt{g_{*\rho}(z)}}\Big(1 - \frac{1}{3}\frac{d\ln g_{*s}(z)}{d\ln z}\Big). \tag{4.69}$$

$\big\langle\Gamma_{\psi\to\phi\phi}\big\rangle$ is the thermally averaged decay rate, which is defined by [65]

$$\big\langle\Gamma_{\psi\to\phi\phi}\big\rangle = \frac{K_1(z)}{K_2(z)}\Gamma_{\psi\to\phi\phi}, \tag{4.70}$$

where $K_1$ and $K_2$ are the modified Bessel functions first and second kind respectively. In equation (4.68) the term $-\langle\Gamma_{H\to Z_{BL}Z_{BL}}\rangle Y_{Z_{\rm BL}} \approx 0$, since the initial abundance of $Z_{\rm BL}$ is very small, the inverse process $Z_{\rm BL}Z_{\rm BL} \to H$ can be neglected. $Z_{\rm BL}$ can also be produced by annihilation processes, such as $hh \to Z_{\rm BL}Z_{\rm BL}$ and $HH \to Z_{\rm BL}Z_{\rm BL}$, but contribution from scattering processes are sub-dominant as seen in section 4.4.

The Boltzmann equation for the lightest sterile neutrino $N_1$ is given by

$$\begin{aligned}\frac{dY_{N_1}}{dz} = &\frac{2M_{\rm P}}{0.33M_h^2}\frac{z\sqrt{g_*(z)}}{g_{*s}(z)}\Big[\langle\Gamma_{W^\pm\to e^\pm N_1}\rangle(Y_W^{\rm eq} - Y_{N_1}) \\ &+ \langle\Gamma_{Z_{BL}\to N_1N_1}\rangle(Y_{Z_{BL}} - Y_{N_1}) + \sum_i\langle\Gamma_{i\to N_1N_1}\rangle(Y_i^{\rm eq} - Y_{N_1})\Big] \\ &+\frac{4\pi^2}{45}\frac{M_{\rm P}M_h}{0.33}\frac{\sqrt{g_*(T)}}{z^2}\Big[\sum_j\langle\sigma v_{j\bar{j}\to N_1N_1}\rangle((Y_j^{\rm eq})^2 - Y_{N_1}^2) \\ &+ \langle\sigma v_{Z_{BL}Z_{BL}\to N_1N_1}\rangle(Y_{Z_{BL}}^2 - Y_{N_1}^2)\Big].\end{aligned} \tag{4.71}$$

Here $i$ and $j$ contains all the other possible decay and annihilation channels for $N_1$ production.

The Boltzmann equation (4.71) governs the evolution of the comoving number density of $N_1$. Numerical solution to the equations (4.68) and (4.71) is shown in Figure 14. The contributions from decays of $Z_{\rm BL}$ and $W^\pm$ can be seen as two plateaus. This effect is present in cases where $\alpha \sim g_{\rm BL}$. At the beginning there are no $Z_{\rm BL}$ or $N_1$ particles. The production of $N_1$ starts from decays of $W$ boson. As the number density of $W$ starts to fall the production of $N_1$ decreases, which is seen as the first plateau. The number of $N_1$ does not change until the production from decays of $Z_{\rm BL}$ starts. As the number of $Z_{\rm BL}$ becomes negligible the number of $N_1$ finally freezes-in to a constant, which is seen as the second plateau. In Figure 14c the "double plateau" effect is absent. This can be explained by the size of active-sterile mixing angle $\alpha$, which is the only parameter controlling $W^\pm \to e^\pm N_1$ decay. Since $\alpha \gg g_{\rm BL}$ the production of $N_1$ is dominated by decays of $W^\pm$ for all $z$, which result in a single plateau.

The density parameter of $N_1$ is given by [77]

$$\Omega_{N_1}h^2 = 2.755\times10^8\Big(\frac{M_{N_1}}{\rm GeV}\Big)Y_{N_1}(T_0). \tag{4.72}$$

Using the equation (4.72) the density of $N_1$ can be obtained by solving the comoving number density at $Y_{N_1}(T_0)$ from the Boltzmann equations (4.68) and (4.71). The numerical solution is shown in Figure 15. The parameters are chosen so that the decay channels $Z_{\rm BL} \to N_1\bar{N}_1$ and $W^\pm \to e^\pm N_1$ have equal contributions to the

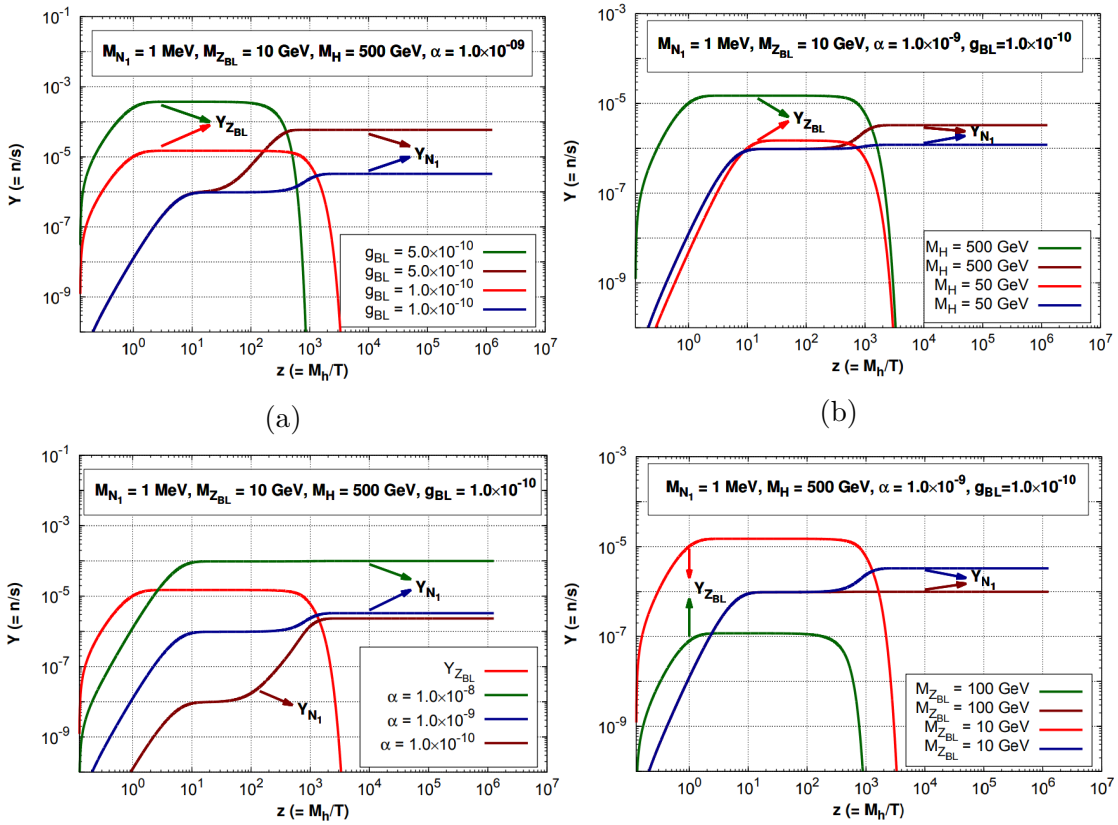


Figure 14: Evolution of the comoving number densities $Y_{Z_{\rm BL}}$ and $Y_{N_1}$ with different set of parameters $g_{\rm BL}$, $M_H$, $\alpha$ and $M_{Z_{\rm BL}}$. Figure taken from [78].

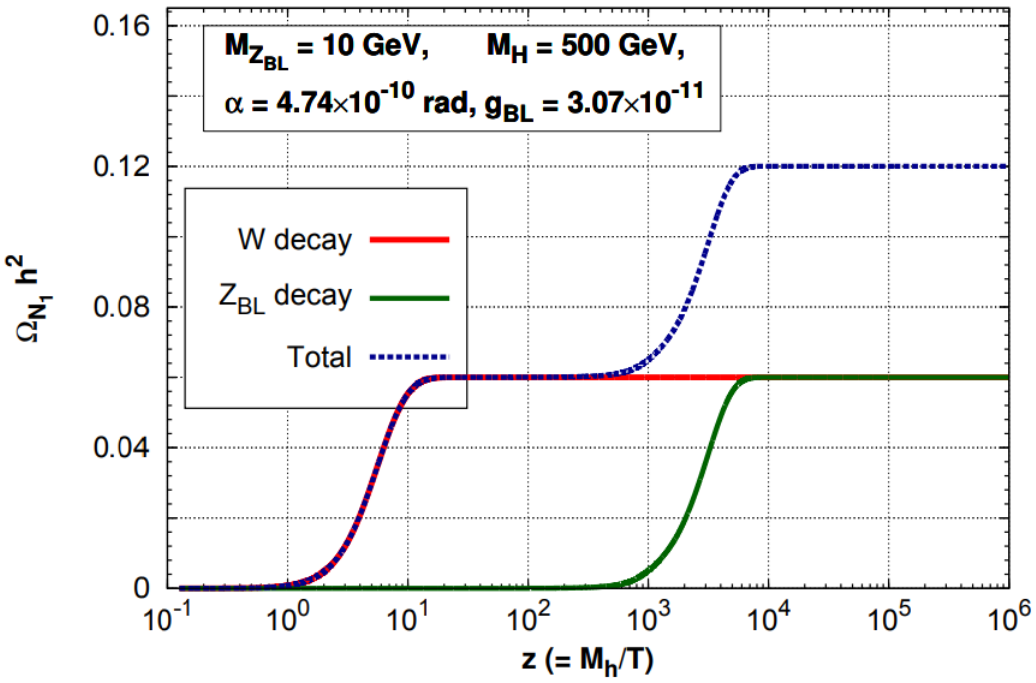


Figure 15: Density of sterile neutrino dark matter $N_1$ with equal contributions from decays of $W^{\pm}$ and $Z_{\rm BL}$. Figure is from [78].

$N_1$ density $\Omega_{N_1} h^2 = 0.12$, while keeping $M_{N_1} = 1$ MeV. Figure 15 illustrates more clearly how the production of $N_1$ starts with decays of $W^{\pm}$ and later increased by decays of $Z_{\rm BL}$. Both decay channels contribute equal amount, while other decay and annihilation channels contribute negligible amount for $M_{N_1} = 1$ MeV, $M_{Z_{\rm BL}} = 10$ GeV, $M_H = 500$ GeV, $\alpha = 4.74 \times 10^{-10}$ rad and $g_{\rm BL} = 3.07 \times 10^{-11}$[78].

Because the dark matter density is known to be $\Omega_c h^2 = 0.12$ [5]. All the possible parameters values of the model can be found that satisfy the observed DM density and that are not constrained by any cosmological and astrophysical observations and theories.

# 5 Experimental signals of dark matter

Although a lot of effort has been made to detect dark matter directly and indirectly, there still exists no clear signal of DM scattering with other particles and no confirmation of possible annihilation or decay products of DM. In this section we discuss the status of DM searches and prospects.

## 5.1 Direct detection

Observations of galaxy rotation curves indicate that galaxies are surrounded by dark matter halo [1]. Therefore, a flux of dark matter passes through the Earth as it orbits the Sun. Direct detection experiments aim to measure the recoil energy of nuclei which has collided with DM particle. An annual modulation of the number of detection events is expected to emerge from the recorded data due to the variation in the velocity of the detector relative to the dark matter halo.

The WIMP-nuclei differential scattering rate is given by [8]

$$\frac{dR}{dE}(E,t) = \frac{N_T \rho_\chi}{m_\chi m_A} \int_{v_{\min}}^{v_{\text{esc}}} v f_E(\vec{v},t) \frac{d\sigma}{dE}(v,E) d^3\vec{v}, \tag{5.1}$$

where $N_T$ is the number of target nuclei per kilogram of the detector, $\rho_\chi$ is the local DM density, $m_\chi$ is the DM mass, $m_N$ is the nucleon mass, $\vec{v}$ is the velocity of the DM particle relative to the Earth, $f_E(\vec{v},t)$ is the distribution of velocities of the WIMP in the frame of the Earth. $v_{\min}$ is the minimum WIMP speed required to produce a detectable event at energy $E$, $v_{\text{esc}}$ is the minimum velocity required so that WIMPs in the halo are no longer bounded to the Milky Way. $\mu$ is the reduced mass of the WIMP-nucleus. The differential cross section for the WIMP-nucleus scattering is given by

$$\frac{d\sigma}{dE} = \frac{m_N}{2\mu^2 v^2}\Big[\sigma_{SI} F^2(q) + \sigma_{SD} S(q)\Big], \tag{5.2}$$

where $F^2(q)$ and $S(q)$ are the spin-independent and spin-dependent form factors [62].

WIMP direct detection experiments such as DAMA/LIBRA [82], GoGent [83] and CDMS [84] have reported annual modulation in the event rate, but the results are inconsistent between each other and in conflict with null results from other experiments such as XENON [85], LUX [86] and PandaX-II [87]. More recent independent analysis of the GoGent data has shown that recorded excess events

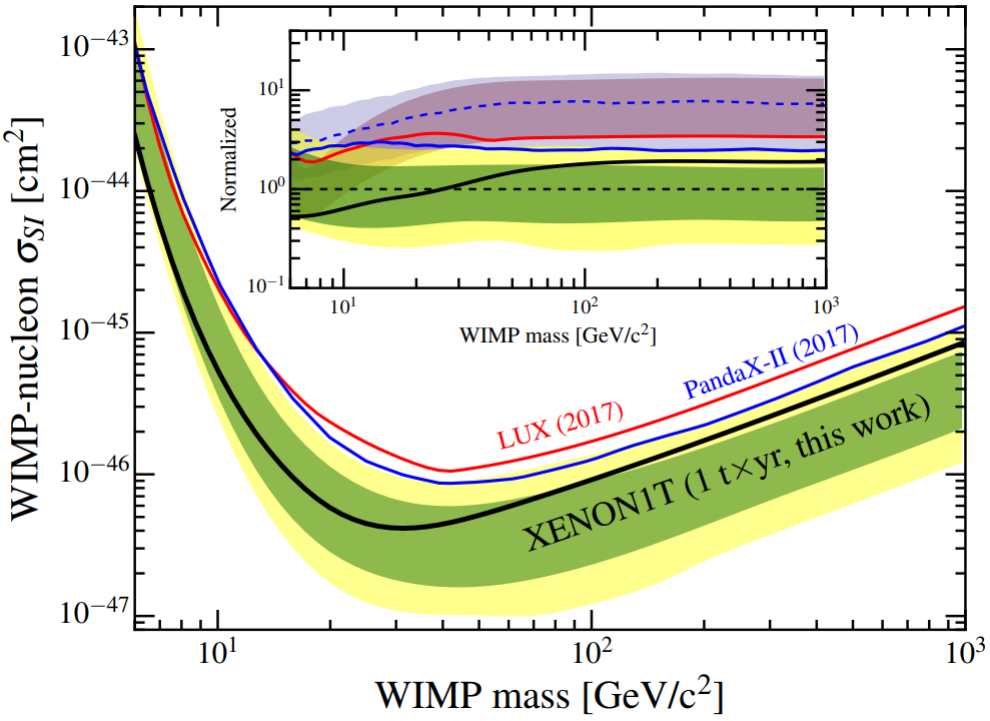


Figure 16: Upper limit for WIMP-nucleon spin-independent elastic scattering cross section $\sigma_{SI} = 4.1 \times 10^{-47}$ cm$^2$ at 30 GeV (black line) with $1\sigma$ (green) and $2\sigma$ (yellow) sensitivity bands from XENON1T experiment [85]. Red and blue lines represent results from previous LUX [86] and PandaX-II [87] experiments respectively. Normalized bands are shown in the inset.

were in fact caused by underestimated background from surface events [88]. In addition, the spin-independent WIMP-nucleon interaction was ruled out as the cause of the DAMA-signal by the COSINE-100 experiment [89]. Currently the best constraint for the spin-independent WIMP-nucleon scattering cross section and the WIMP mass has been set by XENON1T experiment [85]. Limits for the cross section and mass from recent direct detection experiments are illustrated in Figure 16, which further constrain the parameter space of existing WIMP models.

Null results from WIMP direct detection experiments encourages to explore other regions in the dark matter parameter space. For example, FIMP dark matter with a mass in the MeV range can produce detectable single-electron ionization signals from DM-electron scatterings [90]. Light DM with sub-GeV mass requires large number density in order to match the observed dark matter density, which on the other hand, enhances the DM-electron scattering detection rate. Other alternative signals from DM-electron scatterings are ultraviolet photons, individual

ions and heat [90]. Ongoing experimental setups dedicated to find WIMP signals, might be able to detect signals from FIMPs in the near future as sensitivity improves.

## 5.2 Indirect detection

Indirect detection experiments aim to observe the annihilation or decay products of dark matter at galactic and extragalactic scales. Flux of stable particles such as protons, antiprotons, electrons, positrons and photons over the expected background could be a potential DM signal [8]. Since photons are not affected by magnetic fields, they keep their spatial information and are thus ideal channel for detecting DM signal. In order to distinguish DM signal, all other astrophysical sources and phenomena have to be well understood in order to rule them out as a possible explanation to the observation. Natural places to find these signals are regions where dark matter concentration is high, such as near a supermassive black hole in the center of the Milky Way [91].

There have been several observation of excess gamma rays. For example, the EGRET gamma ray detector observed higher diffuse galactic flux than what was theoretically predicted [92]. Various explanations were presented to account for the "anomaly" including annihilation of WIMPs [93]. However, it was later concluded that the "anomaly" was likely due to an error in the EGRET sensitivity [94]. Another excess of gamma rays was observed by the Fermi-LAT coming from the center of the Milky Way [95]. Various explanations have been provided including the annihilation of WIMPs [95] and galactic millisecond pulsars [96]. However, DM annihilation interpretation is inconsistent with dwarf spheroidal galaxies [97] and more recent work suggest that only $\sim 1 - 5$ % of the observed excess gamma rays are produced by millisecond pulsars in the inner region of the galaxy [98].

In 2014 the IceCube Neutrino Observatory announced they had detected 37 extraterrestrial high-energy neutrinos over three-year period with energies ranging from 30 to 2000 TeV [99]. The origin of the observed neutrinos is unknown and various astrophysical sources have been put forth to account for the observation [100], [101]. The IceCube signal has also been examined in context of frozen-in heavy neutrino DM as a possible explanation [102], [103]. If the observed neutrinos are decay products of DM, it is more likely that the unstable DM is produced via freeze-in mechanism, since the extremely weak couplings characteristic for freeze-in can result in a very long lifetimes [102].

Unidentified emission line at $E \simeq 3.55$ keV has been found in a stacked analysis from X-ray images of 73 different galaxy clusters and in the X-ray spectra of Andromeda galaxy taken by XMM-Newton telescope [104], [105]. The excess might have connection to decays of sterile neutrino [106]. However, the 3.55 keV line is absent in spectra of several galaxy clusters obtained by Suzaku [107]. The

excess might also originate from some atomic transition for example Potassium [108], but currently there is no evidence to exclude the DM interpretation.

## 5.3 Collider searches

Dark matter is actively searched at colliders and are mainly focused on WIMPs. One of the main goals of Large Hadron Collider (LHC) was to find evidences of supersymmetry and signals of electroweak scale WIMPs through proton-proton collisions [109]. Since WIMPs are stable and neutral particles, a potential WIMP signal could be detected as missing energy.

Mono-X searches refers to WIMP production associated with jets or with other SM particles [110]–[113]. Jets with large transverse momentum within an event with large missing transverse momentum might be a potential DM signal [8]. If WIMP mass is half of the mass of $Z$ or Higgs boson they might invisibly decay into WIMPs. Since the decay width of the Z boson has been precisely measured, it sets strict constraints on the WIMP models with current limit $\Gamma(Z \to \text{ inv}) \leq (499 \pm 1.5)$ MeV [114]. In case of Higgs, bounds from LHC can be used to estimate the invisible branching ratio to be $\text{Br}(h \to \text{inv}) \leq 0.25$ at 95 % confidence level[115].

It was widely believed that new physics would emerge around TeV scale, since supersymmetry is an attractive solution to the hierarchy problem [66], and it could also provide a DM candidate [109]. However, experiments at LHC show no new physics beyond SM and no signals of DM up to $\sqrt{s} = 13$ TeV [109].

Dark matter produced by freeze-in mechanism is typically unobservable at colliders due to the small production cross section. However, freeze-in models where DM is coupled to SM via a mediator particle could result in detectable signatures in colliders, since the mediator particle itself might not be weakly coupled to the visible sector [116].

## 5.4 Influence of dark matter

Recently the Experiment to Detect the Global Epoch of Reionization Signature (EDGES) collaboration announced a discovery of 21-cm signal originated from the very first stars that formed in the Universe from the primordial hydrogen gas [117]. The observed signal suggests that in the early universe dark matter interacted with baryons [118].

Before the formation of the first stars after the Universe became matter dominated is referred as the Dark Age. Eventually dense regions of primordial hydrogen gas collapsed to to form stars referred as the Cosmic Dawn. At that time the Universe consisted mostly of hydrogen, CMB photons and dark matter.

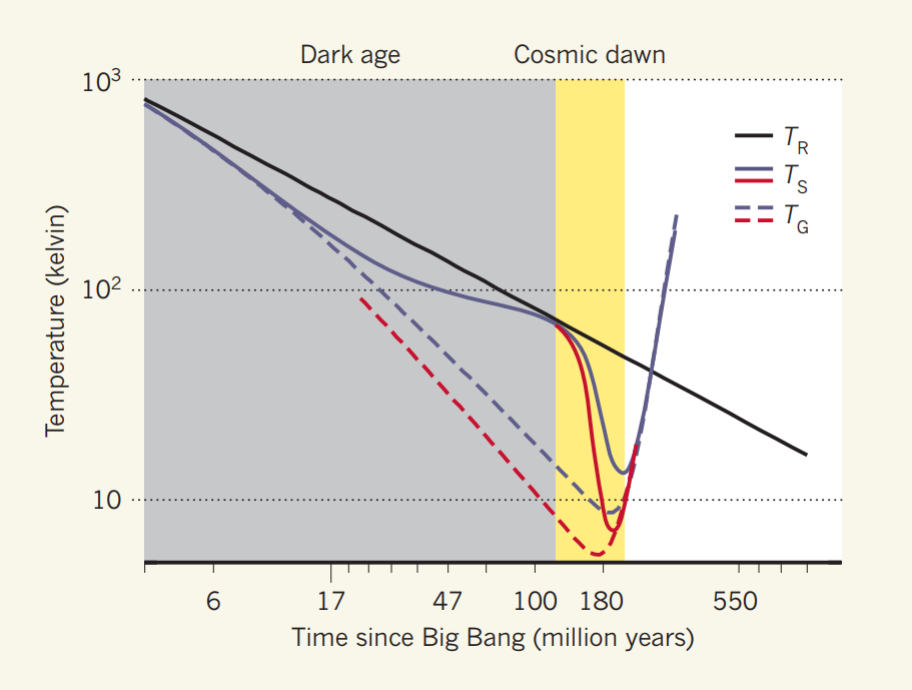


Figure 17: Evolution of the radiation temperature $T_{\mathrm{R}}$, the spin temperature $T_{\mathrm{S}}$ and the hydrogen gas temperature $T_{\mathrm{G}}$. Solid and dashed line corresponds to the predictions based on cosmological models and observations by EDGES respectively. Figure taken from [120]

Neutral hydrogen atom consists of one positively charged proton and one negatively charged electron. The proton and electron can have parallel spins, or antiparallel spins. When the hydrogen is in spin parallel state, it is in a slightly higher energy state. The transition between these states is called the spin flip transition [119]. As this transition occurs a very low-energy photon is emitted or absorbed which has an energy of $5.9 \times 10^{-6}$ eV and wavelength of 21 cm. This is equal to 1.4 GHz which falls to the radio frequency in the electromagnetic spectrum. This transition is also called the hydrogen line or the 21-centimeter line.

The 21-cm signal originating from the age of Cosmic Dawn reported by EDGES can be expressed as temperature relative to the CMB temperature [118]

$$T_{21} = 26.8 X_{\mathrm{HI}} \left(\frac{\rho_g}{\bar{\rho_g}}\right) \left(\frac{\Omega_{\mathrm{b}} H}{0.0327}\right) \left(\frac{0.307}{\Omega_{\mathrm{m}}}\right)^{1/2} \left(\frac{1+z}{10}\right)^{1/2} \left(\frac{T_{\mathrm{S}} - T_{\mathrm{R}}}{T_{\mathrm{S}}}\right) \mathrm{mK}, \qquad (5.3)$$

where $\rho_g$ is density of hydrogen gas and $\bar{\rho_g}$ is its cosmic mean value. $\Omega_{\mathrm{b}}$ and $\Omega_{\mathrm{m}}$ are the density parameters of baryons and matter respectively. $H$ is the Hubble parameter in units of 100 km/s/Mpc, $z$ is the redshift corresponding the observed

wavelength and frequency. $T_{\mathrm{R}}$ is the temperature of the CMB or the radiation at $z$. $T_{\mathrm{S}}$ is the spin temperature at $z$, which satisfies [121]

$$\frac{n_1}{n_0} = 3e^{-T_*/T_{\mathrm{S}}}. \tag{5.4}$$

The above equation relates the ratio between the occupation number of the higher energy state, spin parallel state $n_1$ and the lower energy state, spin antiparallel state $n_0$ to the spin temperature $T_{\mathrm{S}}$. Here $T_* = 0.0681$ K is the temperature corresponding to the 21-cm wavelength. The $X_{\mathrm{HI}}$ is the mass fraction of hydrogen defined as [10]

$$X_{HI} \equiv \frac{An}{n_{\mathrm{B}}}, \tag{5.5}$$

where $A$ is the mass number and $n$ is the number density of hydrogen. $n_{\mathrm{B}}$ is the number density of baryons.

In the early universe during the Dark Age before the Cosmic Dawn the spin temperature $T_{\mathrm{S}}$ was initially coupled with the temperature of the hydrogen gas $T_{\mathrm{G}}$ illustrated in Figure 17. As the Universe expanded the gas cooled and was no longer able to maintain the coupling and the spin temperature coupled with the CMB temperature $T_{\mathrm{R}}$. The hydrogen gas cooled and collapsed to form the very first stars. Lyman-$\alpha$ photons from the early stars shifted the equilibrium and the over time the spin temperature recoupled with the temperature of the hydrogen gas via the Wouthuysen-Field effect [122]. Since the emitted Lyman-$\alpha$ photons with energy 10.2 eV, corresponding to the transition between energy states $n = 1$ and $n = 2$ in hydrogen atom, is $\sim 10^7$ times larger than the photon emitted by the spin flip transition, there is an equal change of hydrogen ending up in spin parallel or spin antiparallel state. Therefore, the equation (5.4) is driven towards $n_1/n_0 \simeq 1$ from $n_1/n_0 \simeq 3$ as the hydrogen gas cools and more 21-centimeter photons are absorbed than emitted.

Eventually the presence of stars stops the cooling of the hydrogen gas and starts heating it. As the early stars die they leave behind black holes and neutron stars. X-rays from the stellar remnants further heat the gas and the gas is expected to become hotter than CMB temperature [117]. At that point the gas is too hot to absorb or emit 21-centimeter photons. When examined the brightness temperature equation (5.3) as a function of $z$, we should see decrease in the temperature $T_{21}$ when $T_{\mathrm{S}}$ recouples with $T_{\mathrm{G}}$ in the presence of stars, and increase when stellar remnants began further heating the hydrogen gas. This is the absorption profile that EDGES reported shown in Figure 18.

The observed absorption profile is centered at $z \approx 17$ and spans $20 > z > 15$. The absorption peak correspond to frequency $\nu = 78 \pm 1$ MHz with brightness temperature $T_{12} = -0.5^{+0.2}_{-0.5}$ K [117]. The observed absorption line was expected [123], but the strongest possible absorption was predicted to be -0.209 K [118]. In

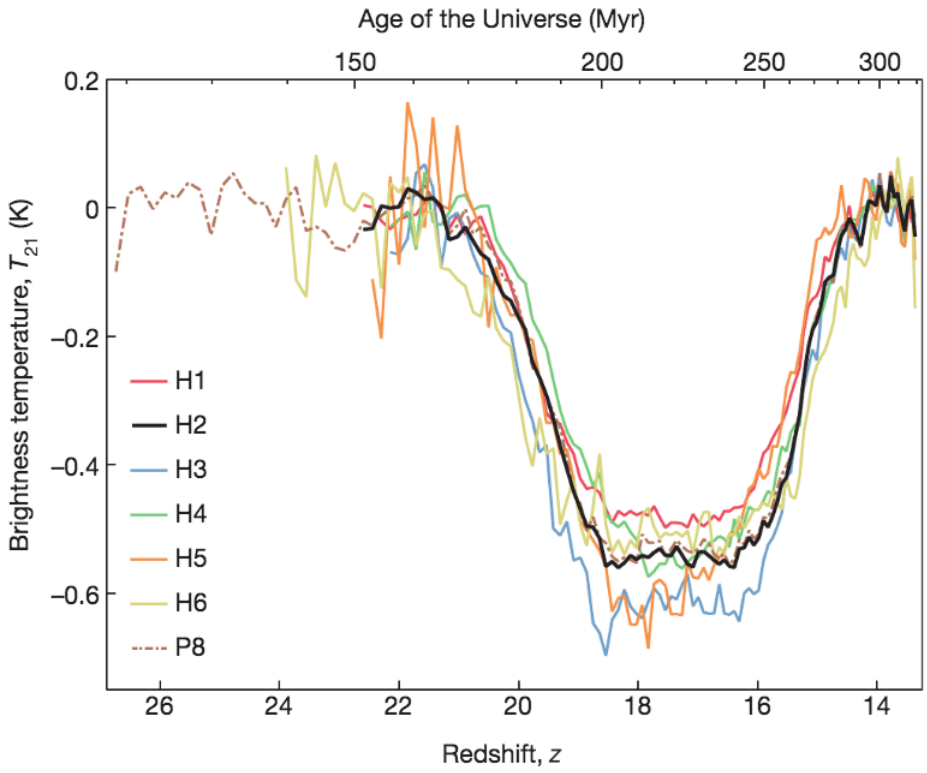


Figure 18: Absorption profile of hydrogen line detected with seven different detectors by EDGES. Figure taken from [117]

addition, the observed absorption profile is flat instead of Gaussian.

The lower peak than expected in the absorption profile suggest that the hydrogen gas has interacted with dark matter [117], [118]. Especially cold dark matter, which decouples from the thermal bath while non-relativistic well before photon decoupling. CDM could interact with the hydrogen gas and making it colder corresponding to the observation. Combining the radiation from the first stars with baryon-DM scattering, sets constraints on dark matter models. Based on the absorption profile observed by EDGES and assuming a minimum absorption of $-0.3$ K, dark matter with mass $m_\chi < 4.3$ GeV and cross section $\sigma_1 > 3.4 \times 10^{-21}\text{cm}^2$ can produce the observed 21-cm signal [118]. DM with mass around few GeV is consistent with null results from direct detection experiments, which aim to detect WIMPs with much larger mass. The dark matter interpretation requires extensive testing of the observed signal. Experiments such as SARAS [124], SCI-HI [125] and LEDA [126] will attempt to replicate and confirm the observed 21-cm signal.

## 5.5 Primordial black holes as DM

It is possible that primordial black holes (PBH) [127] could have formed in the early universe with wide range of masses from collapsed high density regions [128]. However, black holes with mass less than about $10^{15}$ g [127], corresponding to about $10^{-18} M_\odot$, would have evaporated via Hawking radiation [129]. PBHs with masses larger than $10^{-18} M_\odot$ remain in the Universe and could contribute to the dark matter abundance. By observing the stochastic gravitational wave background produced by primordial density perturbations [130], which also seeds the primordial black holes, might reveal the existence of PBHs and if they contribute to the density of dark matter.

Gravitational waves (GW) [11] are disturbances in the fabric of space-time generated by accelerated masses. These "ripples" propagate at the speed of light through the Universe outward in every direction from the source, much like waves produced by water droplet falling into a pond.

The first directly detected gravitational wave was observed by Advanced LIGO and Advanced Virgo detectors in 2015 (GW150914) [131]. It was generated by pair of merging black holes with masses $36 M_\odot$ and $29 M_\odot$. The event occurred at a luminosity distance 410 Mpc. The estimated total energy released via gravitational radiation is $3 M_\odot$.

Same instruments were used to observe another gravitational wave event (GW170817) [132] in 2017, which originated from binary neutron star merger. The total mass of the system is $2.74 M_\odot$ and is located at luminosity distance 40 Mpc. The same binary neutron star merger was also observed independently $\sim 1.7$ s after the GW signal by Fermi Gamma-ray Burst Monitor via short gamma-ray burst (GRB 170817A) [133]. Large-scale observing campaign was launched across electromagnetic spectrum, which lead to the localization of the GRB 170817A in NGC 4993, only 11 hours after the GW signal.

In order to detect gravitational waves with our current technology, a very high energetic event, such as colliding black holes, supernova or a rotation of neutron stars is needed. In order to enhance the rate of GW detection, new and better instruments are underway. One of those projects is called Laser Interferometer Space Antenna (LISA) [134], which is space-based gravitational wave detector. It consists of three individual spacecrafts arranged in an equilateral triangle shape with $2.5 \times 10^9$ m between the satellites. Passing gravitational waves are detected by monitoring the distances between the spacecrafts. The extremely long sides and location enable LISA to detect gravitational waves with frequencies in the range $10^{-4}$ Hz to $10^{-1}$ Hz [134]. This frequency region allows LISA to detect GW with much lower energy than the ground-based detectors such as LIGO and Virgo, which operate in the frequency range 10 Hz to $10^3$ Hz [135]. Various sensitivity curves of detectors and sources are illustrated in Figure 19.

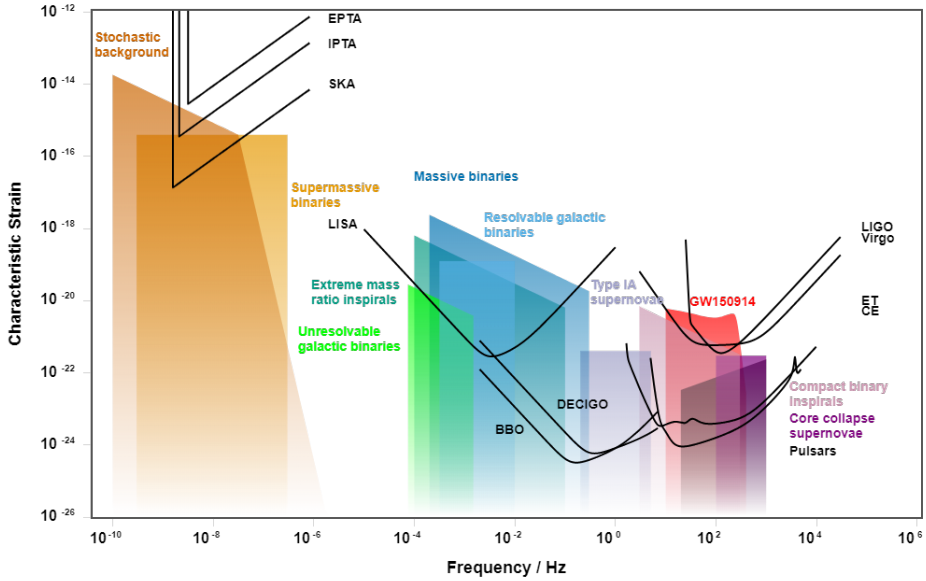


Figure 19: Sensitivity curves for various detectors and sources. Detectors can detect GW signals if the characteristic strain is above the sensitivity curve. Figure generated via [135].

Since primordial black holes are not formed from collapsing stars, their masses can be significantly smaller or larger than typical stellar mass black hole and they could contribute to the dark matter abundance. Idea that significant amount or all dark matter could consist of PBHs is not new, but many observational constraints [136] rule out large range of PBH dark matter masses. However, the sensitivity of LISA could enable the detection of gravitational waves generated at the time of PBH formation.

PBHs can be generated in numerous ways, but the standard method is enhancing the power spectrum of the comoving curvature perturbations during inflation [137]. The enhancing scale is constraint by the CMB anisotropies. Perturbations are eventually transferred to the radiation and if the perturbations are large enough the over dense regions collapse into PBHs at horizon re-entry [137]. Large gradients in curvature perturbations on small scales inevitably lead to primordial GWs [138].

The fraction of DM as PBHs can be written as [130]

$$f_{\mathrm{PBH}}(M) \approx \left(\frac{\beta_M}{6\times 10^{-9}}\right)\left(\frac{\gamma}{0.2}\right)^{1/2}\left(\frac{106.75}{g_{*\rho}}\right)^{1/4}\left(\frac{M_\odot}{M}\right)^{1/2}, \tag{5.6}$$

where $M$ is the mass of the PBHs and $\beta_M$ is the mass fraction of PBHs. $\gamma$ and $g_{*\rho}$ corresponds to the PBH formation efficiency and the effective number of energy

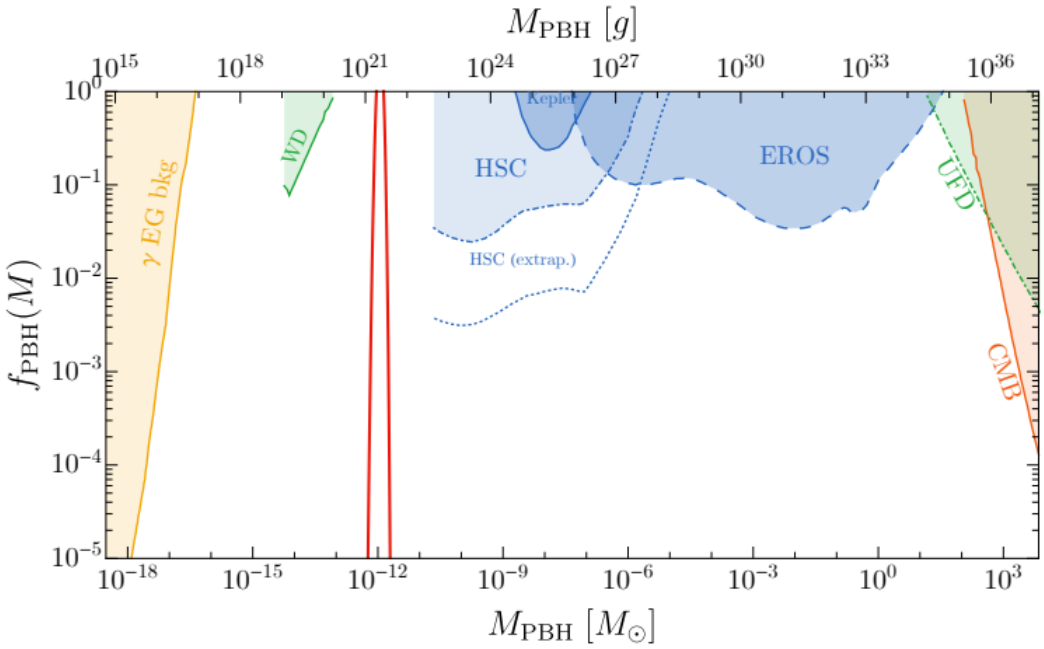


Figure 20: Present constraints on the mass fraction of PBH dark matter at various masses. Red lines represent the PBH abundance as DM. Figure is from [137].

degrees of freedom at horizon entry respectively. The mass of the PBHs is related to the peak frequency of the generated GWs [139]

$$M \approx 33\gamma M_\odot \left(\frac{10^{-9}\ \text{Hz}}{f}\right)^2. \tag{5.7}$$

Using the above equation and the maximum sensitivity of LISA, $f_{\rm LISA} \simeq 3.4$ mHz [137], corresponds to the PBH mass $M \simeq 10^{-12} M_\odot$ when $\gamma = 0.2$. Accidentally the observational constraints are absent around this mass as shown in Figure 20, where the red lines represent dark matter composed of PBHs. Controversial constraints from neutron-star capture [140] on PBHs masses $\sim 10^{18}$–$10^{24}$ g are not included, since they depend on assumptions about DM density in globular clusters [141]. This allows the possibility that DM is only composed of PBHs $f_{\rm PBH}(M) \simeq 1$ [137].

The detection of gravitational waves has enabled a new way of observing the Universe. Further improvements to the existing GW detection systems and development of new space-based and ground-based GW detection systems, such as LISA [134], DECIGO [142], BBO [143], Einstein Telescope [144] and Cosmic Explorer [145], might reveal something about the nature of dark matter in form of PBHs via gravitational waves.

# 6 Summary

The nature and origin of dark matter is still unknown. The presence of dark matter is verified through gravity and observed in several complementary settings: in behavior of galaxy rotation curves, in the evolution of cosmic structures, in the cosmic microwave background and in the mass distribution of galaxy clusters via weak gravitational lensing. All these observations are consistent with non-baryonic dark matter, which interacts only via gravitation with density $\Omega_c h^2 = 0.12$. Theory of Modified Newtonian Dynamics offers an explanation to these phenomena without dark matter, but it struggles to explain some observations without fully eliminating dark matter in some cases and it fails to deliver sufficient cosmological model.

In this thesis we discussed about Weakly Interacting Massive Particles or WIMPs as dark matter produced via thermal freeze-out mechanism, which is the dominating dark matter paradigm. We introduced the Boltzmann equation which describes how thermodynamic system evolves beyond equilibrium and calculated the comoving number density for WIMP $2 \to 2$ annihilation process. We also derived the analytical estimate for the final dark matter abundance and tested which parameters satisfy the dark matter density today.

After establishing the basics of the WIMP paradigm, we turned to introduce Feebly Interacting Massive Particles or FIMPs acting as dark matter produced alternatively via non-thermal freeze-in mechanism. Using the Boltzmann equation, we derived the comoving number density, final dark matter density and required couplings necessary to produce the observed dark matter density for FIMP produced via $1 \to 2$ decay and $2 \to 2$ scattering. Dark matter produced via decays of frozen-in FIMPs was also calculated, where the FIMP is unstable and decays to dark matter. The couplings required to produce FIMP dark matter via freeze-in mechanism are extremely small and contributions from $2 \to 2$ scatterings are sub-dominant. For both production mechanisms, freeze-out and freeze-in, the final dark matter density can be calculated given the couplings and masses of the particles in thermal bath and in dark sector. As an example, we went through how the freeze-in mechanism was applied to very specific sterile neutrino dark matter model in order understand why new physics beyond Standard Model is needed and how freeze-in mechanism constrain the dark matter parameter space.

In the previous section we discussed about the status of direct, indirect and collider experiments, which aim to detect various signals produced from dark matter collisions with baryons and dark matter annihilations or decays. In order to

distinguish a possible dark matter signal various astrophysical sources producing similar signals have to be well understood and excluded. Various signals such as excess gamma-rays, X-rays and high-energy neutrinos of unknown origin have been detected that might be related to dark matter annihilation or decay processes. However, signals from astrophysical sources cannot be fully excluded. Although there exists no confirmed signal from dark matter, the null results help to further constrain the parameter space of various dark matter models. We continued with possible detection of interaction between dark matter and baryons in the early universe making the primordial hydrogen gas colder. Therefore, making the 21-cm cosmology a viable tool to probe dark matter. We finished off with considering that the primordial black holes, which have not evaporated and remain in the Universe, could contribute to dark matter density. Observing gravitational waves with future more sensitive space-based and ground-based detectors related to the formation of primordial black holes might reveal if they exist and do they contribute to the dark matter density today.

Although dark matter remains a mystery, we now have clear understanding why it must exist and how it is produced thermally or non-thermally via freeze-out and freeze-in mechanism respectively. We learned how we might be able to detect dark matter directly and indirectly or through collider searches and how null results from experiments further constrain dark matter models.

# References


[1] V. C. Rubin, N. Thonnard and W. K. Ford Jr., 'Rotational properties of 21 Sc galaxies with a large range of luminosities and radii, from NGC 4605 ($R = 4$ kpc) to UGC 2885 ($R = 122$ kpc)', *The Astrophysical Journal*, vol. 238, p. 471, 1980. DOI: 10.1086/158003.

[2] D. Clowe *et al.*, 'A direct empirical proof of the existence of dark matter', *The Astrophysical Journal*, vol. 648, pp. L109–L113, 2006. arXiv: astro-ph/0608407.

[3] W. Hu and S. Dodelson, 'Cosmic microwave background anisotropies', *Annual Review of Astronomy and Astrophysics*, vol. 40, pp. 171–216, 2002. arXiv: astro-ph/0110414.

[4] S. S. McGaugh, 'A tale of two paradigms: the mutual incommensurability of ΛCDM and MOND', *Canadian Journal of Physics*, vol. 93, no. 2, pp. 250–259, 2015. arXiv: 1404.7525.

[5] N. Aghanim *et al.*, 'Planck 2018 results. VI. cosmological parameters', 2018. arXiv: 1807.06209.

[6] F. Zwicky, 'Die Rotverschiebung von extragalaktischen Nebeln', *Helvetica Physica Acta*, vol. 6, pp. 110–127, 1933, English and Spanish Translation of Zwicky's (1933) The Redshift of Extragalactic Nebulae. arXiv: 1711.01693.

[7] F. Zwicky, 'On the Masses of Nebulae and of Clusters of Nebulae', *The Astrophysical Journal*, vol. 86, p. 217, 1937. DOI: 10.1086/143864.

[8] G. Arcadi *et al.*, 'The waning of the WIMP? A review of models, searches, and constraints', *European Physical Journal*, vol. C78, no. 3, p. 203, 2018. arXiv: 1703.07364.

[9] L. J. Hall *et al.*, 'Freeze-in production of FIMP dark matter', *Journal of High Energy Physics*, vol. 03, p. 080, 2010. arXiv: 0911.1120.

[10] E. W. Kolb and M. S. Turner, *The Early Universe*. Westview Press, 1994.

[11] S. M. Carroll, *Spacetime and geometry: An introduction to general relativity*. Addison-Wesley, 2004.

[12] V. C. Rubin and W. K. Ford Jr., 'Rotation of the Andromeda nebula from a spectroscopic survey of emission regions', *The Astrophysical Journal*, vol. 159, p. 379, 1970. DOI: 10.1086/150317.

[13] M. S. Roberts and R. N. Whitehurst, 'The rotation curve and geometry of M31 at large galactocentric distances.', *The Astrophysical Journal*, vol. 201, pp. 327–346, 1975. DOI: 10.1086/153889.

[14] H. W. Babcock, 'The rotation of the Andromeda nebula', *Lick Observatory Bulletin*, vol. 19, pp. 41–51, 1939. DOI: 10.5479/ADS/bib/1939LicOB.19.41B.

[15] C. Carignan *et al.*, 'Extended HI rotation curve and mass distribution of M31', *The Astrophysical Journal*, vol. 641, pp. L109–L112, 2006. arXiv: astro-ph/0603143.

[16] K. C. Freeman, 'On the disks of spiral and S0 galaxies', *The Astrophysical Journal*, vol. 160, p. 811, 1970. DOI: 10.1086/150474.

[17] G. Bertone and D. Hooper, 'History of dark matter', *Reviews of Modern Physics*, vol. 90, no. 4, 2018. arXiv: 1605.04909.

[18] J. F. Navarro, C. S. Frenk and S. D. M. White, 'The structure of cold dark matter halos', *The Astrophysical Journal.*, vol. 462, pp. 563–575, 1996. arXiv: astro-ph/9508025.

[19] T. Linden, 'Dark matter in the Galactic center', *Proceedings of the International Astronomical Union*, vol. 9, no. S303, pp. 403–413, 2013. DOI: 10.1017/S1743921314001021.

[20] F. W. Dyson, A. S. Eddington and C. Davidson, 'A determination of the deflection of light by the Sun's gravitational field, from observations made at the total eclipse of May 29, 1919', *Philosophical Transactions of the Royal Society of London Series A*, vol. 220, pp. 291–333, 1920. DOI: 10.1098/rsta.1920.0009.

[21] M. Bartelmann, 'Gravitational lensing', *Classical and Quantum Gravity*, vol. 27, 2010. arXiv: 1010.3829.

[22] D. Walsh, R. F. Carswell and R. J. Weymann, '0957 + 561 A, B: twin quasistellar objects or gravitational lens?', *Nature*, vol. 279, pp. 381–384, 1979. DOI: 10.1038/279381a0.

[23] G. M. Bernstein, J. A. Tyson and C. S. Kochanek, 'A large arc in the gravitational lens system 0957 + 561', *The Astronomical Journal*, vol. 105, pp. 816–830, 1993. DOI: 10.1086/116474.

[24] R. Kormann, P. Schneider and M. Bartelmann, 'Isothermal elliptical gravitational lens models', *Astronomy and Astrophysics*, vol. 284, pp. 285–299, 1994. Available at: http://adsabs.harvard.edu/abs/1994A&A...284..285K.

[25] G. Golse and J.-P. Kneib, 'Pseudo elliptical lensing mass model: application to the NFW mass distribution', *Astronomy and Astrophysics*, vol. 390, pp. 821–827, 2002. arXiv: astro-ph/0112138.

[26] R. Gavazzi *et al.*, 'The sloan lens ACS survey. IV: the mass density profile of early-type galaxies out to 100 effective radii', *The Astrophysical Journal*, vol. 667, pp. 176–190, 2007. arXiv: astro-ph/0701589.

[27] G. A. Luppino and N. Kaiser, 'Detection of weak lensing by a cluster of galaxies at z = 0.83', *The Astrophysical Journal*, vol. 475, p. 20, 1997. arXiv: astro-ph/9601194.

[28] N. Kaiser, G. Squires and T. J. Broadhurst, 'A method for weak lensing observations', *The Astrophysical Journal*, vol. 449, pp. 460–475, 1995. arXiv: astro-ph/9411005.

[29] M. Bartelmann and M. Maturi, 'Weak gravitational lensing', 2016. arXiv: 1612.06535.

[30] M. Markevitch, 'Chandra observation of the most interesting cluster in the universe', 2005. arXiv: astro-ph/0511345.

[31] C. M. Hirata *et al.*, 'Intrinsic galaxy alignments from the 2SLAQ and SDSS surveys: luminosity and redshift scalings and implications for weak lensing surveys', *Monthly Notices of the Royal Astronomical Society*, vol. 381, pp. 1197–1218, 2007. arXiv: astro-ph/0701671.

[32] T. G. Brainerd, R. D. Blandford and I. Smail, 'Measuring galaxy masses using galaxy-galaxy gravitational lensing', *The Astrophysical Journal*, vol. 466, p. 623, 1996. arXiv: astro-ph/9503073.

[33] T. M. C. Abbott *et al.*, 'Dark Energy Survey year 1 results: cosmological constraints from galaxy clustering and weak lensing', *Physical Review*, vol. D98, no. 4, 2018. arXiv: 1708.01530.

[34] D. J. Bacon *et al.*, 'Joint cosmic shear measurements with the Keck and William Herschel Telescopes', *Monthly Notices of the Royal Astronomical Society*, vol. 344, pp. 673–685, 2003. DOI: 10.1046/j.1365-8711.2003.06877.x.

[35] T. Hamana *et al.*, 'Cosmic shear statistics in the Suprime-Cam 2.1 sq deg field: constraints on $\Omega_m$ and $\sigma_8$', *The Astrophysical Journal*, vol. 597, pp. 98–110, 2003. arXiv: astro-ph/0210450.

[36] T. Abbott *et al.*, 'The Dark Energy Survey: more than dark energy – an overview', *Monthly Notices of the Royal Astronomical Society*, vol. 460, no. 2, pp. 1270–1299, 2016. arXiv: 1601.00329.

[37] A. G. Riess *et al.*, 'Observational evidence from supernovae for an accelerating universe and a cosmological constant', *The Astronomical Journal*, vol. 116, pp. 1009–1038, 1998. arXiv: astro-ph/9805201.

[38] A. A. Penzias and R. W. Wilson, 'A measurement of excess antenna temperature at 4080 Mc/s.', *The Astrophysical Journal*, vol. 142, pp. 419–421, 1965. DOI: 10.1086/148307.

[39] ESA and the Planck Collaboration, *Planck CMB*, 2013. Available at: http://www.esa.int/spaceinimages/Images/2013/03/Planck_CMB (Accessed: 13th Feb. 2019).

[40] D. J. Fixsen, 'The temperature of the Cosmic Microwave Background', *The Astrophysical Journal*, vol. 707, no. 2, pp. 916–920, 2009. DOI: 10.1088/0004-637x/707/2/916.

[41] G. F. Smoot *et al.*, 'Structure in the COBE differential microwave radiometer first-year maps', *The Astrophysical Journal*, vol. 396, pp. L1–L5, 1992. DOI: 10.1086/186504.

[42] C. L. Bennett *et al.*, 'Nine-year Wilkinson Microwave Anisotropy Probe (WMAP) observations: final maps and results', vol. 208, no. 2, p. 20, 2013. DOI: 10.1088/0067-0049/208/2/20.

[43] R. B. Barreiro, 'The Cosmic Microwave Background: state of the art', *New Astronomy Review*, vol. 44, pp. 179–204, 2000. arXiv: astro-ph/9907094.

[44] ESA and the Planck Collaboration, *Planck's power spectrum of temperature fluctuations in the cosmic microwave background*, 2013. Available at: http://sci.esa.int/planck/51555-planck-power-spectrum-of-temperature-fluctuations-in-the-cosmic-microwave-background/ (Accessed: 13th Feb. 2019).

[45] U. Seljak and M. Zaldarriaga, 'A line of sight integration approach to Cosmic Microwave Background anisotropies', *The Astrophysical Journal*, vol. 469, pp. 437–444, 1996. arXiv: astro-ph/9603033.

[46] W. Hu *et al.*, 'A complete treatment of CMB anisotropies in a FRW universe', *Physical Review*, vol. D57, pp. 3290–3301, 1998. arXiv: astro-ph/9709066.

[47] D. Scott, M. Srednicki and M. J. White, ''Sample variance' in small scale CMB anisotropy experiments', *The Astrophysical Journal*, vol. 421, 1994. arXiv: astro-ph/9305030.

[48] A. Del Popolo, 'Dark matter and structure formation a review', *Astronomy Reports*, vol. 51, pp. 169–196, 2007. arXiv: 0801.1091.

[49] C.-P. Ma and E. Bertschinger, 'Cosmological perturbation theory in the synchronous and conformal Newtonian gauges', *The Astrophysical Journal*, vol. 455, pp. 7–25, 1995. arXiv: astro-ph/9506072.

[50] E. Lifshitz, 'Republication of: On the gravitational stability of the expanding universe', *Journal of Physics (USSR)*, vol. 10, p. 116, 1946. DOI: 10.1007/s10714-016-2165-8.

[51] A. Lewis and C. Anthony, 'Code for Anisotropies in the Microwave Background', Available at: https://camb.info/ (Accessed: 13th Feb. 2019).

[52] C. Alcock *et al.*, 'The MACHO project: microlensing results from 5.7 years of LMC observations', *The Astrophysical Journal*, vol. 542, pp. 281–307, 2000. arXiv: astro-ph/0001272.

[53] P. Tisserand *et al.*, 'Limits on the MACHO content of the galactic halo from the EROS-2 survey of the Magellanic Clouds', *Astronomy and Astrophysics*, vol. 469, pp. 387–404, 2007. arXiv: astro-ph/0607207.

[54] A. Schneider, R. E. Smith and D. Reed, 'Halo mass function and the free streaming scale', *Monthly Notices of the Royal Astronomical Society*, vol. 433, 2013. arXiv: 1303.0839.

[55] D. Boyanovsky, 'Free streaming in mixed dark matter', *Physical Review*, vol. D77, 2008. arXiv: 0711.0470.

[56] J. R. Bond, G. Efstathiou and J. Silk, 'Massive neutrinos and the large-scale structure of the universe', *Physical Review Letters*, vol. 45, pp. 1980–1984, 1980. DOI: 10.1103/PhysRevLett.45.1980.

[57] G. S. Bisnovatyi-Kogan and I. D. Novikov, 'Cosmology with a nonzero neutrino rest mass', *Soviet Astronomy*, vol. 24, 1980. Available at: http://adsabs.harvard.edu/abs/1980SvA....24..516B (Accessed: 18th Apr. 2019).

[58] J. R. Primack and M. A. K. Gross, 'Hot dark matter in cosmology', pp. 287–308, 2000. arXiv: astro-ph/0007165.

[59] V. Springel *et al.*, 'Simulating the joint evolution of quasars, galaxies and their large-scale distribution', *Nature*, vol. 435, pp. 629–636, 2005. arXiv: astro-ph/0504097.

[60] G. R. Blumenthal *et al.*, 'Formation of galaxies and large scale structure with cold dark matter', *Nature*, vol. 311, pp. 517–525, 1984. DOI: 10.1038/311517a0.

[61] J. S. Bullock *et al.*, 'Profiles of dark haloes. evolution, scatter, and environment', *Monthly Notices of the Royal Astronomical Society*, vol. 321, pp. 559–575, 2001. arXiv: astro-ph/9908159.

[62] G. Jungman, M. Kamionkowski and K. Griest, 'Supersymmetric dark matter', *Physics Reports*, vol. 267, pp. 195–373, 1996. arXiv: hep-ph/9506380.

[63] S. P. Martin, 'A supersymmetry primer', pp. 1–98, 1997. arXiv: hep-ph/9709356.

[64] M. Le Bellac, F. Mortessagne and G. G. Batrouni, *Equilibrium and Non-Equilibrium Statistical Thermodynamics*. Cambridge University Press, 2004. DOI: 10.1017/CBO9780511606571.

[65] P. Gondolo and G. Gelmini, 'Cosmic abundances of stable particles: improved analysis', *Nuclear Physics*, vol. B360, pp. 145–179, 1991. DOI: 10.1016/0550-3213(91)90438-4.

[66] M. E. Peskin and D. V. Schroeder, *An Introduction to Quantum Field Theory*. Avalon Publishing, 1995.

[67] J. H. Christenson *et al.*, 'Evidence for the $2\pi$ decay of the $K_2^0$ meson', *Physical Review Letters*, vol. 13, pp. 138–140, 1964. DOI: 10.1103/PhysRevLett.13.138.

[68] R. Aaij *et al.*, 'First observation of CP violation in the decays of $B_s^0$ mesons', *Physical Review Letters*, vol. 110, 2013. arXiv: 1304.6173.

[69] Q. Ahmad *et al.*, 'Measurement of the rate of $\nu_e + d \rightarrow p + p + e^-$ interactions produced by $^8B$ solar neutrinos at the Sudbury neutrino observatory', *Physical Review Letters*, vol. 87, 2001. arXiv: nucl-ex/0106015.

[70] S. Dodelson and L. M. Widrow, 'Sterile neutrinos as dark matter', *Physical Review Letters*, vol. 72, pp. 17–20, 1994. arXiv: hep-ph/9303287.

[71] R. Essig *et al.*, 'Constraining light dark matter with diffuse X-ray and gamma-ray observations', *Journal of High Energy Physics*, vol. 11, p. 193, 2013. arXiv: 1309.4091.

[72] A. Boyarsky *et al.*, 'Lyman-$\alpha$ constraints on warm and on warm-plus-cold dark matter models', *Journal of Cosmology and Astroparticle Physics*, vol. 0905, p. 012, 2009. arXiv: 0812.0010.

[73] U. Seljak *et al.*, 'Can sterile neutrinos be the dark matter?', *Physical Review Letters*, vol. 97, 2006. arXiv: astro-ph/0602430.

[74] A. Boyarsky *et al.*, 'Realistic sterile neutrino dark matter with keV mass does not contradict cosmological bounds', *Physical Review Letters*, vol. 102, 2009. arXiv: 0812.3256.

[75] B. Shakya, 'Sterile neutrino dark matter from freeze-in', *Modern Physics Letters*, vol. A31, 2016. arXiv: 1512.02751.

[76] H. Jutila, Research Training, University of Jyväskylä, 2017.

[77] J. Edsjo and P. Gondolo, 'Neutralino relic density including coannihilations', *Physical Review*, vol. D56, pp. 1879–1894, 1997. arXiv: hep-ph/9704361.

[78] B. Anirban and G. Aritra, 'Freeze-in production of sterile neutrino dark matter in $U(1)_{B\text{-}L}$ model', *Journal of Cosmology and Astroparticle*, vol. 1609, p. 044, 2016. arXiv: 1607.01469.

[79] R. N. Mohapatra and R. E. Marshak, 'Local B – L symmetry of electroweak interactions, Majorana neutrinos, and neutron oscillations', *Physical Review Letters*, vol. 44, pp. 1316–1319, 1980. DOI: 10.1103/PhysRevLett.44.1316.

[80] S. Khalil, 'Low scale B – L extension of the Standard Model at the LHC', *Journal of Physics*, vol. G35, 2008. arXiv: hep-ph/0611205.

[81] C. Giunti and M. Laveder, 'Neutrino mixing', 2003. arXiv: hep-ph/0310238.

[82] R. Bernabei *et al.*, 'Final model independent result of DAMA/LIBRA-phase1', *European Physical Journal*, vol. C73, 2013. arXiv: 1308.5109.

[83] C. E. Aalseth *et al.*, 'Results from a search for light-mass dark matter with a p-type point contact germanium detector', *Physical Review Letters*, vol. 106, 2011. arXiv: 1002.4703.

[84] R. Agnese *et al.*, 'Silicon detector dark matter results from the final exposure of CDMS II', *Physical Review Letters*, vol. 111, 2013. arXiv: 1304.4279.

[85] E. Aprile *et al.*, 'Dark matter search results from a one tonne×year exposure of XENON1T', *Physical Review Letters*, vol. 121, no. 11, 2018. arXiv: 1805.12562.

[86] D. S. Akerib *et al.*, 'Results from a search for dark matter in the complete LUX exposure', *Physical Review Letters*, vol. 118, 2017. arXiv: 1608.07648.

[87] X. Cui *et al.*, 'Dark matter results from 54-ton-day exposure of PandaX-II experiment', *Physical Review Letters*, vol. 119, no. 18, 2017. arXiv: 1708.06917.

[88] J. H. Davis, C. McCabe and C. Boehm, 'Quantifying the evidence for dark matter in CoGeNT data', *Journal of Cosmology and Astroparticle Physics*, vol. 1408, 2014. arXiv: 1405.0495.

[89] G. Adhikari, P. Adhikari and E. B. de Souza, 'An experiment to search for dark-matter interactions using sodium iodide detectors', *Nature*, vol. 564, pp. 83–86, 2018. DOI: 10.1038/s41586-018-0739-1.

[90] R. Essig, J. Mardon and T. Volansky, 'Direct detection of sub-GeV dark matter', *Physical Review*, vol. D85, 2012. arXiv: 1108.5383.

[91] G. Bertone, D. Hooper and J. Silk, 'Particle dark matter: evidence, candidates and constraints', *Physics Reports*, vol. 405, pp. 279–390, 2005. arXiv: hep-ph/0404175.

[92] S. D. Hunter *et al.*, 'EGRET observations of the diffuse gamma-ray emission from the galactic plane', *The Astrophysical Journal*, vol. 481, pp. 205–240, 1997. DOI: 10.1086/304012.

[93] W. de Boer *et al.*, 'EGRET excess of diffuse galactic gamma rays as tracer of dark matter', *Astronomy and Astrophysics*, vol. 444, p. 51, 2005. arXiv: astro-ph/0508617.

[94] F. W. Stecker, S. D. Hunter and D. A. Kniffen, 'The likely cause of the EGRET GeV anomaly and its implications', *Astroparticle Physics*, vol. 29, pp. 25–29, 2008. arXiv: 0705.4311.

[95] T. Daylan *et al.*, 'The characterization of the gamma-ray signal from the central Milky Way: A compelling case for annihilating dark matter', *Physics of the Dark Universe*, vol. 12, pp. 1–23, 2016. arXiv: 1402.6703.

[96] F. Calore, M. D. Mauro and F. Donato, 'Diffuse gamma-ray emission from galactic pulsars', *The Astrophysical Journal*, vol. 796, p. 1, 2014. arXiv: 1406.2706.

[97] A. Albert *et al.*, 'Searching for dark matter annihilation in recently discovered Milky Way satellites with Fermi-LAT', *The Astrophysical Journal*, vol. 834, p. 110, 2017. arXiv: 1611.03184.

[98] I. Cholis, D. Hooper and T. Linden, 'Challenges in explaining the galactic center gamma-ray excess with millisecond pulsars', *Journal of Cosmology and Astroparticle Physics*, vol. 1506, 2015. arXiv: 1407.5625.

[99] M. G. Aartsen *et al.*, 'Observation of high-energy astrophysical neutrinos in three years of IceCube data', *Physical Review Letters*, vol. 113, 2014. arXiv: 1405.5303.

[100] K. Murase, 'On the origin of high-energy cosmic neutrinos', *AIP Conference Proceedings*, vol. 1666, 2015. arXiv: 1410.3680.

[101] L. A. Anchordoqui *et al.*, 'Cosmic neutrino pevatrons: a brand new pathway to astronomy, astrophysics, and particle physics', *Journal of High Energy Astrophysics*, vol. 1-2, pp. 1–30, 2014. arXiv: 1312.6587.

[102] M. Chianese and A. Merle, 'A consistent theory of decaying dark matter connecting IceCube to the Sesame Street', *Journal of Cosmology and Astroparticle Physics*, vol. 1704, no. 04, p. 017, 2017. arXiv: 1607.05283.

[103] M. Re Fiorentin, V. Niro and N. Fornengo, 'A consistent model for leptogenesis, dark matter and the IceCube signal', *Journal of High Energy Physics*, vol. 11, 2016. arXiv: 1606.04445.

[104] E. Bulbul *et al.*, 'Detection of an unidentified emission line in the stacked X-ray spectrum of galaxy clusters', *The Astrophysical Journal*, vol. 789, p. 13, 2014. arXiv: 1402.2301.

[105] A. Boyarsky *et al.*, 'Unidentified line in X-ray spectra of the Andromeda galaxy and Perseus galaxy cluster', *Physical Review Letters*, vol. 113, 2014. arXiv: 1402.4119.

[106] H. Ishida, K. S. Jeong and F. Takahashi, '7 keV sterile neutrino dark matter from split flavor mechanism', *Physics Letters*, vol. B732, pp. 196–200, 2014. arXiv: 1402.5837.

[107] O. Urban *et al.*, 'A Suzaku search for dark matter emission lines in the X-ray brightest galaxy clusters', *Monthly Notices of the Royal Astronomical Society*, vol. 451, pp. 2447–2461, 2015. arXiv: 1411.0050.

[108] T. E. Jeltema and S. Profumo, 'Discovery of a 3.5 keV line in the Galactic Centre and a critical look at the origin of the line across astronomical targets', *Monthly Notices of the Royal Astronomical Society*, vol. 450, pp. 2143–2152, 2015. arXiv: 1408.1699.

[109] X. Cid Vidal *et al.*, 'Beyond the Standard Model physics at the HL-LHC and HE-LHC', 2018. arXiv: 1812.07831.

[110] V. Khachatryan *et al.*, 'Search for new phenomena in monophoton final states in proton-proton collisions at $\sqrt{s} = 8$ TeV', *Physics Letters*, vol. B755, pp. 102–124, 2016. arXiv: 1410.8812.

[111] G. Aad *et al.*, 'Search for dark matter in events with a hadronically decaying W or Z boson and missing transverse momentum in $pp$ collisions at $\sqrt{s} = 8$ TeV with the ATLAS detector', *Physical Review Letters*, vol. 112, 2014. arXiv: 1309.4017.

[112] I. M. Shoemaker and L. Vecchi, 'Unitarity and monojet bounds on models for DAMA, CoGeNT, and CRESST-II', *Physical Review*, vol. D86, 2012. arXiv: 1112.5457.

[113] A. Berlin, T. Lin and L.-T. Wang, 'Mono-Higgs detection of dark matter at the LHC', *Journal of High Energy Physics*, vol. 06, p. 078, 2014. arXiv: 1402.7074.

[114] C. Patrignani *et al.*, 'Review of particle physics', *Chinese Physics*, vol. C40, 2016. DOI: 10.1088/1674-1137/40/10/100001.

[115] G. Aad *et al.*, 'Constraints on new phenomena via Higgs boson couplings and invisible decays with the ATLAS detector', *Journal of High Energy Physics*, vol. 11, p. 206, 2015. arXiv: 1509.00672.

[116] S. Yaser Ayazi, S. M. Firouzabadi and S. P. Zakeri, 'Freeze-in production of fermionic dark matter with pseudo-scalar and phenomenological aspects', *Journal of Physics*, vol. G43, no. 9, 2016. arXiv: 1511.07736.

[117] J. D. Bowman *et al.*, 'An absorption profile centred at 78 megahertz in the sky-averaged spectrum', *Nature*, vol. 555, no. 7694, pp. 67–70, 2018. arXiv: 1810.05912.

[118] R. Barkana, 'Possible interaction between baryons and dark-matter particles revealed by the first stars', *Nature*, vol. 555, no. 7694, pp. 71–74, 2018. arXiv: 1803.06698.

[119] H. C. Van de Hulst, 'Radio waves from space: Origin of radiowaves', *Nederlands Tijdschrift voor Natuurkunde*, vol. 11, pp. 210–221, 1945, English translation: "Classics in Radio Astronomy", W.Sullivan, Reidel 1982.

[120] L. Greenhill, 'A surprising chill before the cosmic dawn', *Nature*, vol. 555, pp. 38–39, 2018. DOI: 10.1038/d41586-018-02310-9.

[121] G. B. Field, 'Excitation of the hydrogen 21-cm line', *Proceedings of the IRE*, vol. 46, pp. 240–250, 1958, ISSN: 0096-8390. DOI: 10.1109/JRPROC.1958.286741.

[122] S. A. Wouthuysen, 'On the excitation mechanism of the 21-cm (radio-frequency) interstellar hydrogen emission line.', *The Astronomical Journal*, vol. 57, pp. 31–32, 1952. DOI: 10.1086/106661.

[123] P. Madau, A. Meiksin and M. J. Rees, '21-cm tomography of the intergalactic medium at high redshift', *The astrophysical Journal*, vol. 475, p. 429, 1997. arXiv: astro-ph/9608010.

[124] S. Singh *et al.*, 'First results on the epoch of reionization from first light with SARAS 2', *The Astrophysical Journal*, vol. 845, p. L12, 2017. arXiv: 1703.06647.

[125] T. C. Voytek *et al.*, 'Probing the dark ages at $z \sim 20$: The SCI-HI 21 cm all-sky spectrum experiment', *The Astrophysical Journal*, vol. 782, p. L9, 2014. arXiv: 1311.0014.

[126] G. Bernardi *et al.*, 'Bayesian constraints on the global 21-cm signal from the Cosmic Dawn', *Monthly Notices of the Royal Astronomical Society*, vol. 461, pp. 2847–2855, 2016. arXiv: 1606.06006.

[127] B. J. Carr, 'Primordial black holes: Do they exist and are they useful?', in *59th Yamada Conference on Inflating Horizon of Particle Astrophysics and Cosmology Tokyo, Japan, June 20-24, 2005*, 2005. arXiv: astro-ph/0511743.

[128] S. W. Hawking, 'Gravitationally collapsed objects of very low mass', *Monthly Notices of the Royal Astronomical Society*, vol. 152, p. 75, 1971. DOI: 10.1093/mnras/152.1.75.

[129] S. W. Hawking, 'Black hole explosions', *Nature*, vol. 248, pp. 30–31, 1974. DOI: 10.1038/248030a0.

[130] M. Sasaki *et al.*, 'Primordial black holes—perspectives in gravitational wave astronomy', *Classical and Quantum Gravity*, vol. 35, 2018. arXiv: 1801.05235.

[131] B. P. Abbott *et al.*, 'Observation of gravitational waves from a binary black hole merger', *Physical Review Letters*, vol. 116, no. 6, 2016. arXiv: 1602.03837.

[132] B. P. Abbott *et al.*, 'GW170817: observation of gravitational waves from a binary neutron star inspiral', *Physical Review Letters*, vol. 119, no. 16, 2017. arXiv: 1710.05832.

[133] B. P. Abbott *et al.*, 'Multi-messenger observations of a binary neutron star merger', *The Astrophysical Journal*, vol. 848, no. 2, p. L12, 2017. arXiv: 1710.05833.

[134] P. Amaro-Seoane *et al.*, 'Laser Interferometer Space Antenna', *ArXiv e-prints*, 2017. arXiv: 1702.00786.

[135] C. J. Moore, R. H. Cole and C. P. L. Berry, 'Gravitational-wave sensitivity curves', *Classical and Quantum Gravity*, vol. 32, 2015. arXiv: 1408.0740.

[136] B. Carr, F. Kuhnel and M. Sandstad, 'Primordial black holes as dark matter', *Physical Review*, vol. D94, 2016. arXiv: 1607.06077.

[137] N. Bartolo *et al.*, 'The primordial black hole dark matter - LISA serendipity', 2018. arXiv: 1810.12218.

[138] R. Saito and J. Yokoyama, 'Gravitational-wave constraints on the abundance of primordial black holes', *Progress of Theoretical Physics*, vol. 123, no. 5, pp. 867–886, 2010. DOI: 10.1143/PTP.123.867.

[139] J. Garcia-Bellido, M. Peloso and C. Unal, 'Gravitational wave signatures of inflationary models from primordial black hole dark matter', *Journal of Cosmology and Astroparticle Physics*, vol. 1709, 2017. arXiv: 1707.02441.

[140] F. Capela, M. Pshirkov and P. Tinyakov, 'Constraints on primordial black holes as dark matter candidates from capture by neutron stars', *Physical Review*, vol. D87, 2013. arXiv: 1301.4984.

[141] A. Katz *et al.*, 'Femtolensing by dark matter revisited', *Journal of Cosmology and Astroparticle Physics*, vol. 1812, 2018. arXiv: 1807.11495.

[142] N. Seto, S. Kawamura and T. Nakamura, 'Possibility of direct measurement of the acceleration of the universe using 0.1-Hz band laser interferometer gravitational wave antenna in space', *Physical Review Letters*, vol. 87, 2001. arXiv: astro-ph/0108011.

[143] J. Crowder and N. J. Cornish, 'Beyond LISA: Exploring future gravitational wave missions', *Physical Review*, vol. D72, 2005. arXiv: gr-qc/0506015.

[144] M. Punturo *et al.*, 'The Einstein Telescope: A third-generation gravitational wave observatory', *Classical and Quantum Gravity*, vol. 27, 2010. DOI: 10.1088/0264-9381/27/19/194002.

[145] B. P. Abbott *et al.*, 'Exploring the sensitivity of next generation gravitational wave detectors', *Classical and Quantum Gravity*, vol. 34, 2017. arXiv: 1607.08697.

# Appendix A

## 1. Decay rate for $1 \to 2$ process

Consider a unstable particle a, which decays to other particles $a = 1 + 2 + \cdots + n$ from initial state $|i\rangle$ to final state $|f\rangle$. The decay rate for channel $f = 1 \ldots n$ is given by [66]

$$\Gamma_f = \frac{1}{2E_a} \int \Big( \prod_{i=1}^{n} \frac{d^3 p_i}{(2\pi)^3 2E_i} \Big) (2\pi)^4 \delta^{(4)}(p_a^\mu - \sum_{j=1}^{n} p_j^\mu) |\mathcal{M}_{fi}(a \to 1 \ldots n)|^2, \tag{A.1}$$

where $E$ is the energy of the particle, $\delta^{(4)}$ is the four dimensional Dirac delta function, $p^\mu$ is 4-momentum and $\mathcal{M}$ is the Lorentz invariant matrix element.

The decay rate for $a \to b + c$ decay is

$$\Gamma_a = \frac{(2\pi)^4}{2E_a} \int |\mathcal{M}|^2 \delta^{(4)}(p_c^\mu + p_b^\mu - p_a^\mu) \frac{d^3 p_c}{(2\pi)^3 2E_c} \frac{d^3 p_b}{(2\pi)^3 2E_b}. \tag{A.2}$$

The 4-momentum conservation can be written as energy conservation and 3-momentum conservation

$$\Gamma_a = \frac{(2\pi)^4}{2E_a} \int |\mathcal{M}|^2 \delta(E_c + E_b - E_a) \delta^{(3)}(p_c + p_b - p_a) \frac{d^3 p_c d^3 p_b}{(2\pi)^6 4E_c E_b}. \tag{A.3}$$

In CMS frame $E_a = m_a$ and $p_a = 0$, thus

$$\Gamma_a = \frac{1}{32\pi^2 m_a} \int |\mathcal{M}|^2 \delta(E_c + E_b - m_a) \delta^{(3)}(p_c + p_b) \frac{d^3 p_c d^3 p_b}{E_c E_b}. \tag{A.4}$$

Integrating over $d^3 p_b$ we get

$$\Gamma_a = \frac{1}{32\pi^2 m_a} \int |\mathcal{M}|^2 \delta(E_c + E_b - m_a) \frac{d^3 p_c}{E_c E_b}. \tag{A.5}$$

Writing $d^3 p_c = p_c^2 dp_c d\Omega$, integrating over $d\Omega$ and writing $p_c = -p_b$ we get

$$\Gamma_a = \frac{1}{8\pi m_a} \int |\mathcal{M}|^2 \delta\Big(\sqrt{m_c^2 + p_c^2} + \sqrt{m_b^2 + p_c^2} - m_a\Big) \frac{p_c^2 dp_c}{E_c E_b}. \tag{A.6}$$

Above equation can be written as

$$\Gamma_a = \frac{1}{8\pi m_a} \int |\mathcal{M}|^2 G(p_c) \delta(H(p_c)) dp_c, \tag{A.7}$$

where

$$G(p_c) = \frac{p_c^2}{E_c E_b} \tag{A.8}$$

and

$$H(p_c) = \sqrt{m_c^2 + p_c^2} + \sqrt{m_b^2 + p_c^2} - m_a. \tag{A.9}$$

In order to solve equation (A.7), we need to use properties of the $\delta$-function and find expression for $\delta(H(p_c))$. Let us start from the definition of $\delta$-function

$$\int_a^b \delta(y)dy = \begin{cases} 1 & \text{if } a < 0 < b \\ 0 & \text{otherwise,} \end{cases} \tag{A.10}$$

which can be expressed in terms of $y = H(p)$, where $H(p_0) = 0$

$$\int_{p_1}^{p_2} \delta(H(p))\frac{dH}{dp}dp = \begin{cases} 1 & \text{if } p_1 < p_0 < p_2 \\ 0 & \text{otherwise.} \end{cases} \tag{A.11}$$

Delta function is nonzero at $p_0$

$$\int_{p_1}^{p_2} \delta(H(p))H'(p_0)dp = \begin{cases} 1 & \text{if } p_1 < p_0 < p_2 \\ 0 & \text{otherwise.} \end{cases} \tag{A.12}$$

Rearranging and expressing the RHS as the delta function

$$\int_{p_1}^{p_2} \delta(H(p))dp = \frac{1}{H'(p_0)} \int_{p1}^{p2} \delta(p - p_0)dp. \tag{A.13}$$

Removing the integrals, we get expression what we were looking for

$$\delta(H(p)) = \frac{\delta(p - p_0)}{H'(p_0)}. \tag{A.14}$$

Using equation (A.14) $\Gamma_a$ can be written as

$$\Gamma_a = \frac{1}{8\pi m_a} \int |\mathcal{M}|^2 G(p_c) \frac{\delta(p_c - p_0)}{H'(p_c)} dp_c \tag{A.15}$$

where $H'$ is the first order derivative of $H$ with respect to $p_c$ and $p_0$ is the value for which $H(p_0) = 0$. Integrating over $p_c$ we get

$$\Gamma_a = \frac{|\mathcal{M}|^2}{8\pi m_a} \frac{G(p_0)}{H'(p_0)}. \tag{A.16}$$

$H'$ can be written as

$$\frac{dH}{dp_c} = \frac{p_c}{\sqrt{m_c^2 + p_c^2}} + \frac{p_c}{\sqrt{m_b^2 + p_c^2}} = \frac{p_c}{E_c} + \frac{p_c}{E_b} = \frac{p_c(E_c + E_b)}{E_c E_b}. \tag{A.17}$$

Substituting $H'$ and $G$ into equation (A.16) we get

$$\Gamma_a = \frac{|\mathcal{M}|^2}{8\pi m_a} \frac{p_0^2}{E_c E_b} \frac{E_c E_b}{p_0(E_c + E_b)}, \tag{A.18}$$

where $E_c + E_b = E_a = m_a$ thus, we find

$$\Gamma_a = \frac{|\mathcal{M}|^2 p_0}{8\pi m_a^2}. \tag{A.19}$$

An Expression for $p_0$ can be obtained from

$$H(p_0) = 0 \tag{A.20}$$

$$\sqrt{m_c^2 + p_0^2} + \sqrt{m_b^2 + p_0^2} = m_a. \tag{A.21}$$

After a few steps

$$2\sqrt{(m_c^2 + p_0^2)(m_b^2 + p_0^2)} = m_a^2 - m_b^2 - m_c^2 - 2p_0^2 \tag{A.22}$$

$$4(m_c^2 + p_0^2)(m_b^2 + p_0^2) = (m_a^2 - m_b^2 - m_c^2 - 2p_0^2)^2 \tag{A.23}$$

$$2m_b^2 m_c^2 = m_a^4 + m_b^4 + m_c^4 - 2m_a^2 m_c^2 - 2m_a^2 m_b^2 - 4m_a^2 p_0^2 \tag{A.24}$$

$$\begin{aligned} 4m_a^2 p_0^2 = (m_b^4 &- 2m_b^2 m_c^2 + m_c^4) \\ &- m_a^2(m_b^2 - 2m_b m_c + m_c^2) \\ &- m_a^2(m_b^2 + 2m_b m_c + m_c^2) + m_a^4 \end{aligned} \tag{A.25}$$

$$\begin{aligned} 4m_a^2 p_0^2 = (m_b - m_c)^2(m_b + m_c)^2 &- m_a^2(m_b - m_c)^2 \\ &- m_a^2(m_b + m_c)^2 + m_a^4 \end{aligned} \tag{A.26}$$

$$4m_a^2 p_0^2 = \left[m_a^2 - (m_b + m_c)^2\right]\left[m_a^2 - (m_b - m_c)^2\right] \tag{A.27}$$

we finally arrive at the result

$$p_0 = \frac{\sqrt{\left[m_a^2 - (m_b + m_c)^2\right]\left[m_a^2 - (m_b - m_c)^2\right]}}{2m_a}. \tag{A.28}$$

# Appendix B

## 1. Phase space Jacobian

Consider the following equations

$$f = \begin{cases} E_+ = E_1 + E_2 \\ E_- = E_1 - E_2 \\ s' = m_1^2 + m_2^2 + 2E_1E_2 - 2p_1p_2\cos\theta \end{cases} \tag{B.1}$$

where $E_i$ is energy, $m_i$ is mass and $p_i$ is 3-momentum of particle $i$. Consider a Lorentz invariant phase space element

$$\frac{d^3p_1}{(2\pi)^3 2E_1}\frac{d^3p_2}{(2\pi)^3 2E_2} \propto dE_1 dE_2 d\cos\theta. \tag{B.2}$$

In order to find $dE_1dE_2d\cos\theta$ in terms of $E_+, E_-$ and $s'$, we have to solve Jacobian determinant

$$\mathcal{J}_f(E_1, E_2, \cos\theta) = \begin{bmatrix} \frac{\partial E_+}{\partial E_1} & \frac{\partial E_+}{\partial E_2} & \frac{\partial E_+}{\partial \cos\theta} \\ \frac{\partial E_-}{\partial E_1} & \frac{\partial E_-}{\partial E_2} & \frac{\partial E_-}{\partial \cos\theta} \\ \frac{\partial s'}{\partial E_1} & \frac{\partial s'}{\partial E_2} & \frac{\partial s'}{\partial \cos\theta} \end{bmatrix} = \begin{bmatrix} 1 & 1 & 0 \\ 1 & -1 & 0 \\ 2E_2 & 2E_1 & -2p_1p_2 \end{bmatrix} = 4p_1p_2.$$

Therefore, the transformation between the two systems is

$$\int f(E_+, E_-, s')dE_+dE_-ds' = \int f(E_1, E_2, \cos\theta)4p_1p_2dE_1dE_2d\cos\theta. \tag{B.3}$$

## 2. Integration limits

Consider the following integration limits

$$\begin{cases} E_1 \geq m_1, \\ E_2 \geq m_2, \\ |\cos\theta| \leq 1. \end{cases} \tag{B.4}$$

Based on limits above, the Mandelstam variable $s'$ is in the region

$$s' \geq (m_1 + m_2)^2. \tag{B.5}$$

From the integration region of $s'$, we obtain limit for variable $E_+$

$$E_+ \geq \sqrt{s}. \tag{B.6}$$

The values for $E_-$ can be found from the definition of $s'$ in equation (B.1) after imposing the absolute limit $|\cos\theta| \leq 1$. Cosine of the angle $\theta$ for the upper limit can be written as

$$\cos\theta = \frac{s' - m_1^2 - m_2^2 - 2E_1E_2}{-2|p_1||p_2|} \leq 1. \tag{B.7}$$

Masses can be written in terms of momentum $|p_i|$ and energy $E_i$

$$\frac{s' - E_1^2 - 2E_1E_2 - E_2^2 + |p_1|^2 + |p_2|^2}{-2|p_1||p_2|} \leq 1. \tag{B.8}$$

Completing the square for energy we get

$$\frac{E_+^2 - s' - |p_1|^2 - |p_2|^2}{2|p_1||p_2|} \leq 1. \tag{B.9}$$

Modifying the equation further

$$E_+^2 - s' \leq |p_1|^2 + 2|p_1||p_2| + |p_2|^2, \tag{B.10}$$

$$E_+^2 - s' \leq \Big(|p_1| + |p_2|\Big)^2, \tag{B.11}$$

$$\Big(E_+^2 - s'\Big)^2 \leq \Big(|p_1| + |p_2|\Big)^2\Big(E_+^2 - s'\Big), \tag{B.12}$$

$$E_+^2 - s' \leq \Big(|p_1| + |p_2|\Big)\sqrt{E_+^2 - s'}, \tag{B.13}$$

we get

$$\frac{E_+^2}{\sqrt{s'}} \leq \Big(|p_1| + |p_2|\Big)\sqrt{\frac{E_+^2 - s'}{s'}} + \sqrt{s'}. \tag{B.14}$$

In CMS frame

$$\begin{cases} |p_1| = \lambda(s', m_1, m_2)/2\sqrt{s'}, \\ |p_2| = \lambda(s', m_1, m_2)/2\sqrt{s'}, \\ E_1 = (s' + m_1^2 - m_2^2)/2\sqrt{s'}, \\ E_2 = (s' - m_1^2 + m_2^2)/2\sqrt{s'}, \\ s' = (E_1 + E_2)^2, \end{cases} \tag{B.15}$$

where

$$\lambda(s', m_1, m_2,) = \Big[s' - (m_1 + m_2)^2\Big]\Big[s' - (m_1 - m_2)^2\Big]. \tag{B.16}$$

Using the results for CMS frame, we finally get the upper limit for $E_-$

$$E_- \leq 2\frac{\sqrt{\lambda(s', m_1, m_2)}}{2\sqrt{s'}}\sqrt{\frac{E_+^2 - s'}{s'}} + E_+\frac{m_1^2 - m_2^2}{s}. \tag{B.17}$$

Same calculation can be done for the lower limit thus, we get

$$\left|E_- - E_+\frac{m_{\psi_1}^2 - m_{\psi_2}^2}{s'}\right| \leq 2\frac{\sqrt{\lambda(s', m_1, m_2)}}{2\sqrt{s'}}\sqrt{\frac{E_+^2 - s'}{s'}}. \tag{B.18}$$

# Appendix C

## 1. Numerical methods: Integration

Solution to equation (4.7) in terms of special functions using Mathematica.

```
In[1]:= Simplify[Integrate[Sqrt[Energy^2 - m^2] * Exp[-Energy / T],
          {Energy, m, Infinity}, GenerateConditions → False], m > 0]
Out[1]= m T BesselK[1, m/T]
```

Solution to equation (4.13) in terms of special functions using Mathematica.

```
In[1]:= Integrate[BesselK[1, x] * x^3, {x, 0, Infinity}]
Out[1]= 3 π / 2
```

Solution to equation (4.46) in terms of special functions using Mathematica.

```
In[1]:= Simplify[Simplify[Integrate[(s - m^2) * BesselK[1, Sqrt[s] / T]
          / Sqrt[s], {s, m^2, Infinity}], m > 0], T > 0]
Out[1]= 4 m T^2 BesselK[1, m/T]
```

Solution to equation (4.50) in terms of special functions using Mathematica.

```
In[1]:= Integrate[BesselK[1, x] * x, {x, 0, Infinity}]
Out[1]= π / 2
```

## 2. Numerical methods: Density perturbations

Python code, which solves the evolution of density perturbations of dark matter, baryonic matter and radiation in synchronous gauge and creates Figure 11. Code utilizes Code for Anisotropies in the Microwave Background (CAMB) library [51].

```
# Author: Henri Jutila
# Date: 18.5.2019

from matplotlib import pyplot as plt
from matplotlib import rc
import sys, platform, os
import numpy as np
import matplotlib
import camb

n = 3000
eta = 10**(np.linspace(0, 4, n))
rc('font', **{'family': 'serif', 'serif': ['Computer Modern']})
rc('text', usetex=True)

# Set parameters and get various background functions
pars = camb.set_params(H0=67.4, ombh2=0.022, omch2=0.12, As=2e-9, ns=0.95)
data = camb.get_background(pars)

# Convert conformal time to scale factor
def unit_conversion(eta):

    second = 0.66E-15               # seconds [1/eV]
    meter = 0.2E-6                  # meter [1/eV]
    const = second/meter            # constant [s]/[m]
    mpc_m = 3.09E+22                # Megaparsec [m]
    mpc_s = const*mpc_m             # Megaparsec [s]
    eta_s = eta*mpc_s               # Conformal time [s]
    hubble_s = 67.4*1000/mpc_m      # Hubble constant [1/s]
    a_m = (eta_s*hubble_s/2)**2     # Scale factor mat. dom.
    a_r = (eta_s*hubble_s*3/4)      # Scale factor rad. dom.
    return a_r, a_m

def plot_ev(ev, k):

    plt.figure(figsize=(8,6))
    plt.grid()
    a_r, a_m = unit_conversion(eta)
    plt.loglog(a_m,ev[:,0])
    plt.loglog(a_m,np.abs(ev[:,1]))
    plt.loglog(a_m[:int(n*0.7)],np.abs(ev[:int(n*0.7),2]))
    plt.xlim([1E-7, 1E+0])
    plt.ylim([1E-3, 1E+4])
    plt.ylabel(r'Density perturbations $\delta$', fontsize=20)
```

```
45      plt.xlabel(r'Scale factor $a/a_0$', fontsize=20)
46      plt.legend([r'$\delta_c$',r'$|\delta_b|$', r'$|\delta_\gamma|$'], \
47                  loc='best', prop={'size':16})
48      plt.xticks(fontsize=18)
49      plt.yticks(fontsize=18)
50      plt.savefig('perturbation.eps', bbox_inches='tight')
51      plt.show()
52
53  def main():
54
55      k = 0.3
56      plot_ev(data.get_time_evolution(k, eta, ['delta_cdm', 'delta_baryon',\
57                                       'delta_photon'], lAccuracyBoost=10), k)
58  if __name__ == '__main__':
59      main()
```

# 3. Numerical methods: Freeze-out

Python code, which solves the evolution of comoving number density $Y$ (3.31) produced through thermal freeze-out mechanism and creates Figure 12.

```
# Author: Henri Jutila
# Date: 18.5.2019

from matplotlib.legend_handler import HandlerBase
from scipy.integrate import odeint
import matplotlib.pyplot as plt
from matplotlib import rc
import numpy as np

a = 1.0
m = 3.3
g = 2.0
p = 0.0
g_f = 1.17E-5
g_rho = 75.75
g_s = g_rho
m_p = 2.348*1E+18
cr_sec = a*(g_f*m)**2
cr_sec1 = cr_sec*5E-6
cr_sec2 = cr_sec*5E-5
cr_sec3 = cr_sec*5E-4

rc('font', **{'family': 'serif', 'serif': ['Computer Modern']})
rc('text', usetex=True)

class AnyObjectHandler(HandlerBase):
    def create_artists(self, legend, orig_handle,

                       x0, y0, width, height, fontsize, trans):
        if len(orig_handle) == 1:
            l = plt.Line2D([x0,y0+width], [0.5*height,0.5*height],
                           color=orig_handle[0])
            return [l]
        else:
            l1 = plt.Line2D([x0,y0+width], [0.7*height,0.7*height],
                           linestyle=orig_handle[1], color=orig_handle[0])
            l2 = plt.Line2D([x0,y0+width], [0.3*height,0.3*height],
                           color=orig_handle[0])
        return [l1, l2]

# Time of freeze-out (x = m/T)
def freeze_out_time(cr_sec):

    threshold = 1E-6
    y0 = 38 + np.log(g) - 0.5*np.log(g_rho/100) + np.log(m) + np.log(cr_sec)
```

```
46      y1 = y0 - 0.5*np.log(y0)
47      while True:
48
49          y_n = -0.5*np.log(y1) + y0
50          if abs(y_n - y1) < threshold:
51              break
52          else:
53              y1 = y_n
54      return y_n
55
56  # Analytical solution to comoving number density
57  def analytic(x, cr_sec, t_fo):
58
59      y_ini = np.ones(x)
60      y_0 = 38 + np.log(g) - 0.5*np.log(g_rho/100) + np.log(m) + np.log(cr_sec)
61      y_0 = y_0 - 0.5*np.log(y_0)
62      y = y_ini*0.75*((p+1)/(cr_sec))*((np.sqrt(g_rho))/(g_s))*(1/(m_p))*(t_fo/m)
63      return y
64
65  # Lee-Weinberg equation
66  def lee_weinberg(y,x, lambd):
67
68      yeq = equi_distri(x)
69      dydx = -lambd*x**(-2)*(y**2 - yeq**2)
70      return dydx
71
72  # Equilibrium comovin number density for non-relativistic species
73  def equi_distri(x):
74
75      yeq = 0.145*(g/g_s)*x**(3/2)*np.exp(-x)
76      return yeq
77
78  def main():
79
80      # Time of freeze-out and DM density
81      t_fo = freeze_out_time(cr_sec)
82      omega_h = 8.5E-11*(t_fo)*(p+1)*((np.sqrt(g_rho))/(g_s))*(1/cr_sec)
83      print('Freeze-out time: {0:0.3f}'.format(t_fo) )
84      print('Dark matter energy density: {0:0.3f}'.format(omega_h))
85
86      x = np.linspace(1, 1000, 10000)
87      y = equi_distri(x)
88
89      # freeze-out time with different cross sections
90      t_fo1 = freeze_out_time(cr_sec1)
91      t_fo2 = freeze_out_time(cr_sec2)
92      t_fo3 = freeze_out_time(cr_sec3)
93
94      # Analytical solution with different cross sections
```

```
95      y_analytic1 = analytic(len(x), cr_sec1, t_fo1)
96      y_analytic2 = analytic(len(x), cr_sec2, t_fo2)
97      y_analytic3 = analytic(len(x), cr_sec3, t_fo3)
98
99      # Constant prefactor in Lee-Weinberg
100     lambd1 = (g_s/np.sqrt(g_rho))*m_p*m*cr_sec1*(2*np.pi*np.sqrt(90))/45
101     lambd2 = (g_s/np.sqrt(g_rho))*m_p*m*cr_sec2*(2*np.pi*np.sqrt(90))/45
102     lambd3 = (g_s/np.sqrt(g_rho))*m_p*m*cr_sec3*(2*np.pi*np.sqrt(90))/45
103
104     # Solve Lee-Weinberg
105     y0 = 0.0
106     y1 = odeint(lee_weinberg, y0, x, args=(lambd1,))
107     y2 = odeint(lee_weinberg, y0, x, args=(lambd2,))
108     y3 = odeint(lee_weinberg, y0, x, args=(lambd3,))
109
110     plt.grid()
111     plt.ylim([1E-8, 1E-2])
112     plt.xlim([1E+0, 1E+3])
113     plt.loglog(x, y, color='black', linestyle='-', label=r'$Y_{eq}$')
114     plt.loglog(x[30:], y1[30:], color='orange', linestyle='--')
115     plt.loglog(x[55:], y2[55:], color='royalblue', linestyle='--')
116     plt.loglog(x[80:], y3[80:], color='limegreen', linestyle='--')
117     plt.plot(x, y_analytic1, color='orange', linestyle='-', label=r'$Y_1$')
118     plt.plot(x, y_analytic2, color='royalblue', linestyle='-', label=r'$$')
119     plt.plot(x, y_analytic3, color='limegreen', linestyle='-', label=r'$Y_3$')
120     plt.xlabel(r'$x = m/T$', fontsize=18)
121     plt.ylabel(r'Comoving number density $Y$', fontsize=18)
122     plt.xticks(fontsize=14)
123     plt.yticks(fontsize=14)
124     plt.legend([('k', ), ('orange', '--'),
125                 ('royalblue', '--'), ('limegreen', '--')],
126             [r'$Y_{\rm{eq}} = 0.145 \frac{g}{g_{*s}}$' \
127                 r'$\big(\frac{m}{T}\big)^{3/2}e^{-m/T}$',
128             r'$Y_0\big(\langle \sigma v \rangle = 7.5 \times 10^{-15}\big)$',
129             r'$Y_0\big(\langle \sigma v \rangle = 7.5 \times 10^{-14}\big)$',
130             r'$Y_0\big(\langle \sigma v \rangle = 7.5 \times 10^{-13}\big)$'],
131             handler_map={tuple: AnyObjectHandler()})
132
133     plt.savefig('analytical_wimp.eps', bbox_inches='tight')
134     plt.show()
135
136 if __name__ == '__main__':
137     main()
```

# 4. Numerical methods: Freeze-in

Python code, which solves the evolution of comoving number density $Y$ (4.13) produced via non-thermal freeze-in mechanism and creates Figure 13.

```
# Author: Henri Jutila
# Date: 18.5.2019

from matplotlib.legend_handler import HandlerBase
from scipy.integrate import odeint
import matplotlib.pyplot as plt
from scipy.special import kn
from matplotlib import rc
import numpy as np

g = 2
m1 = 1
m2 = 10
g_rho = 75.75
g_s = g_rho
g_f = 1.17E-5
lambd1 = 3E-10
lambd2 = 9E-11
lambd3 = 3E-11
m_p = 2.348*1E+18

rc('font', **{'family': 'serif', 'serif': ['Computer Modern']})
rc('text', usetex=True)

class AnyObjectHandler(HandlerBase):
    def create_artists(self, legend, orig_handle,

                       x0, y0, width, height, fontsize, trans):

        if orig_handle[2] == None:
            l = plt.Line2D([x0,y0+width], [0.5*height,0.5*height],
                           linestyle=orig_handle[1], color=orig_handle[0])
            return [l]
        else:
            l1 = plt.Line2D([x0,y0+width], [0.7*height,0.7*height],
                           linestyle=orig_handle[1], color=orig_handle[0])
            l2 = plt.Line2D([x0,y0+width], [0.3*height,0.3*height],
                           linestyle=orig_handle[2], color=orig_handle[0])
        return [l1, l2]

# Comoving number density
def density(y, x, lambd):

    gamma = (lambd**2*m2)/(8*np.pi)
    a = 405*np.sqrt(10)*g/(8*np.pi**4)
```

```
46      b = (m_p*gamma)/(m2**2*g_s*np.sqrt(g_rho))
47      dydx = [a*b*kn(1, x)*x**3]
48      return dydx
49
50  # Equilibrium comovin number density for non-relativistic species
51  def equi_distri(x):
52
53      yeq = 0.145*(g/g_s)*x**(3/2)*np.exp(-x)
54      return yeq
55
56  def main():
57
58      # Solve Y
59      y0 = 0
60      x = np.linspace(1, 1000, 100000)
61      y = equi_distri(x)
62      y1 = odeint(density, y0, x, args=(lambd1, ))
63      y2 = odeint(density, y0, x, args=(lambd2, ))
64      y3 = odeint(density, y0, x, args=(lambd3, ))
65
66      plt.loglog(x, y, color='k', linestyle='-')
67      plt.loglog(x, y1[:, 0], color='orange', linestyle='--')
68      plt.loglog(x, y2[:, 0], color='royalblue', linestyle='--')
69      plt.loglog(x, y3[:, 0], color='limegreen', linestyle='--')
70
71      plt.legend([('k', '-', None), ('orange', '--', None),
72                  ('royalblue', '--', None), ('limegreen', '--', None)],
73                  [r'$Y_{\rm{eq}} = 0.145 \frac{g}{g_{*s}}$' \
74                      r'$\big(\frac{m}{T}\big)^{3/2}e^{-m/T}$',
75                  r'$Y_0\big(\lambda = 3.0 \times 10^{-10}\big)$',
76                  r'$Y_0\big(\lambda = 9.0 \times 10^{-11}\big)$',
77                  r'$Y_0\big(\lambda = 3.0 \times 10^{-11}\big)$'],
78                  handler_map={tuple: AnyObjectHandler()})
79
80      plt.ylim([1E-8, 1E-2])
81      plt.xlim([1.1E+0, 1E+3])
82      plt.xlabel(r'$x = m_{\psi_1}/T$', fontsize=18)
83      plt.ylabel(r'Comoving number density $Y$', fontsize=18)
84      plt.xticks(fontsize=14)
85      plt.yticks(fontsize=14)
86      plt.grid()
87      plt.savefig('fimp_plot_new.eps', bbox_inches='tight')
88      plt.show()
89
90  if __name__ == '__main__':
91      main()
```